Effect of Mixing, Particle Interaction, and Spatial Dimension on the Glass Transition

Dissertation

zur Erlangung des Grades

„Doktor der Naturwissenschaften"

am Fachbereich Physik

der Johannes Gutenberg-Universität Mainz

vorgelegt von

David Hajnal

geboren in Budapest

Mainz im August 2010

1. Berichterstatter:

2. Berichterstatter:

Tag der mündlichen Prüfung: 25. Oktober 2010

D77

Parts of this thesis have already been published in:

- D. Hajnal, J. M. Brader, and R. Schilling,

  Effect of mixing and spatial dimension on the glass transition,

  Phys. Rev. E **80**, 021503 (2009).

- D. Hajnal, M. Oettel, and R. Schilling,

  Glass transition of binary mixtures of dipolar particles in two dimensions, J. Non-Cryst. Solids (2010), doi:10.1016/j.jnoncrysol.2010.06.039.

Zusammenfassung

In der vorliegenden Dissertation werden im Rahmen der Modenkopplungstheorie (MCT) die Auswirkungen von Änderungen in der Zusammensetzung binärer Flüssigkeiten in zwei und drei Raumdimensionen (2D/3D) auf deren Glasübergangsverhalten untersucht.

Die wohlbekannten Modenkopplungsgleichungen werden für die Beschreibung isotroper und homogener Mehrkomponentenflüssigkeiten in beliebigen Raumdimensionen verallgemeinert. Außerdem wird eine neue Methode eingeführt, die eine schnelle und präzise Berechnung spezieller Eigenschaften so genannter Glasübergangslinien erlaubt. Die neuen Gleichungen werden auf verschiedene Modellsysteme angewandt. Diese sind binäre Mischungen harter Scheiben/Kugeln in 2D/3D, binäre Mischungen dipolarer Punktteilchen in 2D, sowie binäre Mischungen dipolar wechselwirkender harter Scheiben in 2D. Einige generelle Eigenschaften der Glasübergangslininen werden ebenfalls dargestellt.

Es wird gezeigt, dass sich binäre harte Scheiben in 2D qualitativ ähnlich zu den binären harten Kugeln in 3D verhalten. Insbesondere werden für binäre harte Scheiben in 2D die selben vier so genannten Mischungseffekte identifiziert, die bereits zuvor von Götze und Voigtmann für binäre harte Kuglen veröffentlicht wurden [Phys. Rev. E **67**, 021502 (2003)]. Beispielsweise kann, je nach Radienverhältnis, das Hinzufügen einer zweiten Komponente zu einer Einkomponentenflüssigkeit entweder den Flüssigkeitszustand oder den Glaszustand stabilisieren. Die Resultate aus der MCT für binäre harte Scheiben in 2D stimmen qualitativ mit vorliegenden Resultaten aus Computersimulationen überein. Ferner ähneln die mittels MCT berechneten Glasübergangslinien für binäre harte Scheiben in 2D sehr stark den entsprechenden Computersimulationsresultaten für dichte Zufallspackungen.

Ein Vergleich von experimentell bestimmten Strukturfaktoren zu denen aus Computersimulationen zeigt, dass das experimentelle System von König at al. [Eur. Phys. J. E **18**, 287 (2005)] sich sehr gut durch binäre Mischungen dipolarer Punktteilchen in 2D beschreiben lässt. Für solche Punktteilchen wird gezeigt, dass im Gegensatz zu den Resultaten für binäre harte Scheiben in 2D oder harte Kugeln in 3D die MCT stets eine Stabilisierung des Flüssigkeitszustandes bei Mischung zweier Komponenten vorhersagt. Es wird ferner demonstriert, dass diese Vorhersage qualitativ mit experimentellen Resultaten im Einklang steht.

Schließlich wird ein Glasübergangsdiagramm für binäre Mischungen dipolar wechselwirkender harter Scheiben in 2D berechnet. Die Resultate zeigen, dass bei höheren Packungsbrüchen eine Konkurrenz der Mischungseffekte für binäre harte Scheiben in 2D und derer von binären Mischungen von Punktdipolen in 2D auftritt.

Abstract

In this thesis, the influence of composition changes on the glass transition behavior of binary liquids in two and three spatial dimensions (2D/3D) is studied in the framework of mode-coupling theory (MCT).

The well-established MCT equations are generalized to isotropic and homogeneous multi-component liquids in arbitrary spatial dimensions. Furthermore, a new method is introduced which allows a fast and precise determination of special properties of glass transition lines. The new equations are then applied to the following model systems: binary mixtures of hard disks/spheres in 2D/3D, binary mixtures of dipolar point particles in 2D, and binary mixtures of dipolar hard disks in 2D. Some general features of the glass transition lines are also discussed.

The direct comparison of the binary hard disk/sphere models in 2D/3D shows similar qualitative behavior. Particularly, for binary mixtures of hard disks in 2D the same four so-called mixing effects are identified as have been found before by Götze and Voigtmann for binary hard spheres in 3D [Phys. Rev. E **67**, 021502 (2003)]. For instance, depending on the size disparity, adding a second component to a one-component liquid may lead to a stabilization of either the liquid or the glassy state. The MCT results for the 2D system are on a qualitative level in agreement with available computer simulation data. Furthermore, the glass transition diagram found for binary hard disks in 2D strongly resembles the corresponding random close packing diagram.

Concerning dipolar systems, it is demonstrated that the experimental system of König et al. [Eur. Phys. J. E **18**, 287 (2005)] is well described by binary point dipoles in 2D through a comparison between the experimental partial structure factors and those from computer simulations. For such mixtures of point particles it is demonstrated that MCT predicts always a plasticization effect, i.e. a stabilization of the liquid state due to mixing, in contrast to binary hard disks in 2D or binary hard spheres in 3D. It is demonstrated that the predicted plasticization effect is in qualitative agreement with experimental results.

Finally, a glass transition diagram for binary mixtures of dipolar hard disks in 2D is calculated. These results demonstrate that at higher packing fractions there is a competition between the mixing effects occurring for binary hard disks in 2D and those for binary point dipoles in 2D.

Acknowledgments

Contents

Chapter 1

Introduction

The study of the dynamics of glass-forming liquids close to vitrification is a rapidly developing field in modern physics. The most important quantities for a description of such liquids in means of statistical mechanics are time-dependent auto-correlation functions of density fluctuations. Close to vitrification, these exhibit complex relaxation patterns, rather than following a simple exponential decay in time, as they would do in case of a normal liquid. In order to obtain an understanding of the basic mechanisms leading to the complex relaxation behavior mentioned above, one is interested in studying simple model systems which capture the essential qualitative features of glass formation. Hence, colloidal dispersions are often chosen for both experimental and theoretical investigations. Compared to atomic liquids, the advantages are obvious: the particle interactions can often be described theoretically by quite simple and well-defined expressions while experimental investigations can be performed by applying standard optical methods instead of neutron scattering techniques.

The first microscopic theory which was able to correctly predict many features of the complex dynamics of glass-forming liquids, the so-called mode-coupling theory (MCT), has been published 1984 by Bengtzelius, Götze, and Sjölander [1] and studied in the subsequent two decades in great detail by Götze and coworkers [2]. Although the equations are based on uncontrolled approximations, MCT serves up to now as the most successful theory for the description of the dynamics of colloidal glass-formers. The basic version of MCT considers isotropic and homogeneous one-component liquids in three spatial dimensions (3D). The only model-dependent input is given by the static structure factors of the considered liquid. The central prediction of MCT is a transition from a liquid into an ideal nonergodic glassy state upon decreasing temperature or increasing particle density below or above some critical value, respectively. Thermodynamic equilibrium quantities do not become singular at the glass transition singularity of MCT. Hence,

the liquid-to-glass transition predicted by MCT is a so-called dynamic transition.

The basic version of MCT has been successfully extended and applied to molecular liquids by Schilling and Scheidsteger [3], to multicomponent liquids in 3D by Barrat and Latz [4], and to colloidal dispersions under steady shear by Fuchs and Cates [5, 6]. The latter extension predicts a transition from a shear-thinning liquid with a finite zero-shear viscosity to a yielding glass with a finite zero-shear yield stress [7, 8]. This was confirmed by experiments of Crassous et al. [9] and, even more impressively, by experiments of Siebenbürger et al. [10]. Brader et al. [11, 12] have generalized the theory to colloidal dispersions under arbitrary time-dependent homogeneous flow. This theory, for instance, is capable to reproduce the existence of a so-called overshoot in the shear stress after a sudden switching on of a shear field, as was observed by Zausch et al. [13] in computer simulations. MCT was also extended and successfully applied to glass-forming liquids inside porous media by Krakoviack [14, 15, 16]. The qualitative properties of the glass transition diagram predicted by MCT have been confirmed by computer simulations of Kurzidim, Coslovich, and Kahl [17]. Furthermore, MCT was also extended to one-component liquids in arbitrary spatial dimensions by Bayer et al. [18], to driven granular fluids by Kranz, Sperl, and Zippelius [19], and recently also to glass-forming liquids in confined geometry by Lang et al. [20]. For hard sphere fluids confined between two parallel smooth plates, the latter extended version of the theory is capable to reproduce the dependence of the diffusivity on the plate distance obtained by Mittal et al. [21] via computer simulations. In this thesis we will present a further extended version of the MCT equations for multicomponent liquids in arbitrary spatial dimensions.

Now, after having illustrated the capabilities of MCT, let us come to the motivation of this thesis. Since it is well-known that physical phenomena like equilibrium phase transitions strongly depend on the spatial dimensionality d, there naturally appears the question about the d-dependence of the glass transition. Although there are from a fundamental point of view interesting studies concerning glass transitions in high dimensions, see for instance the recent publication of Schmid and Schilling [22] and the references therein, in this thesis we will restrict ourselves to the cases $d = 2$ and $d = 3$ which are experimentally accessible. Computer simulation results of Santen and Krauth [23] for polydisperse hard disks in 2D give evidence for the existence of a dynamic glass transition in 2D. Bayer et al. [18] have explored the question on the d-dependence of the glass transition by solving the mode-coupling equations for a one-component system of hard disks in two dimensions (2D). They have found an ideal glass transition at the critical 2D packing fraction $\varphi_0^c \cong 0.697$. On a qualitative level, the results of Bayer et

al. for the glass transition scenario for monodisperse hard disks in 2D are very similar to corresponding MCT results of Franosch et al. [24] for one-component systems of hard spheres in 3D.

In reality, one-component (monodisperse) systems do not serve as good glass-formers since they tend to form crystals rather than amorphous solids. Crystallization can be suppressed by using polydisperse systems. The simplest polydisperse system is a binary mixture. Since it is well-known that adding a second component to a one-component liquid may strongly influence both its static and dynamic properties, Götze and Voigtmann [25] have investigated systematically the glass transition behavior of binary hard spheres in 3D in the framework of MCT. They have found four qualitatively different effects on the relaxation behavior upon changing the composition of the mixtures. These effects we will generally call mixing effects in the following. For instance, depending on the size disparity, adding a second component to a one-component liquid may lead to a stabilization of either the liquid or the glassy state. The first central topic in this thesis will be to investigate within the framework of MCT whether the four mixing effects found by Götze and Voigtmann [25] for binary hard spheres in 3D also occur for binary hard disks in 2D. The results from this investigation will provide information about the question in how far the mechanisms for vitrification differ for $d = 2$ and $d = 3$. Furthermore, the comparison of MCT results for binary hard disks in 2D to available computer simulation data for the same model system will provide information about the quality of MCT in 2D.

As far as we know, the first experimental realization of a model glass-former in 2D was presented by König et al. [26]. They consider binary mixtures of super-paramagnetic colloidal particles on a water-air interface which interact via repulsive dipole-potentials. The magnetic moments are induced by an external magnetic field perpendicular to the water interface. Their results for the self-intermediate scattering functions measured by video microscopy clearly exhibit the stretched relaxation patterns of glass-forming liquids. Thus, the second central topic in this thesis will be a systematic investigation of the glass transition behavior of this well-defined 2D model system within the framework of MCT. The comparison of the obtained results for the dipolar system in 2D to those for binary hard disks in 2D will provide information about the question in how far the glass transition behavior is influenced by the type of particle interactions, which also justifies the title of this thesis. The comparison of experimental data of König et al. [26] to corresponding MCT results will provide further information about the quality of MCT in 2D.

This thesis is organized as follows. In Chapter 2 we summarize essential mathemat-

ical tools and notations. In addition, we derive a formula for the slope of a so-called critical line and describe how to apply it to a fold-bifurcation line. The glass transition lines being of central interest in this thesis will belong to this class. In Chapter 3 we introduce the correlation functions of main interest for a theoretical description of multicomponent liquids. In Chapter 4 we formulate the MCT equations for multicomponent liquids in arbitrary spatial dimensions and discuss their generic properties. In Chapters 5 and 6 we discuss in more detail some aspects of the experimental system of König et al. [26] and introduce the theoretical model systems which we will study in the framework of MCT in Chapters 7-9. We summarize and conclude in Chapter 10.

Chapter 2

Mathematical preliminaries

In this chapter, mathematical tools and notations are introduced which will be essential to understand the main parts of this thesis. Experienced readers may ask why the author dedicates a complete section to this purpose rather than banishing at least some parts of this chapter into the appendix. The answer is simple: in this thesis, the appendix is strictly reserved for more "boring" things like lengthy calculations or numerical algorithms which are not of importance for an understanding of the major results in this thesis. The author is of the opinion that following this rule makes the presentation more clearly arranged. Furthermore, beside summarizing basic tools like spherical coordinates in arbitrary dimensions, we also derive our first scientific result which will be of great importance in this thesis. It will be the so-called slope formula given by Eq. (2.26). In Sect. 2.6 we describe how to apply this formula to a so-called fold-bifurcation line. The glass transition lines being of central interest in this thesis will belong to this class. Thus, our slope formula will serve us as a new powerful tool for a fast and precise prediction of some properties of glass transition lines.

To avoid unnecessary paperwork, we declare some implicit assumptions: all functions occurring in the following formulas are assumed to be sufficiently well-behaved (like "sufficiently smooth", bounded, integrable etc...), such that all occurring expressions indeed exist.

2.1 Spatial Fourier transforms

Let $\vec{r}$ be a vector in a real position space with d dimensions and $f(\vec{r})$ a complex-valued function. Its spatial Fourier transform shall be defined by

$$f_{\vec{k}} = \int \mathrm{d}^d r \; f(\vec{r}) \exp(i\vec{k} \cdot \vec{r}) \tag{2.1}$$

where the integral extends over the whole space. $\vec{k}$ is a wave vector in reciprocal space with d dimensions. " $\cdot$ " denotes the standard scalar product of $\vec{k}$ and $\vec{r}$. The usefulness of our somewhat unconventional notation on the left-hand side (l.h.s.) of Eq. (2.1) will become clear in Sect. 2.5. There holds the inversion formula

$$f(\vec{r}) = (2\pi)^{-d} \int \mathrm{d}^d k \; f_{\vec{k}} \exp(-i\vec{k} \cdot \vec{r}). \tag{2.2}$$

The Fourier transform of an isotropic function $f(\vec{r}) = f(r)$ with $r = |\vec{r}|$ depends on the wave number only: $f_{\vec{k}} = f_k$ with $k = |\vec{k}|$. Here and in the following the reader should not be confused by the fact that we use the same symbol for different representations of a function. Furthermore, the extension of Eqs. (2.1) and (2.2) to matrix-valued functions is trivial.

2.2 Temporal Laplace transforms

Let $\phi(t)$ be a complex-valued function of time defined for $t \geq 0$. Following the conventions of Götze [2], we define its Laplace transform

$$\widehat{\phi}(z) = i \int_0^\infty \mathrm{d}t \; \phi(t) \exp(izt), \quad \Im\{z\} > 0. \tag{2.3}$$

Let $\dot{\phi}(t)$ denote the time derivative of $\phi(t)$. Its Laplace transform is given by

$$\widehat{\dot{\phi}}(z) = -i\phi(0) - iz\widehat{\phi}(z). \tag{2.4}$$

We define the time convolution of two functions by

$$(\psi * \phi)(t) = \int_0^t \mathrm{d}t' \; \psi(t - t')\phi(t'). \tag{2.5}$$

There holds the convolution theorem:

$$\widehat{(\psi * \phi)}(z) = -i\widehat{\psi}(z)\widehat{\phi}(z). \tag{2.6}$$

The long-time limit of a function is connected to a corresponding $1/z$-pole of its Laplace transform:

$$\lim_{t\to\infty} \phi(t) = -\lim_{z\to 0}\{z\widehat{\phi}(z)\}. \tag{2.7}$$

The extension of Eqs. (2.3)-(2.7) to matrix-valued functions is trivial.

2.3 Generalized spherical coordinates

Let $\vec{x} \neq \vec{0}$ be a vector in a space with $d \geq 3$ dimensions and $x = |\vec{x}|$. Its representation in Cartesian coordinates shall be given by $\vec{x} = \sum_{i=1}^{d} x_i \vec{e}_i$ with the orthonormal standard basis vectors $\vec{e}_i$. Now we choose $\vec{e}_d$ as polar axis and decompose $\vec{x}$ as follows: $\vec{x} = x\cos(\vartheta_{d-1})\vec{e}_d + x\sin(\vartheta_{d-1})\vec{x}'$ with $|\vec{x}'| = 1$ and $\vec{x}' \perp \vec{e}_d$. $\vartheta_{d-1} \in [0, \pi]$ is the angle between $\vec{x}$ and $\vec{e}_d$. Now, $\vec{x}'$ is a vector in a subspace with $(d-1) \geq 2$ dimensions perpendicular to $\vec{e}_d$. We have to consider two cases.

1. If $(d-1) = 2$, then we can represent $\vec{x}'$ in planar polar coordinates: $\vec{x}' = \cos(\vartheta_1)\vec{e}_2 + \sin(\vartheta_1)\vec{e}_1$ with $\vartheta_1 \in [0, 2\pi)$.

2. For $(d-1) \geq 3$ we choose $\vec{e}_{d-1}$ as new polar axis and decompose $\vec{x}'$ as follows: $\vec{x}' = \cos(\vartheta_{d-2})\vec{e}_{d-1} + \sin(\vartheta_{d-2})\vec{x}''$ with $|\vec{x}''| = 1$, $\vec{x}'' \perp \vec{e}_{d-1}$, $\vec{x}'' \perp \vec{e}_d$ and $\vartheta_{d-2} \in [0, \pi]$. Now, we consider $\vec{x}''$ and continue the decomposition procedure recursively until we end up with a vector in the subspace spanned by $\vec{e}_1$ and $\vec{e}_2$ where we can finally introduce polar coordinates like in case 1.

The procedure described above leads us to the following representation of the vector $\vec{x}$:

$$x_1 = x \prod_{i=1}^{d-1} \sin(\vartheta_i), \tag{2.8}$$

$$x_j = x\cos(\vartheta_{j-1}) \prod_{i=j}^{d-1} \sin(\vartheta_i), \quad 2 \leq j \leq d-1, \tag{2.9}$$

$$x_d = x\cos(\vartheta_{d-1}). \tag{2.10}$$

2.3.1 Jacobian determinant

Starting from Eqs. (2.8)-(2.10), we can proof by complete induction

$$\mathrm{d}^d x = \mathrm{d}\Omega_d x^{d-1} \mathrm{d}x, \tag{2.11}$$

$$\mathrm{d}\Omega_d = \mathrm{d}\Omega_{d-1} [\sin(\vartheta_{d-1})]^{d-2} \mathrm{d}\vartheta_{d-1}, \quad d \geq 3, \tag{2.12}$$

$$\mathrm{d}\Omega_2 = \mathrm{d}\vartheta_1. \tag{2.13}$$

We can conclude: Eqs. (2.8)-(2.10) define an invertible coordinate transformation if we require the following restrictions:

$$\begin{aligned} x &> 0, && (2.14)\\ \vartheta_1 &\in [0, 2\pi), && (2.15)\\ \vartheta_j &\in (0, \pi), \quad 2 \leq j \leq d-1. && (2.16) \end{aligned}$$

For the derivation of Eqs. (2.8)-(2.16) we have assumed $d \geq 3$, but it is obvious that the results also hold for $d = 2$, where we end up with planar polar coordinates.

2.3.2 An integral transformation formula

Later we will face integrals of the type $\int \mathrm{d}^d y \; F(|\vec{x}|, |\vec{y}|, |\vec{x} - \vec{y}|)$ with $d \geq 2$. The integral extends over the whole space. To write it in a more explicit way, we choose the fixed vector $\vec{x}$ as polar axis and ϑ_{d-1} as the angle between $\vec{x}$ and $\vec{y}$. For $\vec{z} = \vec{x} - \vec{y}$, $x = |\vec{x}|$, $y = |\vec{y}|$ and $z = |\vec{z}|$ we easily verify

$$|x - y| \leq z \leq x + y, \tag{2.17}$$

$$z^2 = x^2 + y^2 - 2xy\cos(\vartheta_{d-1}). \tag{2.18}$$

Now, let us replace the variable ϑ_{d-1} by the new variable z. Eq. (2.18) yields

$$\sin(\vartheta_{d-1}) = \frac{1}{2xy}\sqrt{4x^2y^2 - (x^2 + y^2 - z^2)^2}, \tag{2.19}$$

$$\mathrm{d}\vartheta_{d-1} = \frac{2z\mathrm{d}z}{\sqrt{4x^2y^2 - (x^2 + y^2 - z^2)^2}}. \tag{2.20}$$

Eqs. (2.19)-(2.20) hold for $\vartheta_{d-1} \in (0, \pi)$. To continue, we have to distinguish two cases.

1. If $d = 2$, then we have due to the symmetry of the considered integral above $\int \mathrm{d}\Omega_d \cdots = \int_0^{2\pi} \mathrm{d}\vartheta_1 \cdots = 2\int_0^{\pi} \mathrm{d}\vartheta_1 \cdots = 2\int_{|x-y|}^{x+y} \mathrm{d}z \; 2z[4x^2y^2 - (x^2+y^2-z^2)^2]^{-1/2} \ldots$
2. We have $\int \mathrm{d}\Omega_d \cdots = \int \mathrm{d}\Omega_{d-1} \int_{|x-y|}^{x+y} \mathrm{d}z \; 2z[4x^2y^2 - (x^2+y^2-z^2)^2]^{(d-3)/2}(2xy)^{2-d} \ldots$ for $d \geq 3$.

With these two results we can rewrite the entire integral for all $d \geq 2$ as

$$\int \mathrm{d}^d y \; F(|\vec{x}|, |\vec{y}|, |\vec{x} - \vec{y}|) = \frac{\Omega_{d-1}}{2^{d-3}x^{d-2}} \int_0^{\infty} \mathrm{d}y \int_{|x-y|}^{x+y} \mathrm{d}z \; \frac{yzF(x, y, z)}{[4x^2y^2 - (x^2 + y^2 - z^2)^2]^{\frac{3-d}{2}}} \tag{2.21}$$

where $\Omega_d = 2\pi^{d/2}/\Gamma(d/2)$ is the well-known result for the surface of a unit sphere in d dimensions. $\Gamma(\cdot)$ is the Gamma function. The special case $\Omega_1 = 2$ can be interpreted as follows: the "surface" of the interval $[-1, 1]$ consists of its two endpoints.

2.4 Critical hypersurfaces

Let us assume an arbitrary physical model system with L independent external control parameters $\vec{\xi} = (\xi_1, \ldots, \xi_L)$. Let us further assume that the control parameter space subdivides into two regions. These two regions shall be defined by the existence of two clearly distinguishable physical states. Here, the two states shall be denoted by "state 1" and "state 2". Generically, the transition from state 1 to state 2 takes place at some (locally) smooth critical hypersurface

$$\mathcal{H} = \{\vec{\xi} \mid \Sigma(\vec{\xi}) = 0\} \tag{2.22}$$

with $L - 1$ dimensions which separates the two regions. The function $\Sigma(\vec{\xi})$ is assumed to be real-valued. We call the elements of $\mathcal{H}$ critical points in the following.

2.4.1 Tangent hyperplanes and separation parameters

Let $\vec{\xi}^c = (\xi_1^c, \ldots, \xi_L^c) \in \mathcal{H}$ be a fixed critical point and $\Delta\vec{\xi} = \vec{\xi} - \vec{\xi}^c$. With Taylor's theorem we can write

$$\Sigma(\vec{\xi}^c + \Delta\vec{\xi}) = \sigma(\Delta\vec{\xi}) + \mathcal{O}(|\Delta\vec{\xi}|^2) \tag{2.23}$$

where $\sigma(\Delta\vec{\xi})$ is a linear real-valued function of $\Delta\vec{\xi}$. For such a function there always exists a scalar product representation. There holds

$$\sigma(\Delta\vec{\xi}) = \vec{\mathcal{N}} \cdot \Delta\vec{\xi} \tag{2.24}$$

with fixed $\vec{\mathcal{N}} = (\partial\sigma/\partial(\Delta\xi_1), \ldots, \partial\sigma/\partial(\Delta\xi_L))|_{\Delta\vec{\xi}=\vec{0}} = (\partial\Sigma/\partial\xi_1, \ldots, \partial\Sigma/\partial\xi_L)|_{\vec{\xi}=\vec{\xi}^c}$. Note that Eq. (2.24) is nothing but a trivial special case of the Riesz representation theorem. From Eqs. (2.22)-(2.24) we can read off:

$$\mathcal{T} = \{\vec{\xi} \mid \vec{\xi} = \vec{\xi}^c + \Delta\vec{\xi} \ \wedge \ \sigma(\Delta\vec{\xi}) = 0\} \tag{2.25}$$

is the tangent hyperplane of the hypersurface $\mathcal{H}$ at the critical point $\vec{\xi}^c$ and $\vec{\mathcal{N}}$ is perpendicular to $\mathcal{H}$ at $\vec{\xi}^c$. The symbol " $\wedge$ " represents the logical and-operator. We can conclude: generically, there exists some $\varepsilon > 0$ such that for all $\Delta\vec{\xi} \parallel \vec{\mathcal{N}}$ with $|\Delta\vec{\xi}| < \varepsilon$

the condition $\sigma(\Delta\vec{\xi}) < 0$ implies that the physical model system is in, say, state 1 while $\sigma(\Delta\vec{\xi}) > 0$ implies state 2. In this sense the function $\sigma(\Delta\vec{\xi})$ separates the two states, and thus we call it the separation parameter to $\vec{\xi}^c$.

2.4.2 Slope of a critical line

$\mathcal{H}$ can be locally represented as $\xi_l^{crit}(\xi_1, \ldots, \xi_{l-1}, \xi_{l+1}, \ldots, \xi_L)$ for any l. For fixed $\xi_i = \xi_i^c$, $i \neq j$, $i \neq l$, $\xi_l^{crit}(\xi_1^c, \ldots, \xi_{j-1}^c, \xi_j, \xi_{j+1}^c, \ldots, \xi_{l-1}^c, \xi_{l+1}^c, \ldots, \xi_L^c)$ describes a critical line which is a function of ξ_j. The separation parameter introduced above allows us to derive an expression for its slope $(\partial\xi_l^{crit}/\partial\xi_j)(\xi_1^c, \ldots, \xi_{j-1}^c, \xi_j, \xi_{j+1}^c, \ldots, \xi_{l-1}^c, \xi_{l+1}^c, \ldots, \xi_L^c)$. Differentiating $\Sigma(\xi_1^c, \ldots, \xi_{j-1}^c, \xi_j, \xi_{j+1}^c, \ldots, \xi_{l-1}^c, \xi_l^{crit}(\xi_1^c, \ldots, \xi_{j-1}^c, \xi_j, \xi_{j+1}^c, \ldots, \xi_{l-1}^c, \xi_{l+1}^c, \ldots, \xi_L^c), \xi_{l+1}^c, \ldots, \xi_L^c) = 0$ with respect to ξ_j and evaluating the result at $\xi_j = \xi_j^c$ yields with $\xi_l^{crit}(\xi_1^c, \ldots, \xi_j^c, \ldots, \xi_{l-1}^c, \xi_{l+1}^c, \ldots, \xi_L^c) = \xi_l^c$ and $\partial\Sigma/\partial\xi_i|_{\vec{\xi}=\vec{\xi}^c} = \partial\sigma/\partial(\Delta\xi_i)|_{\Delta\vec{\xi}=\vec{0}}$ the slope formula:

$$\frac{\partial\xi_l^{crit}}{\partial\xi_j}(\xi_1^c, \ldots, \xi_j^c, \ldots, \xi_{l-1}^c, \xi_{l+1}^c, \ldots, \xi_L^c) = -\left.\frac{\partial\sigma/\partial(\Delta\xi_j)}{\partial\sigma/\partial(\Delta\xi_l)}\right|_{\Delta\vec{\xi}=\vec{0}}. \tag{2.26}$$

Let us add some comments on Eq. (2.26). We have derived it in a quite general mathematical framework regardless to any specific application. In principle, Eq. (2.26) could be applied to any physical model system which has at least two control parameters and exhibits the transition scenario supposed above. In this thesis, we will demonstrate for two physical model systems that Eq. (2.26) can be applied as a new powerful tool for a fast and precise prediction of some properties of so-called glass transition lines.

2.5 A generalized matrix algebra

In this thesis, the objects of central interest will be matrix-valued isotropic correlation functions represented in Fourier space. For analytical calculations with such objects it turns out to be convenient to have an algebra with compact and elegant notation. Thus, let us declare: correlation functions are arrays of matrices denoted by bold symbols $\boldsymbol{A}$, $\boldsymbol{B}$ etc. Their "components" $\boldsymbol{A}_k$, $\boldsymbol{B}_k$ being $M \times M$ matrices $(A_k^{\alpha\beta})$, $(B_k^{\alpha\beta})$ (with some fixed natural number M) are labeled by subscript Latin indices (the wave numbers) which can be taken from a discrete or a continuous set. The elements $A_k^{\alpha\beta}$, $B_k^{\alpha\beta}$ of these matrices are indicated by superscript Greek indices, in some cases these elements shall also be denoted by $(\boldsymbol{A})_k^{\alpha\beta}$, $(\boldsymbol{B})_k^{\alpha\beta}$. Matrix products are defined component-wise, i.e. $\boldsymbol{C} = \boldsymbol{A}\boldsymbol{B}$ reads $\boldsymbol{C}_k = \boldsymbol{A}_k\boldsymbol{B}_k$ for all k. We call $\boldsymbol{A}$ positive-(semi-)definite, $(\boldsymbol{A} \succeq \boldsymbol{0})$, $\boldsymbol{A} \succ \boldsymbol{0}$, if this is true for all $\boldsymbol{A}_k$. $\boldsymbol{0}$ denotes the (generalized) zero matrix.

Later we will introduce model systems where k is restricted to a finite number of values. For such systems, the standard scalar product of $\boldsymbol{A}$ and $\boldsymbol{B}$ shall be defined as

$$(\boldsymbol{A}|\boldsymbol{B}) = \sum_k \sum_{\alpha,\beta} (A_k^{\alpha\beta})^* B_k^{\alpha\beta} \tag{2.27}$$

where the superscript * stands for complex conjugation. Having this scalar product, we can also introduce some further concepts from linear algebra. The standard norm of $\boldsymbol{A}$ shall be given by

$$|\boldsymbol{A}| = \sqrt{(\boldsymbol{A}|\boldsymbol{A})}. \tag{2.28}$$

Let $\boldsymbol{\mathcal{C}}[\boldsymbol{X}]$ be a linear map from the vector space spanned by the arrays of matrices specified above onto itself. Then $\boldsymbol{H}$ is called a (right-)eigenvector of $\boldsymbol{\mathcal{C}}$ to eigenvalue $r \in \mathbb{C}$ if $\boldsymbol{\mathcal{C}}[\boldsymbol{H}] = r\boldsymbol{H}$. The adjoint map $\boldsymbol{\mathcal{C}}^\dagger$ of $\boldsymbol{\mathcal{C}}$ satisfies

$$(\boldsymbol{\mathcal{C}}^\dagger[\boldsymbol{X}]|\boldsymbol{Y}) = (\boldsymbol{X}|\boldsymbol{\mathcal{C}}[\boldsymbol{Y}]) \tag{2.29}$$

for all $\boldsymbol{X}$, $\boldsymbol{Y}$. Its eigenvector $\hat{\boldsymbol{H}}$ to eigenvalue r^* is a so-called left-eigenvector of $\boldsymbol{\mathcal{C}}$ corresponding to the eigenvalue r.

2.6 Fold-bifurcations

From a mathematical point of view, the generic glass transitions singularities studied in this thesis are nothing but fold-bifurcations of the real solutions of nonlinear fixed-point equations. They are singularities of the class A_2 introduced by Arnol'd [27]. Thus, it seems reasonable to discuss the general mathematical signature of such bifurcations.

As framework we choose the vector space spanned by arrays of matrices as specified above where we assume that k is restricted to a finite number of values. We consider the fixed-point equation

$$\boldsymbol{F} = \boldsymbol{\mathcal{I}}[\boldsymbol{F}] \tag{2.30}$$

where the nonlinear map $\boldsymbol{\mathcal{I}}$ shall be real-valued if $\boldsymbol{F}$ has this property. Furthermore, $\boldsymbol{\mathcal{I}}$ shall smoothly depend on both $\boldsymbol{F}$ and the L independent external control parameters $\vec{\xi} = (\xi_1, \ldots, \xi_L)$. Eq. (2.30) may have several real solutions for $\boldsymbol{F}$. A bifurcation point, which we call critical point in the following, is a point $\vec{\xi}^c$ within the control parameter space at which at least two real solutions of Eq. (2.30) coincide. Such a bifurcation point is called an A_l-singularity, $l \geq 2$, if it is equivalent to the one described by a real root of degeneracy l of a real polynomial. An A_2-singularity is also called fold-bifurcation.

Let us investigate in more detail the case $l = 2$ and assume a critical point $\vec{\xi}^c$ where the real solution $\boldsymbol{F}^c$ of Eq. (2.30) is twofold degenerated. Quantities taken at the critical point $\vec{\xi}^c$ shall be indicated by a superscript c in the following. Now we are interested in the change in $\boldsymbol{F}$ upon small changes in $\vec{\xi}$. We assume $\vec{\xi} = \vec{\xi}^c + \Delta\vec{\xi}$ and thus also $\boldsymbol{F} = \boldsymbol{F}^c + \Delta\boldsymbol{F}$. Expanding $\boldsymbol{\mathcal{I}}$ with respect to $\Delta\boldsymbol{F}$ around $\boldsymbol{F}^c$ yields

$$\boldsymbol{\mathcal{I}}[\boldsymbol{F}] = \boldsymbol{\mathcal{I}}[\boldsymbol{F}^c] + \boldsymbol{\mathcal{C}}[\Delta\boldsymbol{F}] + \boldsymbol{\mathcal{D}}[\Delta\boldsymbol{F}, \Delta\boldsymbol{F}] + \mathcal{O}(|\Delta\boldsymbol{F}|^3) \tag{2.31}$$

where $\boldsymbol{\mathcal{C}}$ is linear and $\boldsymbol{\mathcal{D}}$ bilinear in $\Delta\boldsymbol{F}$. Let us also expand the coefficient functions with respect to $\Delta\vec{\xi}$ around $\vec{\xi}^c$,

$$\begin{aligned}
\boldsymbol{\mathcal{I}}[\boldsymbol{X}] &= \boldsymbol{\mathcal{I}}^c[\boldsymbol{X}] + \Delta\boldsymbol{\mathcal{I}}[\boldsymbol{X}] + \mathcal{O}(|\Delta\vec{\xi}|^2), && (2.32)\\
\boldsymbol{\mathcal{C}}[\boldsymbol{X}] &= \boldsymbol{\mathcal{C}}^c[\boldsymbol{X}] + \Delta\boldsymbol{\mathcal{C}}[\boldsymbol{X}] + \mathcal{O}(|\Delta\vec{\xi}|^2), && (2.33)\\
\boldsymbol{\mathcal{D}}[\boldsymbol{X}, \boldsymbol{Y}] &= \boldsymbol{\mathcal{D}}^c[\boldsymbol{X}, \boldsymbol{Y}] + \Delta\boldsymbol{\mathcal{D}}[\boldsymbol{X}, \boldsymbol{Y}] + \mathcal{O}(|\Delta\vec{\xi}|^2). && (2.34)
\end{aligned}$$

By substituting Eqs. (2.31)-(2.34) into Eq. (2.30) and using $\boldsymbol{F}^c = \boldsymbol{\mathcal{I}}^c[\boldsymbol{F}^c]$ we obtain

$$\begin{aligned}
\Delta\boldsymbol{F} - \boldsymbol{\mathcal{C}}^c[\Delta\boldsymbol{F}] &= \Delta\boldsymbol{\mathcal{I}}[\boldsymbol{F}^c] + \boldsymbol{\mathcal{D}}^c[\Delta\boldsymbol{F}, \Delta\boldsymbol{F}] \\
&\quad + \mathcal{O}(|\Delta\vec{\xi}|)\mathcal{O}(|\Delta\boldsymbol{F}|) + \mathcal{O}(|\Delta\boldsymbol{F}|^3) + \mathcal{O}(|\Delta\vec{\xi}|^2). \qquad (2.35)
\end{aligned}$$

A necessary condition for the twofold degeneracy of $\boldsymbol{F}^c$ is that the linear map given by the l.h.s. of Eq. (2.35) has a nontrivial kernel. Hence, $\boldsymbol{\mathcal{C}}^c$ must have $r = 1$ as eigenvalue. For the following, we assume that this eigenvalue is not degenerated. Under this condition right-eigenvector $\boldsymbol{H}^c$ and left-eigenvector $\hat{\boldsymbol{H}}^c$ to eigenvalue $r = 1$ can be chosen uniquely by requiring some appropriate normalizations and we can derive an asymptotic formula for $\Delta\boldsymbol{F}$. For this we use the decomposition

$$\Delta\boldsymbol{F} = g\boldsymbol{H}^c + \Delta\tilde{\boldsymbol{F}} \tag{2.36}$$

with $(\Delta\tilde{\boldsymbol{F}}|\boldsymbol{H}^c) = 0$ and thus also $(\hat{\boldsymbol{H}}^c|\Delta\tilde{\boldsymbol{F}}) = 0$. We substitute Eq. (2.36) into Eq. (2.35). Since $\Delta\tilde{\boldsymbol{F}}$ is perpendicular to the kernel of the linear map given by the l.h.s. of Eq. (2.35), the resulting equation can be formally resolved for $\Delta\tilde{\boldsymbol{F}}$ yielding

$$\Delta\tilde{\boldsymbol{F}} = \mathcal{O}(|\Delta\vec{\xi}|). \tag{2.37}$$

Now, we again substitute Eq. (2.36) into Eq. (2.35), take the scalar product of the

resulting equation with $\hat{\boldsymbol{H}}^c$ from the left, and use Eq. (2.37). We obtain

$$\begin{aligned} 0 &= (\hat{\boldsymbol{H}}^c|\Delta\boldsymbol{\mathcal{I}}[\boldsymbol{F}^c]) + g^2(\hat{\boldsymbol{H}}^c|\boldsymbol{\mathcal{D}}^c[\boldsymbol{H}^c,\boldsymbol{H}^c]) \\ &\quad +\mathcal{O}(|g|)\mathcal{O}(|\Delta\vec{\xi}|) + \mathcal{O}(|g|^3) + \mathcal{O}(|\Delta\vec{\xi}|^2). \end{aligned} \tag{2.38}$$

With this, our problem is reduced to the one of finding the real roots of a real polynomial in g. The assumption of the non-degeneracy of the eigenvalue $r = 1$ of $\boldsymbol{\mathcal{C}}^c$ was crucial for this. For the following, we assume $(\hat{\boldsymbol{H}}^c|\boldsymbol{\mathcal{D}}^c[\boldsymbol{H}^c,\boldsymbol{H}^c]) \neq 0$, otherwise we would have a higher-order bifurcation point of class A_l, $l \geq 3$. As last step we substitute the series ansatz $g = \sum_{n=1}^{\infty} g_n$ with $g_n = \mathcal{O}(|\Delta\vec{\xi}|^{\frac{n}{2}})$ into Eq. (2.38) yielding a sequence of equations for g_n which in principle, starting with $n = 1$, can be solved recursively for arbitrary n. For the solution $\boldsymbol{F}$ of Eq. (2.30) we obtain the leading $|\Delta\vec{\xi}|^{\frac{1}{2}}$-order asymptotes

$$\boldsymbol{F} = \boldsymbol{F}^c \pm \boldsymbol{H}^c\sqrt{-\frac{(\hat{\boldsymbol{H}}^c|\Delta\boldsymbol{\mathcal{I}}[\boldsymbol{F}^c])}{(\hat{\boldsymbol{H}}^c|\boldsymbol{\mathcal{D}}^c[\boldsymbol{H}^c,\boldsymbol{H}^c])}} + \mathcal{O}(|\Delta\vec{\xi}|). \tag{2.39}$$

Eq. (2.39) makes the signature of a fold-bifurcation clear: if $\vec{\xi}$ is first chosen such that $(\hat{\boldsymbol{H}}^c|\Delta\boldsymbol{\mathcal{I}}[\boldsymbol{F}^c])/(\hat{\boldsymbol{H}}^c|\boldsymbol{\mathcal{D}}^c[\boldsymbol{H}^c,\boldsymbol{H}^c]) > 0$ and then varied such that $(\hat{\boldsymbol{H}}^c|\Delta\boldsymbol{\mathcal{I}}[\boldsymbol{F}^c])$ changes its sign at $\vec{\xi} = \vec{\xi}^c$, then a pair of complex solutions of Eq. (2.30) merges into a pair of real ones at the critical point. Furthermore, the two solutions belonging to this pair coincide at $\vec{\xi} = \vec{\xi}^c$.

So far, we have discussed the local behavior of $\boldsymbol{F}$ in the neighborhood of a special fold-bifurcation point $\vec{\xi}^c$. Since we have assumed that the nonlinear map $\boldsymbol{\mathcal{I}}$ in Eq. (2.30) smoothly depends on L independent control parameters $\vec{\xi} = (\xi_1, \ldots, \xi_L)$, the set of bifurcation points will generically form some locally smooth critical hypersurface $\mathcal{H}$ with $L-1$ dimensions within the L-dimensional control parameter space. Now, let us assume that there is a locally smooth subset $\mathcal{U} \subset \mathcal{H}$ such that for all $\vec{\xi}^c \in \mathcal{U}$ the restrictions made above are fulfilled and thus also Eq. (2.39) holds. Let us fix some $\vec{\xi}^c \in \mathcal{U}$ and, without loss of generality, let us further assume $(\hat{\boldsymbol{H}}^c|\boldsymbol{\mathcal{D}}^c[\boldsymbol{H}^c,\boldsymbol{H}^c]) < 0$. If this is not the case, we simply redefine $\boldsymbol{\mathcal{D}} \mapsto -\boldsymbol{\mathcal{D}}$. The expression $(\hat{\boldsymbol{H}}^c|\Delta\boldsymbol{\mathcal{I}}[\boldsymbol{F}^c])$ being linear in $\Delta\vec{\xi}$ can be rewritten in its scalar product representation

$$(\hat{\boldsymbol{H}}^c|\Delta\boldsymbol{\mathcal{I}}[\boldsymbol{F}^c]) = \vec{\mathcal{N}} \cdot \Delta\vec{\xi} \tag{2.40}$$

similarly to Eq. (2.24). From Eqs. (2.39) and (2.40) we can now read off: generically, there exists some $\varepsilon > 0$ such that for all $\Delta\vec{\xi} \parallel \vec{\mathcal{N}}$ with $|\Delta\vec{\xi}| < \varepsilon$ the condition $(\hat{\boldsymbol{H}}^c|\Delta\boldsymbol{\mathcal{I}}[\boldsymbol{F}^c]) < 0$ implies that the solutions of Eq. (2.30) whose asymptotes are given

by Eq. (2.39) have non-vanishing imaginary parts while for $(\hat{\boldsymbol{H}}^c|\Delta\boldsymbol{\mathcal{I}}[\boldsymbol{F}^c]) > 0$ these solutions are real-valued. Hence, $\vec{\mathcal{N}}$ has to be perpendicular to $\mathcal{U}$ at $\vec{\xi}^c$ and the set

$$\mathcal{T} = \{\vec{\xi} \mid \vec{\xi} = \vec{\xi}^c + \Delta\vec{\xi} \ \wedge \ (\hat{\boldsymbol{H}}^c|\Delta\boldsymbol{\mathcal{I}}[\boldsymbol{F}^c]) = 0\} \tag{2.41}$$

is the tangent hyperplane of the hypersurface $\mathcal{U}$ at the critical point $\vec{\xi}^c$. Thus, up to a constant prefactor, we have derived an explicit expression

$$\sigma(\Delta\vec{\xi}) \propto (\hat{\boldsymbol{H}}^c|\Delta\boldsymbol{\mathcal{I}}[\boldsymbol{F}^c]) \tag{2.42}$$

for the separation parameter to $\vec{\xi}^c$ which was introduced in Sect. 2.4.1 in a more general framework.

Similarly to the discussion in Sect. 2.4.2, the locally smooth hypersurface $\mathcal{U}$ consisting of fold-bifurcation points can be locally represented as $\xi_l^{crit}(\xi_1, \ldots, \xi_{l-1}, \xi_{l+1}, \ldots, \xi_L)$ for any l. For fixed $\xi_i = \xi_i^c$, $i \neq j$, $i \neq l$, $\xi_l^{crit}(\xi_1^c, \ldots, \xi_{j-1}^c, \xi_j, \xi_{j+1}^c, \ldots, \xi_{l-1}^c, \xi_{l+1}^c, \ldots, \xi_L^c)$ describes a fold-bifurcation line which is a function of ξ_j. Eq. (2.42) opens up the possibility for calculating the slope of such a line by using the general slope formula given by Eq. (2.26).

2.7 Summary

In this chapter, we have first summarized some basic mathematical tools like spatial Fourier transforms, temporal Laplace transforms and generalized spherical coordinates. We have derived an integral transformation formula, Eq. (2.21), which will be of importance for our purposes. We have discussed the general mathematical concepts for the description of critical hypersurfaces. We have derived the slope formula, Eq. (2.26), for a critical line. Later we will demonstrate that this slope formula can be applied as a new powerful tool for a fast and precise prediction of some properties of glass transition lines. We have introduced a generalized matrix algebra which will allow us to formulate equations in the following chapters in a compact way. Finally, we have discussed the mathematical signature of fold-bifurcations. The glass transition singularities studied in this thesis will be bifurcations of this type.

Chapter 3

Physical preliminaries

In this chapter, we first specify the physical systems which will form the basis for this thesis. Second, we introduce the functions of main interest for a theoretical description of these systems. We also formulate some useful exact identities for the considered functions.

3.1 Multicomponent liquids

As starting point, we suppose a classical liquid consisting of M components. We choose to describe it in the canonical ensemble: the liquid shall be enclosed into some cubic box with volume V in d spatial dimensions and temperature T. The total number of particles shall be given by $N = \sum_{\alpha=1}^{M} N_\alpha$ where N_α denotes the number of particles of species α. To calculate thermodynamic limits of canonically averaged phase space functions, one has to consider $V \to \infty$ and $N \to \infty$ with fixed total particle density $n = N/V$ and fixed particle number concentrations $x_\alpha = N_\alpha/N$ for $1 \leq \alpha \leq M$. The existence of such limits is assumed throughout in this thesis. For the following, we also allow that the considered system of N particles is embedded as a subsystem into a larger particle system. Such an assumption is reasonable, for example, for the description of multicomponent mixtures of colloidal particles which are dispersed into some liquid solvent. The dynamics of the dispersed particles is then governed by the Liouville operator $\mathcal{L}$ which generates the dynamics of the complete particle system. Following Götze [2], we make the following restrictions: all particles shall interact only via centrosymmetric pair-potentials and, when considering thermodynamic limits, the complete system is assumed to be homogeneous, isotropic and free of chirality.

3.2 Collective density correlators

Let $n^\alpha(\vec{r},t) = \sum_{i=1}^{N_\alpha} \delta(\vec{r} - \vec{r}_{\alpha,i}(t))$ denote the time-dependent microscopic particle density of the component α of the liquid. $\vec{r}_{\alpha,i}(t)$ denotes the position of particle i of the component α at time t and $\delta(\cdot)$ is the Dirac delta distribution. The time-dependent density fluctuation of the component α of the liquid to wave vector $\vec{k}$ is given by the spatial Fourier transform (see Sect. 2.1) of $n^\alpha(\vec{r},t)$:

$$n_{\vec{k}}^\alpha(t) = \sum_{i=1}^{N_\alpha} \exp(i\vec{k}\cdot\vec{r}_{\alpha,i}(t)). \tag{3.1}$$

Form here, we will make use of the notations introduced in Sect. 2.5. We define for $t \geq 0$ the matrix of time-dependent partial auto-correlation functions of density fluctuations $\boldsymbol{\Phi}(t)$ with components $\Phi_k^{\alpha\beta}(t)$ by

$$\Phi_k^{\alpha\beta}(t) = \left\langle N^{-1}[n_{\vec{k}}^\alpha(t)]^* n_{\vec{k}}^\beta(0)\right\rangle_{TL}, \quad k > 0, \tag{3.2}$$

$$\Phi_0^{\alpha\beta}(t) = \lim_{k\to 0^+} \Phi_k^{\alpha\beta}(t), \tag{3.3}$$

where $\langle \ldots \rangle_{TL}$ means canonical averaging followed by performing the thermodynamic limit. We have the normalization $\boldsymbol{\Phi}(0) = \boldsymbol{S}$, where $\boldsymbol{S} \succ \boldsymbol{0}$ denotes the positive-definite static structure factor matrix whose elements obey $\lim_{k\to\infty} S_k^{\alpha\beta} = x_\alpha \delta_{\alpha\beta}$. Here $\delta_{\alpha\beta}$ denotes the Kronecker delta. Further, it can be shown that $\boldsymbol{\Phi}(t)$ is symmetric, there holds $\Phi_k^{\alpha\beta}(t) = \Phi_k^{\beta\alpha}(t)$ for all $t \geq 0$ [2].

3.3 Self-correlators

The collective density correlator $\Phi_k^{\alpha\beta}(t)$ can be decomposed as

$$\Phi_k^{\alpha\beta}(t) = x_\alpha \delta_{\alpha\beta} \Phi_{\alpha,k}^{self}(t) + x_\alpha x_\beta \Psi_k^{\alpha\beta}(t) \tag{3.4}$$

with the self-correlator of an arbitrary tagged particle i of species α

$$\Phi_{\alpha,k}^{self}(t) = \left\langle \exp(-i\vec{k}\cdot[\vec{r}_{\alpha,i}(t) - \vec{r}_{\alpha,i}(0)])\right\rangle_{TL}, \quad k > 0, \tag{3.5}$$

$$\Phi_{\alpha,0}^{self}(t) = \lim_{k\to 0^+} \Phi_{\alpha,k}^{self}(t), \tag{3.6}$$

and the remaining distinct part

$$\Psi_k^{\alpha\beta}(t) = \left\langle N \exp(-i\vec{k}\cdot[\vec{r}_{\alpha,i}(t) - \vec{r}_{\beta,j}(0)]) \right\rangle_{TL}, \quad k > 0, \quad (i \neq j) \vee (\alpha \neq \beta), \tag{3.7}$$

$$\Psi_0^{\alpha\beta}(t) = \lim_{k\to 0^+} \Psi_k^{\alpha\beta}(t). \tag{3.8}$$

The symbol " $\vee$ " represents the logical or-operator. From Eq. (3.4) we can read off the useful limiting formula

$$\Phi_{\alpha,k}^{self}(t) = \lim_{x_\alpha \to 0} \{\Phi_k^{\alpha\alpha}(t)/x_\alpha\}. \tag{3.9}$$

3.4 Mean-square displacements

The mean-square displacement (MSD) of an arbitrary tagged particle i of species α is given by

$$\delta r_\alpha^2(t) = \left\langle |\vec{r}_{\alpha,i}(t) - \vec{r}_{\alpha,i}(0)|^2 \right\rangle_{TL}. \tag{3.10}$$

A simple Taylor expansion of the exponential function in Eq. (3.5) yields a connection between the MSDs and the low wave number behavior of the self-correlators:

$$\delta r_\alpha^2(t) = 2d \lim_{k\to 0} \{[1 - \Phi_{\alpha,k}^{self}(t)]/k^2\}. \tag{3.11}$$

3.5 Summary

In this brief chapter we have specified d-dimensional multicomponent liquids as a physical starting point for our study. Further, we have introduced the functions of main interest for a statistical description of these liquids: the collective density correlators, and the self-correlators and MSDs of tagged particles. However, we have not yet introduced any method for an explicit determination of these functions. The next chapter will be dedicated to this issue.

Chapter 4

Mode-coupling theory

In the last chapter, we have formally defined several correlation functions for a statistical description of multicomponent liquids in d spatial dimensions. To proceed, we need some (approximative) technique for an explicit calculation of these objects. Since we are interested in the glass transition behavior of the physical systems specified above, we choose MCT [2] as theoretical framework.

So far, MCT equations were derived for multicomponent liquids in 3D [2] and also for one-component liquids in arbitrary dimensions [18]. In this chapter, we extend these equations to multicomponent liquids in arbitrary dimensions d. Rather than rewriting the complete derivation of the MCT equations for multicomponent liquids given in [2], we restrict ourselves to highlight the few necessary modifications when dropping the restriction $d = 3$. We also restrict ourselves to present the overdamped versions of the MCT equations since the model systems studied in this thesis theoretically are all motivated by experiments on colloidal dispersions (see the next chapter). Furthermore, we neglect throughout the static triple-correlation functions, for technical simplicity. The latter simplification is known as the so-called convolution approximation.

4.1 Equations for the collective density correlators

Up to some few modifications, the derivation of the MCT equations can be copied from Ref. [2]. First we notice that the formal structure of the exact Zwanzig-Mori equation for $\mathbf{\Phi}(t)$ does not explicitly depend on the spatial dimension d. For overdamped colloidal dynamics it reads

$$\boldsymbol{\tau}\dot{\mathbf{\Phi}}(t) + \boldsymbol{S}^{-1}\mathbf{\Phi}(t) + \int_0^t \mathrm{d}t' \; \boldsymbol{m}(t-t')\dot{\mathbf{\Phi}}(t') = \mathbf{0}. \tag{4.1}$$

$\boldsymbol{\tau}$ is a positive-definite matrix of microscopic relaxation times. Its components shall be approximated by

$$\tau_k^{\alpha\beta} = \delta_{\alpha\beta}/(k^2 D_\alpha^0 x_\alpha) \tag{4.2}$$

where D_α^0 denotes the short-time diffusion coefficient of a single particle of the species α inserted into the fluid. Hydrodynamic interactions are neglected. In Sect. 4.3 we will provide a phenomenological justification for Eq. (4.2). The short-time asymptote of $\boldsymbol{\Phi}(t)$ is given by

$$\boldsymbol{\Phi}(t \to 0^+) = \boldsymbol{S} - \boldsymbol{\tau}^{-1} t + \mathcal{O}(t^2). \tag{4.3}$$

The memory kernel $\boldsymbol{m}(t)$ describing fluctuating stresses can not be calculated explicitly. In the framework of MCT, it is approximated by a symmetric bilinear functional $\boldsymbol{\mathcal{F}}$ of $\boldsymbol{\Phi}(t)$,

$$\boldsymbol{m}(t) = \boldsymbol{\mathcal{F}}[\boldsymbol{\Phi}(t), \boldsymbol{\Phi}(t)]. \tag{4.4}$$

The derivation of an explicit expression for the components of $\boldsymbol{\mathcal{F}}$ follows exactly the steps in Ref. [2] with two modifications. First, we perform the thermodynamic limit by applying the rule $V^{-1}\sum_{\vec{k}} \ldots \mapsto (2\pi)^{-d}\int \mathrm{d}^d k \ldots$ and obtain for the components $\mathcal{F}_k^{\alpha\beta}[\boldsymbol{X}, \boldsymbol{Y}]$ integrals of the type $\int \mathrm{d}^d p \; F(|\vec{k}|, |\vec{p}|, |\vec{k}-\vec{p}|)$. Second, assuming $d \geq 2$, we apply then Eq. (2.21). After dropping the static triple-correlation functions, the final result reads

$$\mathcal{F}_k^{\alpha\beta}[\boldsymbol{X}, \boldsymbol{Y}] = \frac{\Omega_{d-1}}{(4\pi)^d} \sum_{\alpha',\beta',\alpha'',\beta''} \int_0^\infty \mathrm{d}p \int_{|k-p|}^{k+p} \mathrm{d}q \; V_{k;p,q}^{\alpha\beta;\alpha'\beta',\alpha''\beta''} X_p^{\alpha'\beta'} Y_q^{\alpha''\beta''} \tag{4.5}$$

with the vertices

$$V_{k;p,q}^{\alpha\beta;\alpha'\beta',\alpha''\beta''} = \frac{n}{x_\alpha x_\beta} \frac{pq}{k^{d+2}} v_{kpq}^{\alpha\alpha'\alpha''} v_{kpq}^{\beta\beta'\beta''} \tag{4.6}$$

where

$$v_{kpq}^{\alpha\beta\gamma} = \frac{(k^2+p^2-q^2)c_p^{\alpha\beta}\delta_{\alpha\gamma} + (k^2-p^2+q^2)c_q^{\alpha\gamma}\delta_{\alpha\beta}}{[4k^2p^2 - (k^2+p^2-q^2)^2]^{(3-d)/4}}. \tag{4.7}$$

$c_k^{\alpha\beta}$ denote the direct correlation functions. $\boldsymbol{c}$ is related to $\boldsymbol{S}$ via the Ornstein-Zernike equation

$$(\boldsymbol{S}^{-1})_k^{\alpha\beta} = \delta_{\alpha\beta}/x_\alpha - n c_k^{\alpha\beta}. \tag{4.8}$$

Eqs. (4.1)-(4.8) serve now as a closed set of self-consistent nonlinear equations for the calculation of $\boldsymbol{\Phi}(t)$. They provide the theoretical framework for this thesis. The interaction potentials for a specific model system enter the MCT equations only via the static structure factors. For their determination some independent approach is needed since MCT does not provide any method to calculate the static correlation matrix $\boldsymbol{S}$.

4.2 Equations for the self-correlators

The MCT equations for the self-correlators $\Phi^{self}_{\alpha,k}(t)$ can be derived from the MCT equations for the collective density correlators $\Phi^{\alpha\beta}_k(t)$ by applying the following "trick": we add an additional component $M+1$ consisting of particles of species α, $1 \leq \alpha \leq M$, to the M-component system and apply then Eq. (3.9) for the component $M+1$. The calculation is in principle straightforward but somewhat tedious. The final result is

$$\tau^{self}_{\alpha,k}\dot{\Phi}^{self}_{\alpha,k}(t) + \Phi^{self}_{\alpha,k}(t) + \int_0^t \mathrm{d}t'\; m^{self}_{\alpha,k}(t-t')\dot{\Phi}^{self}_{\alpha,k}(t') = 0, \tag{4.9}$$

$$\tau^{self}_{\alpha,k} = 1/(k^2 D^0_\alpha), \tag{4.10}$$

$$\Phi^{self}_{\alpha,k}(t \to 0^+) = 1 - t/\tau^{self}_{\alpha,k} + \mathcal{O}(t^2), \tag{4.11}$$

$$\begin{aligned} m^{self}_{\alpha,k}(t) \;&=\; \mathcal{F}^{self}_{\alpha,k}[\mathbf{\Phi}(t), \underline{\Phi}^{self}_{\alpha}(t)] = \frac{\Omega_{d-1}}{(4\pi)^d}\sum_{\alpha',\alpha''}\int_0^\infty \mathrm{d}p \int_{|k-p|}^{k+p}\mathrm{d}q \\ &\times 2n\frac{pq}{k^{d+2}}\frac{(k^2+p^2-q^2)^2 c^{\alpha\alpha'}_p c^{\alpha\alpha''}_p}{[4k^2p^2-(k^2+p^2-q^2)^2]^{(3-d)/2}}\Phi^{\alpha'\alpha''}_p(t)\Phi^{self}_{\alpha,q}(t), \end{aligned} \tag{4.12}$$

where $\underline{\Phi}^{self}_{\alpha}(t)$ has to be read as an array whose components $\Phi^{self}_{\alpha,k}(t)$ are labeled by the subscript k. Eqs. (4.9)-(4.12) are a set of self-consistent equations for $\underline{\Phi}^{self}_{\alpha}(t)$ which need the full solution for the collective correlation matrix $\mathbf{\Phi}(t)$ as input.

4.3 Equations for the mean-square displacements

The MCT equations for the MSD of an arbitrary tagged particle i of species α follow from Eqs. (4.9)-(4.12) by performing the $k \to 0$ limit according to Eq. (3.11). For this purpose it turns out to be convenient to use Eq. (2.21) to transform Eq. (4.12) back to Cartesian coordinates. Then it is easy to verify

$$\delta r^2_\alpha(t) + D^0_\alpha \int_0^t \mathrm{d}t'\; m^{msd}_\alpha(t-t')\delta r^2_\alpha(t') = 2dD^0_\alpha t, \tag{4.13}$$

$$\delta r^2_\alpha(t \to 0^+) = 2dD^0_\alpha t, \tag{4.14}$$

$$m_\alpha^{msd}(t) = \mathcal{F}_\alpha^{msd}[\mathbf{\Phi}(t), \underline{\Phi}_\alpha^{self}(t)] = \frac{n(\Omega_d/d)}{(2\pi)^d} \sum_{\alpha',\alpha''} \int_0^\infty \mathrm{d}p\; p^{d+1} c_p^{\alpha\alpha'} c_p^{\alpha\alpha''} \Phi_p^{\alpha'\alpha''}(t) \Phi_{\alpha,p}^{self}(t). \tag{4.15}$$

Eqs. (4.13)-(4.15) require the full solutions for $\mathbf{\Phi}(t)$ and $\underline{\Phi}_\alpha^{self}(t)$ as input. Eq. (4.14) can be regarded as an a-posteriori justification for our choice for the matrix $\boldsymbol{\tau}$ of microscopic relaxation times: Eq. (4.2) is the simplest ansatz which yields the phenomenologically expected short-time diffusion behavior according to Eq. (4.14).

4.4 Discretized models

The motivation for introducing discretized versions of the MCT equations is twofold. First, the MCT equations above can only be solved numerically which naturally requires discretized equations. Second, several theorems on the MCT equations can be proved provided that the wave number k is restricted to some finite set excluding $k = 0$ [28].

For the following, we discretize k to a finite, equally spaced grid of K points

$$k = (\hat{o}_d + \hat{k})\Delta k \tag{4.16}$$

with $\hat{k} = 0, 1, \ldots, K-1$ and $0 < \hat{o}_d < 1$. The integrals in Eqs. (4.5), (4.12), and (4.15) are then replaced by Riemann sums

$$\int_0^\infty \mathrm{d}p \ldots \int_{|k-p|}^{k+p} \mathrm{d}q \ldots \mapsto \sum_{\hat{p}=0}^{K-1} \Delta k \ldots \sum_{\hat{q}=|\hat{k}-\hat{p}|}^{\min\{K-1,\hat{k}+\hat{p}\}} \Delta k \ldots, \tag{4.17}$$

and Eqs. (4.1), (4.9), and (4.13) represent a finite number of coupled nonlinear equations. The parameters o_d, Δk, and K have to be chosen appropriately for a given model system.

4.5 Ideal glass transition singularities

The nonergodicity parameters (NEPs) $\boldsymbol{F} = (F_k^{\alpha\beta})$ for the collective motion are given by $\boldsymbol{F} = \lim_{t\to\infty} \mathbf{\Phi}(t)$. $\boldsymbol{F} = \mathbf{0}$ corresponds to a liquid state, while $\boldsymbol{F} \succ \mathbf{0}$ defines a glassy state. With Eqs. (4.1)-(4.4) and Eqs. (2.3)-(2.7) we can easily show that $\boldsymbol{F}$ is a fixed point of the nonlinear map

$$\boldsymbol{\mathcal{I}}[\boldsymbol{X}] = \boldsymbol{S} - (\boldsymbol{S}^{-1} + \boldsymbol{\mathcal{F}}[\boldsymbol{X}, \boldsymbol{X}])^{-1}. \tag{4.18}$$

Obviously, $\boldsymbol{X} = \boldsymbol{0}$ is always a fixed point. In general, $\boldsymbol{\mathcal{I}}$ may have more than one fixed point. Thus the question: how can $\boldsymbol{F}$ be characterized?

For the discretized models described above, several statements can be proved rigorously [28]: Eq. (4.1) has a unique solution. It is defined for all $t \geq 0$ and is completely monotone, i.e. $(-\partial/\partial t)^l \boldsymbol{\Phi}(t) \succeq \boldsymbol{0}$ for all l. $\boldsymbol{F} \succeq \boldsymbol{0}$ is with respect to the semi-order " $\succeq$ " the maximum real, symmetric fixed point of $\boldsymbol{\mathcal{I}}$. Iterating Eq. (4.18) starting with $\boldsymbol{X} = \boldsymbol{S}$ leads to a monotonically decaying sequence converging towards $\boldsymbol{F}$, this fact can be utilized for a numerical determination of the NEPs. Linearization of $\boldsymbol{\mathcal{I}}$ around $\boldsymbol{F}$ similarly to Eq. (2.31) yields a so-called positive linear map

$$\boldsymbol{\mathcal{C}}[\boldsymbol{Y}] = 2(\boldsymbol{S} - \boldsymbol{F})\boldsymbol{\mathcal{F}}[\boldsymbol{F}, \boldsymbol{Y}](\boldsymbol{S} - \boldsymbol{F}) \tag{4.19}$$

in the sense that $\boldsymbol{\mathcal{C}}[\boldsymbol{Y}] \succeq \boldsymbol{0}$ for all $\boldsymbol{Y} \succeq \boldsymbol{0}$. The physical picture of the MCT equations that correlations for all wave numbers are coupled leads to the further assumption that $\boldsymbol{\mathcal{C}}$ is an irreducible map if $\boldsymbol{F} \succ \boldsymbol{0}$ [28]. According to a generalized version of the Perron-Frobenius theorem, the maximum eigenvalue $0 < r \leq 1$ of $\boldsymbol{\mathcal{C}}$ is then non-degenerated and thus the corresponding right-eigenvector $\boldsymbol{H} \succ \boldsymbol{0}$ and the corresponding left-eigenvector $\hat{\boldsymbol{H}} \succ \boldsymbol{0}$ (see Sect. 2.5 for its definition) are then determined uniquely by requiring the normalizations [29]

$$(\hat{\boldsymbol{H}}|\boldsymbol{H}) = (\hat{\boldsymbol{H}}|\boldsymbol{H}\{\boldsymbol{S} - \boldsymbol{F}\}^{-1}\boldsymbol{H}) = 1. \tag{4.20}$$

For any eigenvalue $\tilde{r} \neq r$ of $\boldsymbol{\mathcal{C}}$, $|\tilde{r}| \leq |r|$ holds, and if $|\tilde{r}| = |r|$, then the corresponding eigenvector can not be positive-definite. Hence, remembering the bifurcation analysis in Sect. 2.6, we can state that possible MCT singularities are identified by $r = 1$ and belong to the class A_l, $l = 2, 3, \ldots$, according to the terminology of Arnol'd [27].

The generic liquid-glass transition singularities studied in detail in this thesis belong to the class A_2. For a model system with L physical control parameters $\vec{\xi} = (\xi_1, \ldots, \xi_L)$ they form a locally smooth critical hypersurface $\mathcal{H}$ with $L - 1$ dimensions within the L-dimensional physical control parameter space. Quantities taken at such critical points shall be indicated by a superscript c in the following. While in the liquid regime $\boldsymbol{X} = \boldsymbol{0}$ is the maximum real, symmetric fixed point of $\boldsymbol{\mathcal{I}}$ and thus it is $\boldsymbol{F} = \boldsymbol{0}$, at $\vec{\xi}^c \in \mathcal{H}$ a further real, symmetric fixed point $\boldsymbol{X} = \boldsymbol{F}^c$ appears which, due to the bilinear dependence of $\boldsymbol{\mathcal{F}}$ on $\boldsymbol{F}$ in the fixed-point equation $\boldsymbol{F} = \boldsymbol{\mathcal{I}}[\boldsymbol{F}]$, has the generic feature $\boldsymbol{F}^c \succ \boldsymbol{0}$. The maximum property of $\boldsymbol{F}$ implies then that $\boldsymbol{F}$ jumps at $\vec{\xi} = \vec{\xi}^c$ from $\boldsymbol{0}$ to $\boldsymbol{F} = \boldsymbol{F}^c \succ \boldsymbol{0}$. Hence, the liquid-glass transition predicted by MCT is a so-called type-B transition.

For $\vec{\xi}^c \in \mathcal{H}$, the proven properties of the MCT equations cited above guarantee that Eqs. (2.39)-(2.42) can be directly applied with $\boldsymbol{\mathcal{I}}$ given by Eq. (4.18). With this, it is

easy to verify that for $\vec{\xi} = \vec{\xi}^c + \Delta\vec{\xi}$ with some fixed $\vec{\xi}^c \in \mathcal{H}$ the separation parameter $\sigma(\Delta\vec{\xi})$ to $\vec{\xi}^c$, which is specified up to a constant prefactor by Eq. (2.42), can be chosen by expanding

$$\tilde{\sigma}(\vec{\xi}) = (\hat{\boldsymbol{H}}^c|\{\boldsymbol{S}^c - \boldsymbol{F}^c\}\boldsymbol{S}^{c-1}\{\boldsymbol{S}\boldsymbol{\mathcal{F}}[\boldsymbol{F}^c, \boldsymbol{F}^c](\boldsymbol{S} - \boldsymbol{F}^c) - \boldsymbol{S}^c\boldsymbol{\mathcal{F}}^c[\boldsymbol{F}^c, \boldsymbol{F}^c](\boldsymbol{S}^c - \boldsymbol{F}^c)\}) \quad (4.21)$$

around $\vec{\xi}^c$ up to linear order in $\Delta\vec{\xi}$. Let us further introduce the so-called exponent parameter [2, 29]

$$\lambda^c = (\hat{\boldsymbol{H}}^c|\{\boldsymbol{S}^c - \boldsymbol{F}^c\}\boldsymbol{\mathcal{F}}^c[\boldsymbol{F}^c, \boldsymbol{F}^c]\{\boldsymbol{S}^c - \boldsymbol{F}^c\}), \quad (4.22)$$

the terminology will become clear in Sect. 4.6. Taking the above cited maximum property for the NEPs into account, we can specialize Eq. (2.39) to determine the asymptotic behavior of the NEPs for $\sigma(\Delta\vec{\xi}) > 0$, i.e. inside the glassy regime. The leading-order asymptotic result reads

$$\boldsymbol{F} = \boldsymbol{F}^c + \boldsymbol{H}^c\sqrt{\sigma(\Delta\vec{\xi})/(1-\lambda^c)} + \mathcal{O}(|\Delta\vec{\xi}|). \quad (4.23)$$

This square-root law is also called factorization theorem since to leading order the quantity $\boldsymbol{F} - \boldsymbol{F}^c$ factorizes into a wave number and particle index dependent part $\boldsymbol{H}^c$ evaluated at $\vec{\xi}^c$ and a function depending only on the separation parameter $\sigma(\Delta\vec{\xi})$ to $\vec{\xi}^c$. At generic liquid-glass transition points $\vec{\xi}^c$ belonging to the class A_2 it is $1/2 < \lambda^c < 1$. Higher-order singularities of class A_l with $l \geq 3$ are characterized by $\lambda^c = 1$ [2].

We can locally represent the critical hypersurface $\mathcal{H}$ as $\xi_l^{crit}(\xi_1, \ldots, \xi_{l-1}, \xi_{l+1}, \ldots, \xi_L)$ for any l. For fixed $\xi_i = \xi_i^c$, $i \neq j$, $i \neq l$, $\xi_l^{crit}(\xi_1^c, \ldots, \xi_{j-1}^c, \xi_j, \xi_{j+1}^c, \ldots, \xi_{l-1}^c, \xi_{l+1}^c, \ldots, \xi_L^c)$ defines a so-called glass transition line which is a function of ξ_j. For an explicit calculation of the slope of such a line we can specialize Eq. (2.26) to

$$\frac{\partial\xi_l^{crit}}{\partial\xi_j}(\xi_1^c, \ldots, \xi_j^c, \ldots, \xi_{l-1}^c, \xi_{l+1}^c, \ldots, \xi_L^c) = -\left.\frac{\partial\tilde{\sigma}/\partial\xi_j}{\partial\tilde{\sigma}/\partial\xi_l}\right|_{\vec{\xi}=\vec{\xi}^c} \quad (4.24)$$

where only those quantities on the r.h.s. of Eq. (4.21) without the superscript c are differentiated.

4.6 Asymptotic relaxation laws

Close to the liquid-glass transition, MCT makes universal predictions for the relaxation behavior of $\boldsymbol{\Phi}(t)$ which can be studied in the framework of asymptotic expansions. Here we restrict ourselves to cite the major results from this asymptotic approach.

For the following, let $\vec{\xi}^c \in \mathcal{H}$ be a fixed generic A_2 liquid-glass transition point and $\Delta\vec{\xi} = \vec{\xi} - \vec{\xi}^c$. Furthermore, we assume that the mode-coupling functional $\boldsymbol{\mathcal{F}}[\boldsymbol{X}, \boldsymbol{Y}]$ depends smoothly on $\Delta\vec{\xi}$ for all $\boldsymbol{X}$, $\boldsymbol{Y}$. Two quantities will be of great importance in this section. The first one is the separation parameter $\sigma(\Delta\vec{\xi})$ which is obtained from Eq. (4.21) by expanding $\tilde{\sigma}(\vec{\xi})$ around $\vec{\xi}^c$ up to linear order in $\Delta\vec{\xi}$. For the following discussion, $\Delta\vec{\xi} \neq \vec{0}$ shall be chosen such that $\sigma(\Delta\vec{\xi}) \neq 0$, i.e. $\vec{\xi}$ is assumed not to be an element of the tangent hyperplane $\mathcal{T}$ of the critical hypersurface $\mathcal{H}$ at $\vec{\xi}^c$. The second important quantity will be the exponent parameter λ^c given by Eq. (4.22) whose value determines the exponents occurring in the asymptotic scaling laws discussed below. These positive exponents will be the critical exponent a obeying the relation

$$\Gamma^2(1-a)/\Gamma(1-2a) = \lambda^c, \tag{4.25}$$

the von Schweidler exponent b satisfying

$$\Gamma^2(1+b)/\Gamma(1+2b) = \lambda^c, \tag{4.26}$$

and the exponent

$$\gamma = (a+b)/(2ab) \tag{4.27}$$

describing the divergence of the time scale for the final relaxation of $\boldsymbol{\Phi}(t)$ to $\mathbf{0}$ upon increasing $\sigma(\Delta\vec{\xi}) < 0$ towards 0 [2].

4.6.1 The first scaling-law regime

Beside the theorems cited in Sect. 4.5 it can be proved [2] that $\boldsymbol{\Phi}(t)$ depends smoothly on $\Delta\vec{\xi}$ for every fixed finite time interval. Together with the fact $\lim_{t\to\infty} \boldsymbol{\Phi}^c(t) = \boldsymbol{F}^c$ for $\Delta\vec{\xi} = \vec{0}$ this implies the following: for every given arbitrary small error $\varepsilon > 0$ and every arbitrary large time increment $\Delta t > 0$ there exists some open neighborhood $\mathcal{B}$ of $\vec{\xi}^c$ and some time interval $[t_1, t_2]$ of length Δt such that for all $\vec{\xi} \in \mathcal{B}$ and $t_1 < t < t_2$ there holds $|\boldsymbol{\Phi}(t) - \boldsymbol{F}^c| < \varepsilon$. This means that for $\vec{\xi}$ close to $\vec{\xi}^c$ the correlation matrix $\boldsymbol{\Phi}(t)$ develops a dynamics located around $\boldsymbol{F}^c$ for a large time interval which is also called the β-relaxation process.

For times within the so-called first scaling-law regime defined by $|\boldsymbol{\Phi}(t) - \boldsymbol{F}^c| \ll 1$ there holds the factorization theorem [2, 24]

$$\boldsymbol{\Phi}(t) - \boldsymbol{F}^c = \boldsymbol{H}^c \mathcal{G}(t) + \mathcal{O}(|\Delta\vec{\xi}|) \tag{4.28}$$

with the β-correlator $\mathcal{G}(t) = \mathcal{O}(|\sigma|^{1/2}) = \mathcal{O}(|\Delta\vec{\xi}|^{1/2})$ obeying the equation of motion

$$\sigma + \lambda^c \mathcal{G}^2(t) = \frac{\mathrm{d}}{\mathrm{d}t} \int_0^t \mathrm{d}t' \mathcal{G}(t-t')\mathcal{G}(t') \tag{4.29}$$

with the so-called critical law

$$\mathcal{G}(t \to 0) = (t/t_0)^{-a} \tag{4.30}$$

as short-time asymptote. The $\Delta\vec{\xi}$-independent time scale t_0 has to be matched to the full solution of Eq. (4.1) at $\vec{\xi} = \vec{\xi}^c$ since in this case the power law occurring in Eq. (4.30) is a special solution of Eq. (4.29) which describes the relaxation of $\boldsymbol{\Phi}^c(t)$ towards $\boldsymbol{F}^c$. It is easy to verify that $\mathcal{G}(t)$ obeys the scaling law

$$\mathcal{G}(t, \sigma \gtrless 0) = |\sigma|^{1/2} \tilde{\mathcal{G}}(\tilde{t} = t/t_\sigma, \tilde{\sigma} = \pm 1), \tag{4.31}$$

$$t_\sigma = t_0 |\sigma|^{-\frac{1}{2a}}. \tag{4.32}$$

The master function $\tilde{\mathcal{G}}(\tilde{t})$ obeys Eq. (4.29) with the replacements $\sigma \mapsto \sigma/|\sigma| = \pm 1$, $t \mapsto \tilde{t}$, and the short-time asymptote $\tilde{\mathcal{G}}(\tilde{t} \to 0) = (\tilde{t})^{-a}$. For $\sigma > 0$, t_σ is a characteristic time scale for the relaxation of $\boldsymbol{\Phi}(t)$ towards $\boldsymbol{F}$. In the liquid regime, i.e. $\sigma < 0$, t_σ defines the characteristic time scale on which $\boldsymbol{\Phi}(t)$ crosses the critical plateau $\boldsymbol{F}^c$. Obviously, the so-called β-time scale t_σ shows a power-law divergence upon $\sigma \to 0$.

Eq. (4.29) can be solved by asymptotic series expansions [8]. One finds the leading long-time asymptotes

$$\mathcal{G}(t \to \infty, \sigma > 0) = \sqrt{\sigma/(1-\lambda^c)}, \tag{4.33}$$

$$\mathcal{G}(t \to \infty, \sigma < 0) = -(t/\tau)^b. \tag{4.34}$$

Eq. (4.33) describes the asymptotic behavior of $\boldsymbol{F}$ in the glassy regime close to $\vec{\xi}^c$. This result reproduces the square-root law for the NEPs given by Eq. (4.23). Eq. (4.34) is referred to as the von Schweidler law and describes the initial part of the relaxation of $\boldsymbol{\Phi}(t)$ from $\boldsymbol{F}^c$ to $\mathbf{0}$. Eqs. (4.31) and (4.32) imply

$$\tau = \tilde{\tau} t_0 |\sigma|^{-\gamma} \tag{4.35}$$

with the $\Delta\vec{\xi}$-independent constant $\tilde{\tau}$ which demonstrates that the arrest of $\boldsymbol{\Phi}(t)$ to $\boldsymbol{F}^c$ at $\vec{\xi} = \vec{\xi}^c$ is caused by a power-law divergence of the times scale τ for the onset of the relaxation of $\boldsymbol{\Phi}(t)$ from $\boldsymbol{F}^c$ to $\mathbf{0}$ upon $\sigma \to 0^-$. Furthermore, because of $\gamma = (a+b)/(2ab) > 1/(2a)$, this time scale diverges faster than the β-time scale t_σ, and this

fact manifests itself in the characteristic two-step relaxation process of $\mathbf{\Phi}(t)$ in the liquid regime close to vitrification.

4.6.2 The second scaling-law regime

Now we turn to the relaxation process of $\mathbf{\Phi}(t)$ from $\boldsymbol{F}^c$ to $\mathbf{0}$ within the liquid regime which is also called the α-relaxation process. As already stated above, the time scale τ for this process diverges faster upon approaching the glass transition point than the time scale for the β-relaxation. Thus, the α-relaxation can be separated from the β-dynamics by considering the limits $\sigma \to 0^-$ and $t \to \infty$ with fixed $\widetilde{t} = t/\tau$. One arrives at the so-called α-scaling law [2, 24]

$$\mathbf{\Phi}(t) = \widetilde{\mathbf{\Phi}}^c(\widetilde{t} = t/\tau) + \mathcal{O}(|\Delta\vec{\xi}|) \tag{4.36}$$

where the $\Delta\vec{\xi}$-independent master function $\widetilde{\mathbf{\Phi}}^c(\widetilde{t})$ obeys the equation of motion

$$(\boldsymbol{S}^c)^{-1}\widetilde{\mathbf{\Phi}}^c(\widetilde{t}) = \widetilde{\boldsymbol{m}}^c(\widetilde{t})\boldsymbol{S}^c - \frac{\mathrm{d}}{\mathrm{d}\widetilde{t}}\int_0^{\widetilde{t}} \mathrm{d}\widetilde{t}'\widetilde{\boldsymbol{m}}^c(\widetilde{t}-\widetilde{t}')\widetilde{\mathbf{\Phi}}^c(\widetilde{t}') \tag{4.37}$$

with the memory kernel

$$\widetilde{\boldsymbol{m}}^c(\widetilde{t}) = \boldsymbol{\mathcal{F}}^c[\widetilde{\mathbf{\Phi}}^c(\widetilde{t}), \widetilde{\mathbf{\Phi}}^c(\widetilde{t})] \tag{4.38}$$

and the von Schweidler law

$$\widetilde{\mathbf{\Phi}}^c(\widetilde{t} \to 0) = \boldsymbol{F}^c - \boldsymbol{H}^c(\widetilde{t})^b \tag{4.39}$$

as short-time asymptote. Eq. (4.36) is also called superposition principle due to the following implication: for times within the so-called second scaling-law regime given by $t \gg \tau$, density correlators $\Phi_k^{\alpha\beta}(t)$ corresponding to different small values of $\sigma(\Delta\vec{\xi}) < 0$ collapse onto master curves $(\widetilde{\mathbf{\Phi}}^c)_k^{\alpha\beta}(\widetilde{t})$ when they are plotted as functions of $\widetilde{t} = t/\tau$.

4.7 Coupled quantities

We can introduce further important quantities coupled to $\boldsymbol{F}$. The tagged-particle NEPs $F_{\alpha,k}^{self} \geq 0$ are given by the array $\underline{F}_\alpha^{self} = \lim_{t\to\infty} \underline{\Phi}_\alpha^{self}(t)$. It is the maximum real fixed point of the nonlinear map [2]

$$\mathcal{I}_{\alpha,k}^{self}[\underline{X}] = 1 - (1 + \mathcal{F}_{\alpha,k}^{self}[\boldsymbol{F}, \underline{X}])^{-1} \tag{4.40}$$

which can be derived analogously to the one in Eq. (4.18). The so-called localization length is defined by

$$\Delta r_\alpha = \lim_{t\to\infty} \sqrt{\delta r_\alpha^2(t)/(2d)}. \tag{4.41}$$

By using Eqs. (4.13)-(4.15) and Eqs. (2.3)-(2.7) we can easily show that the localization length can be directly calculated from $\boldsymbol{F}$ and $\underline{F}_\alpha^{self}$ via

$$\Delta r_\alpha = \sqrt{1/\mathcal{F}_\alpha^{msd}[\boldsymbol{F}, \underline{F}_\alpha^{self}]}. \tag{4.42}$$

Obviously, $\boldsymbol{F} = \boldsymbol{0}$ implies $\underline{F}_\alpha^{self} = \underline{0}$ where $\underline{0}$ is an array whose elements are all zero, and thus also $\Delta r_\alpha = \infty$.

Now, let us consider an arbitrary physical model system which is driven through its glass transition by varying one physical control parameter $\xi \geq 0$ while all remaining control parameters shall be kept fixed. Let us further assume that the vertices monotonically increase upon increasing ξ in the sense that $\xi_2 > \xi_1$ implies $\boldsymbol{\mathcal{F}}[\boldsymbol{X}, \boldsymbol{X}; \xi_2] \succ \boldsymbol{\mathcal{F}}[\boldsymbol{X}, \boldsymbol{X}; \xi_1]$ and $\mathcal{F}_{\alpha,k}^{self}[\boldsymbol{X}, \underline{X}; \xi_2] > \mathcal{F}_{\alpha,k}^{self}[\boldsymbol{X}, \underline{X}; \xi_1]$ for all $\boldsymbol{X} \succ \boldsymbol{0}$ and $\underline{X} > \underline{0}$ (the last inequality has to be read component-wise). The model system shall exhibit an ideal glass transition singularity at some $0 < \xi^c < \infty$ such that $\boldsymbol{F} = \boldsymbol{0}$ if $0 \leq \xi < \xi^c$, and $\boldsymbol{F} \succ \boldsymbol{0}$ for all $\xi > \xi^c$. At $\xi = \xi^c$, $\boldsymbol{F}$ shall jump from $\boldsymbol{0}$ to $\boldsymbol{F}^c \succ \boldsymbol{0}$. As already mentioned above, this jump is generic due to the bilinear dependence of $\boldsymbol{\mathcal{F}}$ on $\boldsymbol{F}$ in the fixed-point equation $\boldsymbol{F} = \boldsymbol{\mathcal{I}}[\boldsymbol{F}]$. Under these conditions, we have $\underline{F}_\alpha^{self} = \underline{0}$ for all $0 \leq \xi < \xi^c$. Now, there are two possible scenarios for the behavior of $\underline{F}_\alpha^{self}$ at ξ^c.

The standard scenario predicted by MCT for many well-established model systems is characterized by $\underline{F}_\alpha^{self,c} > \underline{0}$ and by some finite localization length $0 < \Delta r_\alpha^c < \infty$ for all components $1 \leq \alpha \leq M$ of the liquid at ξ^c which means that collective and tagged-particle motion freeze in simultaneously. There is, however, also the possibility that at least for one $0 \leq \alpha \leq M$ it is $\underline{F}_\alpha^{self,c} = \underline{0}$ and thus $\Delta r_\alpha^c = \infty$, i.e. in the present case MCT predicts that the modes of the self-motion of the particles of species α at long times become decoupled from the collective ones and that the particles of species α can diffuse through the frozen-in glass matrix formed by the remaining components at ξ^c [30, 31, 32]. Under this condition, there is a further possibility that there is some $\xi^* > \xi^c$ such that $\underline{F}_\alpha^{self} > \underline{0}$ for all $\xi > \xi^*$, and $\underline{F}_\alpha^{self} = \underline{0}$ if $0 \leq \xi < \xi^*$. Assuming $\xi = \xi^* + \Delta\xi$ with $\Delta\xi > 0$, the linear dependence of $\underline{\mathcal{F}}_\alpha^{self}$ on $\underline{F}_\alpha^{self}$ in the fixed-point equation $\underline{F}_\alpha^{self} = \underline{\mathcal{I}}_\alpha^{self}[\underline{F}_\alpha^{self}]$ implies $\underline{F}_\alpha^{self} \to \underline{0}$ and thus also $\Delta r_\alpha \to \infty$ for $\Delta\xi \to 0$, i.e. in the present case MCT predicts a continuous localization-delocalization transition for the particles of species α associated with the diverging length scale Δr_α. Such a continuous transition is also called a type-A transition.

MCT predictions like the type-A transition discussed above have to be critically challenged since they involve problems. One of these problems is more or less a technical one. Explicit (both analytical and numerical) calculations are typically performed by using some discretized models where finite low wave number cutoffs have to be introduced. Thus, it can not be expected that such a model captures correctly the physics on length scales beyond the one defined by its low wave number cutoff. The second problem is even more delicate. Its origin relies on the low wave number behavior of the vertices in the tagged-particle memory kernel given by Eq. (4.12) which may lead to a failure of MCT in the description of delocalization transitions. To point out this problem more explicitly, let us consider as an example the so-called Lorentz gas model where a point-like tagged particle moves through the voids of a fixed array of spheres with radius R in d spatial dimensions. The spheres may overlap and are randomly distributed with number density n. They serve as hard obstacles at which the tagged particle is elastically scattered. For this model, one expects a delocalization-localization transition for the tagged particle upon increasing n above some critical value. The MCT expression for the tagged-particle memory kernel for the Lorentz gas model is similar to Eq. (4.12). Now, for the 3D Lorentz gas model, it can be shown that introducing a low wave number cutoff in the MCT equations leads to a qualitative change in the asymptotic behavior of the self-NEPs of the tagged particle close to the critical density, compared to the full MCT equations with continuous wave numbers without cutoff at low values [33]. For the 2D Lorentz gas model, the situation seems to be even worse. In this case, the full MCT equations with continuous wave numbers without cutoff at low values predict a localized state for the tagged particle at arbitrary small $n > 0$ [33, 34], and this prediction is in a clear contradiction to corresponding computer simulation results of Höfling and Franosch [35]. It still remains an open question how to resolve these problems on the theoretical side.

4.8 Static structure functions

As already mentioned above, the interaction potentials for a specific model system enter the MCT equations only via the static structure factors. Thus, we need some technique for a precise determination of these objects. Precision, however, is not the only criterion for the choice of some specific technique, but also efficiency in order to be able to preform systematic calculations. For a theoretical calculation of static structure factors there are two well-established complementary approaches.

The first one is to make use of the integral equation theory based on the Ornstein-

Zernike equation for mixtures to calculate the direct correlation functions $c_k^{\alpha\beta}$. The static structure factor matrix $\boldsymbol{S}$ follows then from Eq. (4.8). The Ornstein-Zernike equation for mixtures reads [36]

$$\boldsymbol{h} = \boldsymbol{c} + n\boldsymbol{c}\boldsymbol{x}\boldsymbol{h} \tag{4.43}$$

where $x_k^{\alpha\beta} = x_\alpha \delta_{\alpha\beta}$ and $h_k^{\alpha\beta}$ are the total correlation functions for given wave number k. To obtain a unique solution for $\boldsymbol{c}$, we need a so-called closure relation. The general ansatz [36] for this is

$$\ln[g^{\alpha\beta}(r)] = -u_{eff}^{\alpha\beta}(r) + h^{\alpha\beta}(r) - c^{\alpha\beta}(r), \tag{4.44}$$

$$u_{eff}^{\alpha\beta}(r) = \frac{u^{\alpha\beta}(r)}{k_B T} - d_0^{\alpha\beta}(r). \tag{4.45}$$

$g^{\alpha\beta}(r) = h^{\alpha\beta}(r) + 1$ are the pair distribution functions and $d_0^{\alpha\beta}(r)$ are called the bridge functions for which no general expression is known. Thus, every specific closure relation relies on some uncontrolled approximation scheme for $d_0^{\alpha\beta}(r)$ which also marks the main disadvantage of using an integral equation theory. The advantage is, however, that data with high numerical quality can be produced. There is no statistic noise and there are no finite size effects like in atomistic computer simulations. Furthermore, crystallization effects can explicitly be excluded.

Second, we can perform atomistic computer simulations. Since we are interested in calculating static quantities, the most efficient choice is the Monte Carlo (MC) technique [37]. The main advantage of atomistic computer simulations is that they yield exact results in the sense that these do not rely on uncontrolled approximations, in contrast to the results from integral equation theories. However, there are also some limitations. In order to study glassy behavior, we have to restrict the range of the control parameters such that no crystallization effects occur for the considered model systems. Furthermore, the numerical quality of the structure factors obtained from MC simulations are not as high as the ones obtained from integral equation theory. For instance, statistic noise and finite-size effects, which typically become dominant at small k, may lead to a violation of the strict positive-definiteness of the static structure factor matrix $\boldsymbol{S}_k$ which causes instabilities in the numerical solution of the MCT equations. Thus, when we intend to use structure factors obtained from MC simulations as input for MCT calculations, we need a clearly defined way to smooth the numerical raw data such that the condition $\boldsymbol{S} \succ \boldsymbol{0}$ is enforced.

In this thesis, depending on the considered problem, we will make use of both integral equation theories with various closure relations and MC simulations to calculate the

static input for MCT. For the general model system which we will introduce in Sect. 5.4, an efficient MC algorithm together with an automatized data smoothing procedure for the production of high-quality structure factor input for MCT obeying $\boldsymbol{S} \succ \mathbf{0}$ is described in Appendix A.1. The numerical methods for solving the Ornstein-Zernike equation for the simplified model systems which will be introduced in Sects. 6.1 and 6.2 are briefly summarized in Appendix A.2.

4.9 Summary

In this chapter we have first extended the MCT equations, which were previously published for multicomponent systems in 3D and one-component systems in arbitrary dimensions, to multicomponent systems in arbitrary dimensions. We have done this for the equations for the collective density correlators, the self-correlators, and the mean-square displacements. We have also introduced discretized versions of these equations for practical purposes. Furthermore, we have discussed the generic liquid-glass transition singularities and the corresponding asymptotic relaxation laws predicted by MCT. Thereby we have also mentioned some problems of MCT in describing localization-delocalization transitions. Finally, we have discussed two well-established techniques for the calculation of statistic structure factors which are needed as input for MCT. With this, we have now all necessary theoretical concepts and methods in hand for the purposes in this thesis, and thus we can start the next chapter by introducing the specific model systems of interest.

Chapter 5

The model system

In this chapter, we first discuss the experimental system of König et al. [26] which serves as the main motivation for the theoretical studies in the thesis. Second, we analyze theoretically the interactions between the so-called super-paramagnetic colloidal particles used in this experimental setup. Finally, we formulate an idealized model system which should capture the essential features of the system of König et al. and will be used for the theoretical investigations in this thesis.

5.1 The pending-droplet experiment

The main motivation for the theoretical investigations in this thesis originates from the experimental system of König et al. [26]. They consider a binary mixture of spherical super-paramagnetic colloidal particles inside a pending droplet. The geometry of the experimental setup is chosen such that the droplet develops a flat liquid-air interface perpendicular to the gravitational field inside the laboratory. Since the mass density of the colloidal particles is higher than the density of the solvent, gravity keeps the colloidal particles sedimented on the liquid-air interface of the pending droplet. Thus, particle motion is only possible in 2D to good accuracy. The colloidal particles are doped with ferromagnetic clusters whose sizes are small enough that at room temperature thermal energy overcomes the magnetic coupling forces between the permanent dipole moments of the different clusters inside a colloidal particle. Hence, in the absence of any external magnetic field, the magnetic moments of the clusters are randomly orientated and thus the magnetizations of the colloidal particles are zero, while in the presence of an external magnetic field the components of the magnetizations of the particles parallel to the external magnetic field become non-zero. Thus, an external magnetic field oriented perpendicular to the liquid-air interface plane leads to isotropic repulsive

dipolar interaction forces between the particles on the interface plane. König et al. can tune the strength of these forces by varying the strength of the external magnetic filed, and by video microscopy they can record particle trajectories from which various static and dynamic correlation functions can be calculated. At high enough magnetic fields, their results for the self-intermediate scattering functions clearly exhibit the stretched relaxation patterns of glass-forming liquids, see for instance Fig. 8.1 in Chapter 8. With this, the experimental system of König et al. serves as a well-suited model system for studying glass transition phenomena in 2D. Interested readers can find technical details on the experimental setup in Ref. [38].

The binary mixture used by König et al. consists of two species of particles which we call "big" (labeled by $\alpha = b$) and "small" ($\alpha = s$) in the following. For the radii R_α and magnetic susceptibilities χ_α of the super-paramagnetic colloidal particles there holds both $R_s < R_b$ and $\chi_s < \chi_b$.

5.2 Analysis of the particle interactions

Let us start with analyzing the interactions between the particles occurring in the experimental system described above.

As a first step, we remember that exposing a single super-paramagnetic colloidal particle of species α to an external magnetic field $\vec{B}$ leads to an induced magnetic moment $\vec{m}_\alpha$ of this particle for which we assume the linear response relation

$$\vec{m}_\alpha = \chi_\alpha \vec{B} \tag{5.1}$$

with the susceptibility χ_α.

Second, we have to investigate the interactions between two super-paramagnetic colloidal particles, one of species α, and the other one of species β, on the liquid-air interface plane in the presence of an external magnetic filed $\vec{B}$. In this case, Eq. (5.1) has to be modified since the magnetic field $\vec{B}_\beta$ corresponding to the magnetic moment $\vec{m}_\beta$ of the particle of species β also influences the induced magnetic moment $\vec{m}_\alpha$. The same statement holds for $\vec{m}_\beta$. For the following, we assume throughout that the external magnetic field $\vec{B}$ and thus also $\vec{m}_\alpha$ and $\vec{m}_\beta$ are perpendicular to the liquid-air interface plane and that the colloidal particles can only move along this plane. Thus, it is sufficient to consider scalar quantities $B = |\vec{B}|$, $m_\alpha = |\vec{m}_\alpha|$, etc. Furthermore, we neglect effects like Casimir interactions induced by thermal fluctuations of the liquid-air interface [39].

Now, the magnetization m_α of the particle of species α is given by

$$m_\alpha = \chi_\alpha[B + B_\beta] \tag{5.2}$$

where

$$B_\beta = -\frac{\mu_0}{4\pi}\frac{m_\beta}{r^3} \tag{5.3}$$

is the magnetic field of the polarized particle of species β acting from distance r on the particle of species α [40]. $\mu_0 = 4\pi \cdot 10^{-7}\mathrm{NA}^{-2}$ is the vacuum permeability in SI-units. Substituting Eq. (5.3) into Eq. (5.2) yields

$$m_\alpha = \chi_\alpha \left[B - \frac{\mu_0}{4\pi}\frac{m_\beta}{r^3}\right], \tag{5.4}$$

for the particle of species β we obtain similarly

$$m_\beta = \chi_\beta \left[B - \frac{\mu_0}{4\pi}\frac{m_\alpha}{r^3}\right]. \tag{5.5}$$

Eqs. (5.4) and (5.5) are two independent linear equations for m_α and m_β whose solution yields the distance-dependent magnetizations

$$m_\alpha(r) = \chi_\alpha B \left[1 - \frac{\mu_0}{4\pi}\frac{\chi_\beta}{r^3}\right]\left[1 - \left(\frac{\mu_0}{4\pi}\frac{\chi_\alpha}{r^3}\right)\left(\frac{\mu_0}{4\pi}\frac{\chi_\beta}{r^3}\right)\right]^{-1}, \tag{5.6}$$

$$m_\beta(r) = \chi_\beta B \left[1 - \frac{\mu_0}{4\pi}\frac{\chi_\alpha}{r^3}\right]\left[1 - \left(\frac{\mu_0}{4\pi}\frac{\chi_\alpha}{r^3}\right)\left(\frac{\mu_0}{4\pi}\frac{\chi_\beta}{r^3}\right)\right]^{-1}. \tag{5.7}$$

Of course, we want to keep our theoretical model system as simple as possible and thus we ask ourselves whether for the experimental system of König et al. the influence of the magnetic filed B_β on the magnetization m_α is negligible or not. To find an answer for this question, let us determine an upper limit for the r-dependent terms in Eqs. (5.6) and (5.7). Assuming that the colloidal particles can be treated as hard spherical objects with radii R_α, we obtain with the experimental values $\chi_b \cong 6.2 \cdot 10^{-11}\mathrm{Am}^2/\mathrm{T}$, $\chi_s \cong 6.6 \cdot 10^{-12}\mathrm{Am}^2/\mathrm{T}$, $2R_b \cong 4.7\mu\mathrm{m}$, and $2R_s \cong 2.8\mu\mathrm{m}$ reported by König et al. [26]

$$\frac{\mu_0}{4\pi}\frac{\chi_\alpha}{r^3} \leq \frac{\mu_0}{4\pi}\frac{\chi_b}{[R_b + R_s]^3} \cong 0.12 \tag{5.8}$$

for all possible combinations of α, β. This means that, compared to the ideal one-particle case $m_\alpha = \chi_\alpha B$, the change in m_α due to the presence of a second super-paramagnetic particle is for sure less than the maximum possible value of 12% which occurs when a small particle is in contact with a big one. Since the experiments of König et al. [26]

are carried out at 2D packing fractions on the liquid-air interface plane which are below their maximum possible values and thus the average distance between the particles is larger than $R_b + R_s$, we neglect throughout the influence of the magnetic filed B_β on the magnetization m_α in the following, and postulate the linear response relation

$$m_\alpha = \chi_\alpha B \tag{5.9}$$

for all super-paramagnetic colloidal particles on the liquid-air interface plane.

5.3 Dipole-potentials

Now, we are able to derive an approximative expression for the pair-potential of two super-paramagnetic colloidal particles on the liquid-air interface plane. For this we remember that the particles used by König et al. are doped with ferromagnetic clusters. Each of these clusters has a permanent magnetic dipole moment. By using the well-known formula for the potential energy between two permanent magnetic dipole moments [40] we obtain for the thermal average of the potential energy between two colloidal particles on the liquid-air interface plane for not too small distances r the expression

$$\left\langle E_{pot}^{\alpha\beta}(r) \right\rangle = \frac{\mu_0}{4\pi} \frac{1}{r^3} \sum_{i,j} \langle m_{\alpha,i} m_{\beta,j} \rangle \tag{5.10}$$

where $m_{\alpha,i}$ is the component of the permanent magnetic moment perpendicular to the liquid-air interface plane of cluster i inside the colloidal particle of species α, and the angular brackets stand for canonical averaging. Note that we have already dropped the contributions of the components of all magnetic moments parallel to the liquid-air interface plane. Now, the assumption that the magnetic field B_β has no influence on the magnetic moment m_α leads us to the reasonable approximation $\langle m_{\alpha,i} m_{\beta,j} \rangle \approx \langle m_{\alpha,i} \rangle \langle m_{\beta,j} \rangle$. Finally, we postulate the validity of Eq. (5.9) which yields the identity $\sum_i \langle m_{\alpha,i} \rangle = \chi_\alpha B$. We end up with an approximative expression for the dipolar pair-potential $u^{\alpha\beta}(r)$ between two super-paramagnetic colloidal particles on the liquid-air interface plane depending only on the external field B and the phenomenological material parameters χ_α, the result is

$$u^{\alpha\beta}(r) = \frac{\mu_0}{4\pi} \frac{\chi_\alpha \chi_\beta B^2}{r^3}, \quad r > R_\alpha + R_\beta. \tag{5.11}$$

Note that Eq. (5.11) is identical to the formula for the potential energy of two permanent magnetic dipole moments $m_\alpha = \chi_\alpha B$. We stress this fact because it seems that in previous works there has been some confusion concerning the right proportionality factor on the r.h.s. of Eq. (5.11) [41].

5.4 An idealized model system

The results in the previous section motivate us to introduce an idealized theoretical model system which should capture all essential features of the experimental system of König et al. [26], at least for all our practical purposes in this thesis.

We postulate an ideal binary mixture of hard disks with radii R_α in 2D which are distributed isotropically and homogeneously with total particle number density n. The mixture shall consist of "big" ($\alpha = b$) and "small" ($\alpha = s$) particles where $R_s \leq R_b$. Besides the hard-core repulsions, the particles shall also interact via the induced dipole-potentials given by Eq. (5.11), i.e. the complete pair-potentials shall be given by

$$u^{\alpha\beta}(r) = \begin{cases} \infty & , \quad r \leq R_\alpha + R_\beta, \\ \dfrac{\mu_0}{4\pi} \dfrac{\chi_\alpha \chi_\beta B^2}{r^3} & , \quad r > R_\alpha + R_\beta. \end{cases} \tag{5.12}$$

The susceptibilities shall obey $\chi_s \leq \chi_b$. The system of dipolar hard disks shall be coupled to a heath bath with temperature T and also be governed by Brownian dynamics. The single-particle short-time diffusion coefficients D_α^0 are assumed to obey the Stokes-Einstein law, i.e. we further postulate the relation

$$D_\alpha^0 / D_\beta^0 = R_\beta / R_\alpha \tag{5.13}$$

which for the system of König et al. [26] is at least approximately fulfilled. Furthermore, if the two species of particles in the experimental setup are made of the same homogeneous material, then we can translate Eq. (5.13) to

$$D_\alpha^0 / D_\beta^0 = [\chi_\beta / \chi_\alpha]^{1/3} \tag{5.14}$$

since in this case it is reasonable to assume that the susceptibility χ_α is proportional to the volume $(4/3)\pi R_\alpha^3$ of the spherical colloidal particle of species α.

5.5 Physical control parameters

At first view, the thermodynamic equilibrium state of the model system defined above depends on seven tunable physical control parameters: the total particle number density n, the two radii R_b and R_s, the two susceptibilities χ_b and χ_s, the system temperature T, and the strength of the magnetic field B. Note that the thermodynamic equilibrium state does not depend on the two diffusion constants D_b^0 and D_s^0. Since the thermodynamic equilibrium state is not dependent on the used unit system, one of the parameters can be eliminated by choosing the unit length appropriately. Furthermore, since the Boltzmann factor in the canonical ensemble only depends on the ratio of potential and thermal energy, only five independent control parameters remain. The question now is: how to choose these five control parameters appropriately? Of course, there is no unique answer to this question. A minimum requirement, however, is that all five independent control parameters shall be dimensionless. The comparison of our binary model system to much simpler one-component models will guide us to a natural choice of these dimensionless variables.

Let us first focus on the hard-core repulsions by assuming $B = 0$. Let us further assume for the moment $R_b = R_s$. In this special case our model system defines a one-component system consisting of hard disks. It is well-known that the thermodynamic equilibrium state of this simple system depends on the packing fraction φ only which is the area occupied by the disks divided by the complete system area. Dropping the restriction $R_b = R_s$ leads us to an ideal system of binary hard disks. For some practical purposes, such a studying so-called mixing effects, one intends to compare properties of such a binary system to those of a corresponding one-component system. For such a comparison it is reasonable to require that both systems have the same packing fraction. Thus, it turns out to be convenient to choose the total packing fraction

$$\varphi = n\pi(x_b R_b^2 + x_s R_s^2) \tag{5.15}$$

as one of the independent control parameters. The thermodynamic state of the binary mixture of hard disks is then fully characterized by specifying one of the particle number concentrations, say that of the smaller ones

$$x_s = N_s/(N_b + N_s), \tag{5.16}$$

and the size ratio

$$\delta_R = R_s/R_b. \tag{5.17}$$

Now, let us focus on the dipolar interactions by assuming $R_\alpha = 0$. If we further assume $\chi_b = \chi_s = \chi_0$, then we end up with a one-component model of point dipoles in 2D. For this simple model system it is easy to verify that its thermodynamic equilibrium state only depends on the dimensionless parameter $\Gamma_0 = n^{3/2}\frac{\mu_0}{4\pi}\frac{m_0^2}{k_BT}$ where k_BT is the thermal energy and $m_0 = \chi_0 B$ the magnetization per particle. Dropping the restriction $\chi_b = \chi_s$ leads us to a model of binary point dipoles in 2D. In this case, the (averaged) magnetization per site is given by $m = [x_b\chi_b + x_s\chi_s]B$. As already stated above, for the study of mixing effects one intends to compare properties of a binary system to those of a corresponding one-component system. In the present case, it is reasonable to require for such a comparison that density n, thermal energy k_BT, and magnetization per site m are identical for the two considered systems. Thus, it turns out to be convenient to generalize the expression for Γ_0 and to choose to so-called interaction parameter

$$\Gamma = (\pi n)^{3/2}\frac{\mu_0}{4\pi}\frac{[x_b\chi_b + x_s\chi_s]^2 B^2}{k_BT} \tag{5.18}$$

as one of the independent control parameters. The thermodynamic equilibrium state of the binary mixture of point dipoles is then fully characterized by specifying one of the particle number concentrations, say that of the smaller ones given by Eq. (5.16), and the susceptibility ratio

$$\delta_\chi = \chi_s/\chi_b. \tag{5.19}$$

The prefactor $\pi^{3/2}$ in Eq. (5.18) was introduced to match the convention used in Ref. [26].

With Eqs. (5.15)-(5.19) we have found a reasonable choice for the five independent physical control parameters which we will use in the following to characterize the thermodynamic equilibrium state of our idealized model system specified above.

5.6 Summary

In the present chapter, we have briefly described the basic principles of the experimental system of König et al. [26]. We have analyzed theoretically the interactions between super-paramagnetic colloidal particles within this experimental setup. An important result of this analysis was that the effect of mutual polarization of the particles is negligible. Based on this insight, we have introduced an idealized 2D model system which should capture all essential features of the system of König et al. In the next chapter, we will see that under certain conditions this model system can be further simplified but also generalized. It is the main intention of this thesis to study glass transition phenomena in 2D by applying MCT to these simplified model systems.

Chapter 6

Simplified model systems

In this chapter, we discuss two simplified versions of the model system introduced in Sect. 5.4. The first one is obtained by dropping the dipolar interactions and the restriction $d = 2$, and the second one by neglecting the hard-core repulsions. For both systems, the thermodynamic equilibrium state will depend on three independent control parameters. Thus, for both systems the set of liquid-to-glass transition points predicted by MCT will form a locally smooth critical surface. Both of these surfaces can be interpreted as a set union of glass transition lines as introduced in Sect. 4.5. For both model systems, we will study symmetry properties of special glass transition lines within a common mathematical framework.

6.1 Binary mixtures of d-dimensional hard spheres

By assuming that the external magnetic field is switched off, i.e. $B = 0$, the model system introduced in Sect. 5.4 reduces to a binary mixture of hard disks in 2D. Since one of our intentions in this thesis is to study also the influence of the spatial dimension d on the glass transition, let us drop here the restriction $d = 2$ and postulate a model system consisting of a binary mixture of hard spherical particles in d dimensions. The thermodynamic equilibrium state is then fully characterized by three independent control parameters: the total d-dimensional packing fraction

$$\varphi = n(\Omega_d/d)(x_b R_b^d + x_s R_s^d), \tag{6.1}$$

the particle number concentration x_s of the smaller spheres given by Eq. (5.16), and the ratio of the radii of the smaller and bigger spheres δ_R given by Eq. (5.17). The single-particle short-time diffusion coefficients D_α^0 are assumed to obey the Stokes-Einstein law

according to Eq. (5.13).

Later, we will dedicate a complete chapter in this thesis for a detailed MCT study for the present model system for the cases $d = 2$ and $d = 3$. While for sufficiently low φ it will behave liquid-like, MCT will predict vitrification at high enough φ. The set of generic MCT liquid-to-glass transition singularities will form a locally smooth critical surface which we can represent as $\varphi^c(x_s, \delta_R)$. The following limiting cases are obvious:

$$\varphi^c(x_s, 1) \equiv \varphi^c(0, \delta_R) \equiv \varphi^c(1, \delta_R) \equiv \varphi_0^c \tag{6.2}$$

where φ_0^c is the critical packing fraction for the corresponding monodisperse system. Furthermore, an interchange of the roles of the big and small spheres leads to the same physical scenario. Therefore it is

$$\varphi^c(x_s, \delta_R) = \varphi^c(1 - x_s, 1/\delta_R). \tag{6.3}$$

We will discuss some consequences of these symmetry properties in Sect. 6.3.

6.2 Binary mixtures of point dipoles in 2D

So far, we have kept secret that the colloidal dispersion used by König et al. [26] is strongly diluted where the average distance between the particles exceeds the diameter of the bigger particles roughly by a factor of four. With this information we can estimate $\varphi < (4 \cdot 2R_b)^{-2}\pi R_b^2 = \pi/64 \cong 0.05$ for the total 2D packing fraction on the interface plane. Therefore, collisions of the hard cores of two particles practically never occur if the interaction parameter Γ is high enough, and thus the thermodynamic equilibrium state of the experimental system close to vitrification should be completely determined by the induced dipole-potentials.

Idealizing this picture, we assume a binary mixture of point particles in 2D interacting via the induced dipole-potentials

$$u^{\alpha\beta}(r) = \frac{\mu_0}{4\pi} \frac{\chi_\alpha \chi_\beta B^2}{r^3}. \tag{6.4}$$

The thermodynamic equilibrium state is then fully determined by three independent control parameters: the particle number concentration x_s of the smaller dipoles given by Eq. (5.16), the interaction parameter Γ given by Eq. (5.18), and the ratio of the susceptibilities of the smaller and bigger dipoles δ_χ given by Eq. (5.19). Note that although we have assumed point particles, the two species of particles shall be called

"big" ($\alpha = b$) and "small" ($\alpha = s$) in the sense that $\chi_b \geq \chi_s$. Furthermore, we have to remember that although we have neglected the hard-core repulsions, the particles in the experimental setup still remain spherical particles with finite radii. Thus, for the calculation of time-dependent quantities for our idealized model of point dipoles we keep on postulating that the single-particle short-time diffusion coefficients D_α^0 remain finite and optionally even obey the version of the Stokes-Einstein law given by Eq. (5.14).

Later, we will dedicate a complete chapter in this thesis for a detailed MCT study for the binary point dipole model in 2D. While for sufficiently low Γ it will behave liquid-like, MCT will predict vitrification at high enough Γ. The set of generic MCT liquid-to-glass transition singularities will form a locally smooth critical surface which we can represent as $\Gamma^c(x_s, \delta_\chi)$. Similarly to the binary d-dimensional hard sphere model in the previous section, there hold the symmetry relations

$$\Gamma^c(x_s, 1) \equiv \Gamma^c(0, \delta_\chi) \equiv \Gamma^c(1, \delta_\chi) \equiv \Gamma_0^c, \tag{6.5}$$

$$\Gamma^c(x_s, \delta_\chi) = \Gamma^c(1 - x_s, 1/\delta_\chi). \tag{6.6}$$

Γ_0^c is the critical interaction parameter for the corresponding monodisperse system. In the next section, we will analyze some consequences of these symmetry properties.

6.3 Glass transition lines

The symmetry relations in the two previous sections motivate us to discuss some features of the critical surface $\varphi^c(x_s, \delta_R)$ for the d-dimensional binary hard sphere model and those of $\Gamma^c(x_s, \delta_\chi)$ for the binary point dipole model in 2D within a common framework. For the following, let us introduce the space-holder variables $\xi \in \{\varphi, \Gamma\}$ and $\delta \in \{\delta_R, \delta_\chi\}$. The "critical surface" $\xi^c(x_s, \delta)$ shall then stand for both $\varphi^c(x_s, \delta_R)$ for the d-dimensional binary hard sphere model and $\Gamma^c(x_s, \delta_\chi)$ for the binary point dipole model in 2D.

Let us first note that fixing δ to some specific value in $\xi^c(x_s, \delta)$ defines a glass transition line which is a function of x_s. The critical surface $\xi^c(x_s, \delta)$ is then nothing but the set union of all these glass transition lines corresponding to different values of δ. Numerical methods for the determination of such lines can be found in Appendix A.3. The slope of a glass transition line can be calculated by specializing Eq. (2.26) to

$$\left.\frac{\partial \xi^{crit}}{\partial x_s}\right|_{(x_s,\delta)=(x_s^c,\delta^c)} = -\left.\frac{\partial\sigma/\partial(\Delta x_s)}{\partial\sigma/\partial(\Delta\xi)}\right|_{(\Delta\xi,\Delta x_s,\Delta\delta)=\vec{0}}. \tag{6.7}$$

One of the important aspects of this thesis will be the demonstration of the predictive

power of Eq. (6.7) for the so-called weak-mixing limits $x_s = 0$ and $x_b = 0$, since the knowledge of the initial slopes of a glass transition line for both limits is already sufficient to predict some of its qualitative features. For instance, if $(\partial\xi^c/\partial x_s)(x_s = 0, \delta)$ is positive (negative), the liquid (glass) is stabilized upon adding a small concentration of small particles into the one-component liquid consisting of the bigger ones. If $(\partial\xi^c/\partial x_s)(x_s = 0, \delta)$ and $(\partial\xi^c/\partial x_b)(x_b = 0, \delta)$ are both positive (negative), then the corresponding glass transition line has at least one maximum (minimum). Furthermore, if for two values, δ_1 and δ_2, it is $(\partial\xi^c/\partial x_s)(x_s = 0, \delta_1) < (\partial\xi^c/\partial x_s)(x_s = 0, \delta_2)$ and $(\partial\xi^c/\partial x_b)(x_b = 0, \delta_1) > (\partial\xi^c/\partial x_b)(x_b = 0, \delta_2)$, i.e. $(\partial\xi^c/\partial x_s)(x_s = 1, \delta_1) < (\partial\xi^c/\partial x_s)(x_s = 1, \delta_2)$, then the glass transition lines for δ_1 and δ_2 have an odd number of intersection points and therefore at least one crossing. Otherwise the number of intersection points is even. The essential steps for the calculation of the slope $\partial\xi^c/\partial x_s$ are explained in Appendix B.

Now, let us turn to the symmetry properties of the glass transition lines. We can translate Eqs. (6.2), (6.3), (6.5), and (6.6) to

$$\xi^c(x_s, 1) \equiv \xi^c(0, \delta) \equiv \xi^c(1, \delta) \equiv \xi_0^c, \tag{6.8}$$

$$\xi^c(x_s, \delta) = \xi^c(1 - x_s, 1/\delta). \tag{6.9}$$

ξ_0^c is the critical coupling parameter for the corresponding monodisperse system. Now, let us assume a binary system whose two species of particles are almost identical, i.e. $0 < (1 - \delta) \ll 1$. Then, with Eq. (6.8) we can write

$$\xi^c(x_s, \delta) = \xi_0^c + (1 - \delta)\xi_1^c(x_s) + (1 - \delta)^2\xi_2^c(x_s) + \mathcal{O}[(1 - \delta)^3], \tag{6.10}$$

$$\xi_i^c(0) = \xi_i^c(1) = 0, \quad i = 1, 2. \tag{6.11}$$

Eq. (6.9) implies for the coefficient functions

$$\xi_1^c(x_s) = -\xi_1^c(1 - x_s), \tag{6.12}$$

$$\xi_2^c(x_s) = \xi_2^c(1 - x_s) - \xi_1^c(1 - x_s). \tag{6.13}$$

We can conclude: if $\xi_1^c(x_s)$ is a non-vanishing function for almost all x_s, then we obtain to leading order in $(1 - \delta)$ glass transition lines which, after subtracting ξ_0^c, are anti-symmetric with respect to the equimolar composition $x_s = 1/2$, i.e. in this case we can write

$$[\xi^c(x_s, \delta) - \xi_0^c] \cong -[\xi^c(1 - x_s, \delta) - \xi_0^c], \tag{6.14}$$

$$\xi^c(1/2, \delta) \cong \xi_0^c. \tag{6.15}$$

If, however, there holds

$$\xi_1^c(x_s) = 0 \tag{6.16}$$

for all x_s while $\xi_2^c(x_s)$ is a non-vanishing function for almost all x_s, then Eqs. (6.10) and (6.13) imply

$$\xi^c(x_s, \delta) \cong \xi^c(1 - x_s, \delta) \tag{6.17}$$

which means that the glass transition lines become symmetric with respect to $x_s = 1/2$ if the two species of particles become almost identical. There holds also the (somewhat weaker) inverse statement. If Eq. (6.17) is assumed to be true for $0 < (1 - \delta) \ll 1$, then Eq. (6.12) implies Eq. (6.16). For the slopes $s_\alpha^c(\delta) = (\partial \xi^c / \partial x_\alpha)(x_\alpha = 0, \delta)$ of a glass transition line we can formulate further special (numerically testable) conclusions from Eq. (6.16):

$$(\partial s_\alpha^c / \partial \delta)(\delta = 1) = 0. \tag{6.18}$$

In order to come to the point, let us note already here that in the following chapters we will be able to produce numerical results with sufficiently high accuracy to demonstrate that Eqs. (6.17) and (6.18), and thus also Eq. (6.16), are indeed valid for both the d-dimensional binary hard sphere model and the binary point dipole model in 2D. These results exclude the possibility of the occurrence of antisymmetric glass transition lines according to Eqs. (6.14) and (6.15) for the model systems considered here.

6.4 Summary

By simplifying but also generalizing the model system introduced in Sect. 5.4 we have introduced two special model systems, the d-dimensional binary hard sphere model and the binary point dipole model in 2D. For both of them we will present detailed MCT studies in the next chapters. For both systems the set of liquid-to-glass transition points predicted by MCT will form a locally smooth critical surface. These surfaces can be interpreted as set unions of special glass transition lines. Without using MCT, we have discussed already in this chapter some general properties of these special glass transition lines for both models within a common mathematical analysis. We have derived two possible scenarios for the behavior of these glass transition lines for the case that the two species of particles within the considered binary mixtures become almost identical: the glass transition lines may then become antisymmetric or symmetric with respect to the equimolar composition. As already anticipated, the numerical results in the following

chapters will demonstrate that for the two considered model systems here the symmetric case applies.

Chapter 7

Binary mixtures of hard disks/spheres

In this chapter, we present a detailed MCT study on the simplified model system introduced in Sect. 6.1, i.e. the d-dimensional binary hard sphere model where we will restrict our numerical studies to the cases $d = 2$ and $d = 3$. The comparison of the results for 2D and 3D will provide information about the influence of the spatial dimensionality d on the glass transition behavior and in particular on the occurring mixing effects.

We further specify: the wave number k shall be discretized according to Eq. (4.16). For the offset, following previous works, we choose $\hat{o}_2 = 0.303$ for $d = 2$ [18] and $\hat{o}_3 = 0.5$ for $d = 3$ [25]. The choice $K = 250$ and $\Delta k = 0.3$ turns out to be sufficiently accurate to avoid larger discretization effects. For calculations with finite concentrations of both particle species, the unit length shall be given by the diameter $2R_b$ of the bigger particles, and, if not stated explicitly otherwise, the short-time diffusion coefficients D_α^0 shall be assumed to obey the Stokes-Einstein law according to Eq. (5.13). Furthermore, the unit of time is then chosen such that $D_\alpha^0 = 0.01/(2R_\alpha)$. To perform calculations in the weak-mixing limits $x_\alpha \to 1$ it is more convenient to choose the diameters $2R_\alpha$ of the majority particle species as unit length. Static structure factor input for MCT is taken from the Percus-Yevick (PY) theory, see Appendix A.2.1 for technical details. The algorithm for the numerical calculation of time-dependent correlation functions is specified in Appendix A.4.

7.1 Previous results

Let us briefly summarize some important MCT results which have been already published before for the current model system. We first focus on the monodisperse case, i.e. $\delta_R = 1$. For hard spheres in 3D, Franosch et al. [24] have precisely calculated the critical MCT packing fraction for the ideal liquid-glass transition. Their result has been

$\varphi_0^c \cong 0.516$ ($d = 3$). A comparison to corresponding dynamic light scattering results of Henderson et al. [42] for almost monodisperse colloidal suspensions demonstrates that MCT tends to overestimate the glass formation, their widely accepted experimental value is $\varphi_{exp}^c \cong 0.578$. The first MCT calculations in 2D were performed by Bayer et al. [18] for monodisperse hard disks. They have found an ideal liquid-glass transition at the critical packing fraction $\varphi_0^c \cong 0.697$ ($d = 2$) and they have demonstrated that the qualitative liquid-to-glass transition scenario in 2D is very similar to the 3D case. Furthermore, Bayer et al. have demonstrated that the ratios of the critical MCT packing fractions φ_0^c and the corresponding values φ_0^{rcp} for the random close packing fractions are very similar for 2D and 3D, it is $\varphi_0^c/\varphi_0^{rcp} \cong 0.83$ ($d = 2$) and $\varphi_0^c/\varphi_0^{rcp} \cong 0.81$ ($d = 3$). One of our most important results in this chapter will be to demonstrate that the similarity of the two numbers above is probably not just by chance: we will provide the first systematic comparison of the glass transition lines predicted by MCT for binary mixtures of hard disks in 2D to corresponding random close packing lines obtained from computer simulations. There will be a striking similarity between the results from both approaches. Let us finally remark that Schmid and Schilling [22] have recently calculated the critical MCT packing fraction for monodisperse d-dimensional hard spheres for high dimensions. They have found the asymptote $\varphi_0^c(d) \sim d^2 2^{-d}$ analytically. The same result was found independently by Ikeda and Miyazaki [43] numerically.

Now, let us turn to binary liquids. The first MCT calculations on multicomponent liquids were performed by Barrat and Latz [4] for binary soft spheres. However, Götze and Voigtmann [25] were the first ones studying systematically the effect of composition changes on the glass transition behavior for binary hard spheres in 3D. They have found four mixing effects.

(i) For small size disparities the glassy regime is enhanced. For $0.8 \lesssim \delta_R < 1$ it is $\varphi^c(x_s, \delta_R) < \varphi_0^c$ if $0 < x_s < 1$.

(ii) For larger size disparities the liquid state is stabilized, i.e. for $0.3 \leq \delta_R \lesssim 0.6$ it is $\varphi^c(x_s, \delta_R) > \varphi_0^c$ if $0 < x_s < 1$. This effect is also called plasticization.

(iii) Upon increasing the concentration x_s of the smaller particles the NEPs, and thus also the plateau values of the normalized correlation functions $\Phi_k^{\alpha\alpha}(t)/S_k^{\alpha\alpha}$ in the liquid regime for intermediate times, increase for not too small k and all x_s.

(iv) Starting with $x_s = 0$ and increasing the concentration x_s of the smaller particles leads for not too large k to a slowing down of the relaxation of the normalized

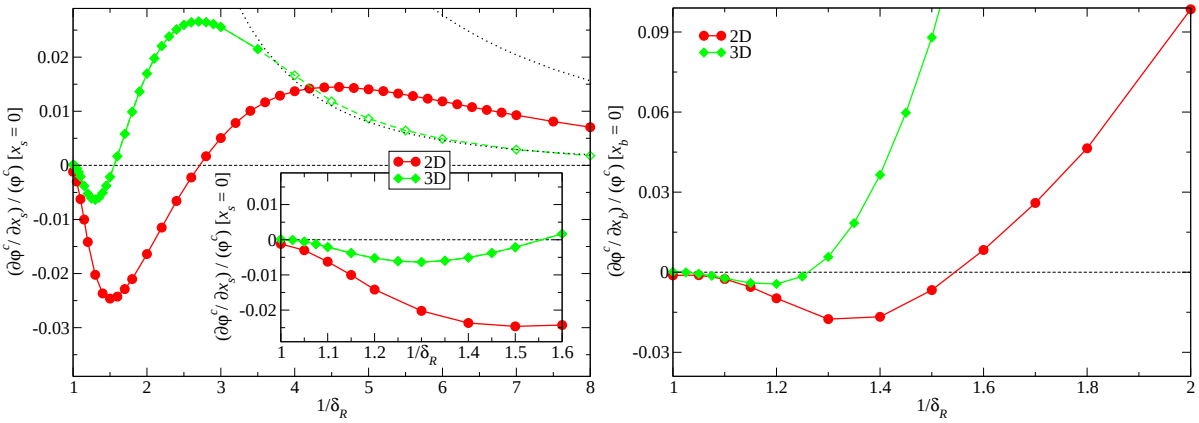

Figure 7.1: Left panel: Normalized slopes of the glass transition lines at $x_s = 0$ for the binary hard sphere models in 2D and 3D. It is $\varphi_0^c \cong 0.6914$ for $d = 2$ and 0.5159 for $d = 3$. The dotted lines show the asymptotes given by Eq. (7.1) for 2D and 3D (from right to left). For $1/\delta_R > 3.5$ in the 3D model, the tagged-particle NEPs indicate a delocalization transition of the smaller spheres. This regime is indicated by open symbols (see text). The inset presents the slopes on a much finer scale very close to $\delta_R = 1$. Right panel: Slopes of the glass transition lines at $x_b = 0$.

correlators $\Phi_k^{bb}(t)/S_k^{bb}$ of the big particles towards their plateaus in the sense that the $\Phi_k^{bb}(t)/S_k^{bb}$ versus $\log_{10}(t)$ curve becomes flatter upon increasing x_s.

These results qualitatively agree with those from dynamic light scattering experiments [42, 44] and molecular dynamics simulations [45, 46]. In contrast to this, a recent theory of Juárez-Maldonado and Medina-Noyola based on the self-consistent generalized Langevin equation (SCGLE) [47] predicts a plasticization effect also for size ratios close to unity and the authors argue that the data available from simulations and experiments are not sufficiently accurate to rule out the opposite scenario.

In the following, we will demonstrate in the framework of MCT that the four mixing effects cited above are also observable for binary hard disks in 2D where the effect (i) will be more strongly pronounced as in the 3D case. Furthermore, we will show that at least on a qualitative level all four mixing effects are also observable in corresponding computer simulation results for binary hard disk in 2D.

7.2 Mode-coupling results

Now, we can start to present our numerical MCT results for binary hard disks/spheres.

7.2.1 Glass transition lines

Let us first demonstrate the predictive power of our slope formula, Eq. (6.7), by applying it to the so-called weak-mixing limits $x_\alpha \to 0$. The technical procedure for this is described in Appendix B.

The left panel in Fig. 7.1 shows normalized slopes of the glass transition lines at $x_s = 0$ as functions of the inverse size ratio $1/\delta_R$ for the binary hard sphere models in 2D and 3D. The qualitative behavior of the slope curves is the same for the two models. By definition, the case $\delta_R = 1$ represents a one-component system in both 2D and 3D with critical packing fraction $\varphi(x_s, \delta_R = 1) \equiv \varphi_0^c$, and thus the slopes have to be zero at this point. The numerical results for the 3D model clearly support this statement. For the 2D model, the data slightly deviate from zero at $x_s = 0$. This, however, is an artifact due to the numerically calculated static structure factors in 2D, see also Appendix A.2.1. For the 3D model, we have used the analytical solution for the PY structure factors to calculate the static input for MCT which has led to a better self-consistency at $\delta_R = 1$ than for the 2D model. For δ_R close to unity, the slopes become negative. This implies that adding a small concentration of small particles into a one-component liquid consisting of big particles leads to a decrease in the critical packing fraction φ^c. In this sense, mixing stabilizes the glass. After exhibiting a minimum at δ_R^-, the slopes become zero again at δ_R^0 and remain positive for $0 < \delta_R < \delta_R^0$. In this region, adding a small concentration of small particles into a one-component liquid consisting of big particles leads to an increase in the critical packing fraction φ^c. In this sense, mixing stabilizes the liquid which is nothing but the well-known plasticization effect. Upon further decreasing δ_R, the slopes exhibit a maximum at δ_R^+ and indicate a monotonic decay for asymptotically small δ_R. For the 2D model, this decay is more stretched than for the 3D case.

The right panel in Fig. 7.1 displays normalized slopes of the glass transition lines at $x_b = 0$ for the binary 2D and 3D hard sphere models. Again, the qualitative behavior of the slope curves is the same for 2D and 3D. For δ_R close to unity, the slopes are negative, which means that adding a small concentration of big particles into a one-component liquid consisting of small particles leads to a stabilization of the glass. The slope exhibits a minimum at $\tilde{\delta}_R^- > \delta_R^-$. It vanishes at $\tilde{\delta}_R^0 > \delta_R^0$ followed by a strongly increasing plasticization effect for smaller δ_R.

Let us also try to understand at least some facets of the behavior of the slope curves presented in Fig. 7.1. At this point we have to be honest and state that we have no intuitive physical picture for the origin of the stabilization of the glass upon mixing. Thus, let us restrict to the case $0 < \delta_R \ll 1$. For $0 < x_s \ll 1$, we can assume that the

few small particles fit into the voids between the bigger ones and thus the glass transition is mainly driven by the cage effect of the big particles. Neglecting possible depletion interactions between the big particles due to the presence of the smaller ones [48], we can write down $\varphi_b = \varphi_0^c$ with the critical packing fraction φ_0^c for the monodisperse system as a criterion for vitrification. With $\varphi^c = \varphi_0^c + \varphi_s$ we arrive at

$$(\partial\varphi^c/\partial x_s)(x_s = 0, 0 < \delta_R \ll 1) = \varphi_0^c(\delta_R)^d. \tag{7.1}$$

The dotted lines on the left panel of Fig. 7.1 demonstrate that Eq. (7.1) indeed describes the numerical data for the 3D model well for $1/\delta_R \geq 4.0$. For the 2D case, we would need precise numerical data for much smaller δ_R than the ones shown in Fig. 7.1 to test the validity of Eq. (7.1). Such precise data are actually not available, due to difficulties in the numerical calculation. We can also try to describe the case $0 < \delta_R \ll 1$, $0 < x_b \ll 1$ analogously. Our hypothesis here is that the rarely distributed large particles have no influence on the local caging between the smaller ones which drive the glass transition. We arrive at

$$(\partial\varphi^c/\partial x_b)(x_b = 0, 0 < \delta_R \ll 1) = \varphi_0^c(\delta_R)^{-d}. \tag{7.2}$$

To test the validity of Eq. (7.2), we would need precise numerical data for much smaller δ_R than the ones shown in Fig. 7.1 which are actually not available, again for technical reasons. At least, the data on the right panel of Fig. 7.1 and Eq. (7.2) have the common qualitative feature that the increase of the slope curve for small δ_R is faster for 3D than for 2D.

For the 3D model, we observe a continuous transition of the tagged-particle NEPs $F_{s,k}^{self,c}$ to zero by approaching $\delta_R \cong 1/4$ from above, see the right panel of Fig. 7.2. This indicates a delocalization transition of the smaller spheres in the glass formed by the bigger ones [30, 31, 32]. As already discussed in Sect. 4.7, the current version of MCT can not describe several details of such a type-A transition correctly. Since the evaluation of Eq. (6.7) at $x_s = 0$ requires $F_{s,k}^{self,c}$ as input (see Appendix B.3.3), we show the corresponding data for $1/\delta_R > 3.5$ in Fig. 7.1 with open symbols. For our choice of the low wave number cutoff, the MCT model does not yield a delocalization transition in 2D, even if we use the PY result for a point-like tracer particle as static input, see the left panel of Fig. 7.2. This result might be physically correct but also might be just an artifact of MCT, see the comments on the 2D Lorentz gas model in Sect. 4.7. However, the 2D data for the slopes at small δ_R show the same qualitative behavior as the corresponding ones for the 3D model which indicates that at least the qualitative x_s-dependence of φ^c should not be too strongly influenced by the problems of MCT in

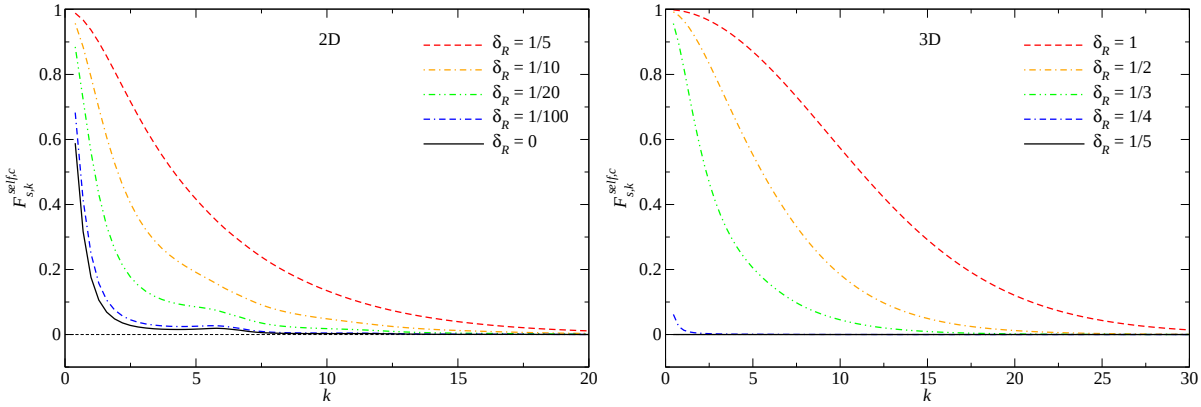

Figure 7.2: Left panel: Critical tagged-particle NEPs of a single small hard disk inside the 2D glass matrix formed by the bigger disks at their critical packing fraction. The data indicate an arrested state even for $\delta_R = 0$, i.e. for a point-like tracer particle. Right panel: Critical tagged-particle NEPs of a single small hard sphere inside the 3D glass matrix formed by the bigger spheres at their critical packing fraction. The data indicate a delocalization transition for the small particle at $\delta_R \cong 1/4$.

describing type-A transitions.

So far, the results for the slopes in Fig. 7.1 allow us to predict qualitative properties of the glass transition lines which we will verify below. Both $x_s = 0$ and $x_b = 0$ define one-component models with the same critical packing fraction φ_0^c. Hence for $\tilde{\delta}_R^0 < \delta_R < 1$ the glass transition lines have at least one minimum. If $\delta_R^0 < \delta_R < \tilde{\delta}_R^0$, then the glass transition lines exhibit at least one minimum and one maximum. For $0 < \delta_R < \delta_R^0$, the glass transition lines have at least one maximum. As an additional result, we find for both 2D and 3D that the slope curves $s_\alpha^c(\delta_R) = (\partial\varphi^c/\partial x_\alpha)(x_\alpha = 0, \delta_R)$ for $\alpha = b$ and $\alpha = s$ become almost identical for $0 < (1 - \delta_R) \ll 1$ (not shown in the figures). Furthermore, the numerical data in Fig. 7.1 indicate $(\partial s_\alpha^c/\partial\delta_R)(\delta_R = 1) = 0$. Hence, from the discussion in Sect. 6.3 we expect that the glass transition lines become symmetric with respect to the equimolar composition $x_s = 1/2$ in the limit of small size disparity which implies that the linear contribution in the Taylor series of $\varphi^c(x_s, \delta_R)$ with respect to $0 < (1 - \delta_R) \ll 1$ vanishes.

Now, let us present numerically calculated glass transition lines. The technical procedure for the determinations of $\varphi^c(x_s, \delta_R)$ is described in Appendix A.3.1. The left panel in Fig. 7.3 shows our results for the relative variation $(\varphi^c - \varphi_0^c)/\varphi_0^c$ of the glass transition lines for the binary hard disk model in 2D. Results of Götze and Voigtmann for the corresponding hard sphere model in 3D [25] are shown in the inset in Fig. 7.3. The shapes of all shown lines are fully consistent with our predictions from the slopes above: the transition lines for the largest δ_R show a single minimum and are indeed

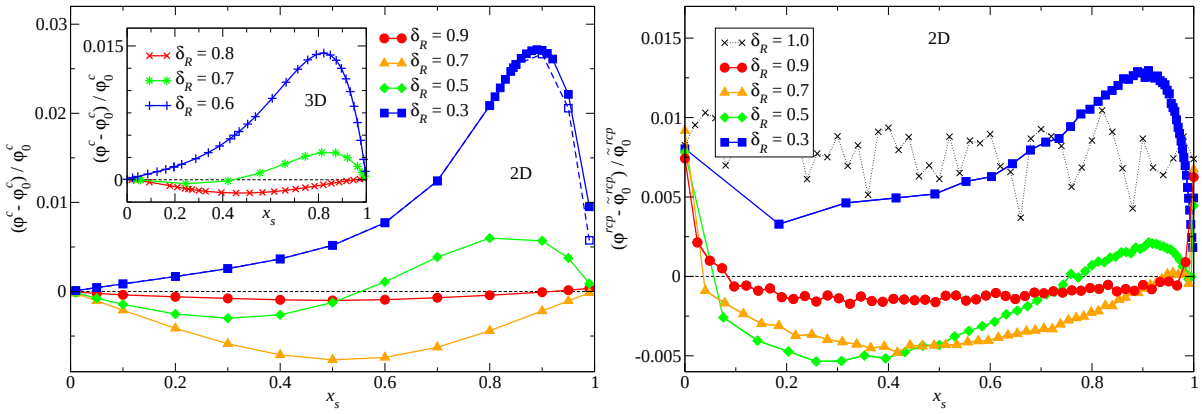

Figure 7.3: Left panel: Relative variation of the glass transition lines for the binary hard disk model in 2D. The open squares calculated with $K = 400$ grid points (instead of $K = 250$) give an estimate for the error due to the high wave number cutoff. Inset: Relative variation of the glass transition lines for the binary hard sphere model in 3D using the numerical data of Götze and Voigtmann [25] calculated with $\Delta k = 0.4$ and $K = 200$. Right panel: Relative variation of the random close packing fraction using the numerical data of Okubo and Odagaki [49]. $\tilde{\varphi}_0^{rcp}$ is chosen such that the relative variation vanishes below but close to $x_s = 1$ (see text).

almost symmetric with respect to $x_s = 1/2$. Furthermore, a numerical test for $x_s = 1/4$ has confirmed a quadratic dependence on $0 < (1 - \delta_R) \ll 1$ for both 2D and 3D (not shown in the figures). For intermediate values for δ_R, the glass transition lines become S-shaped with one minimum followed by one maximum. For the smallest values for δ_R, the transition lines exhibit a single maximum.

From our numerical MCT results we can read off the following trend: compared to the 3D model, the stabilization of the glass is much more pronounced in the 2D model where the less pronounced plasticization effect only sets in at smaller size ratios. For instance, the maximum relative decrease in φ^c occurring at $\delta \cong 0.7$ in 2D (see the left panel in Fig. 7.3) is about five times larger than the maximum downshift in φ^c in 3D which occurs at $\delta \cong 0.8$ (see the inset in Fig. 7.3 and also Fig. 2 in Ref. [25]). On the qualitative level, however, the binary hard disk model in 2D exhibits the same two mixing effects on φ^c as have been reported before by Götze and Voigtmann [25] for the binary hard sphere model in 3D.

So far, we have presented results for mixing effects on the glass transition based on MCT which is based on uncontrolled approximations. Thus, we may ask ourselves whether these results have anything to do with reality or not. Remember for instance that the SCGLE theory [47], which is also based on uncontrolled approximations, does not predict a stabilization of the glass upon mixing for binary hard spheres in 3D as MCT does. As far as we know, this theory has never been applied to a 2D model.

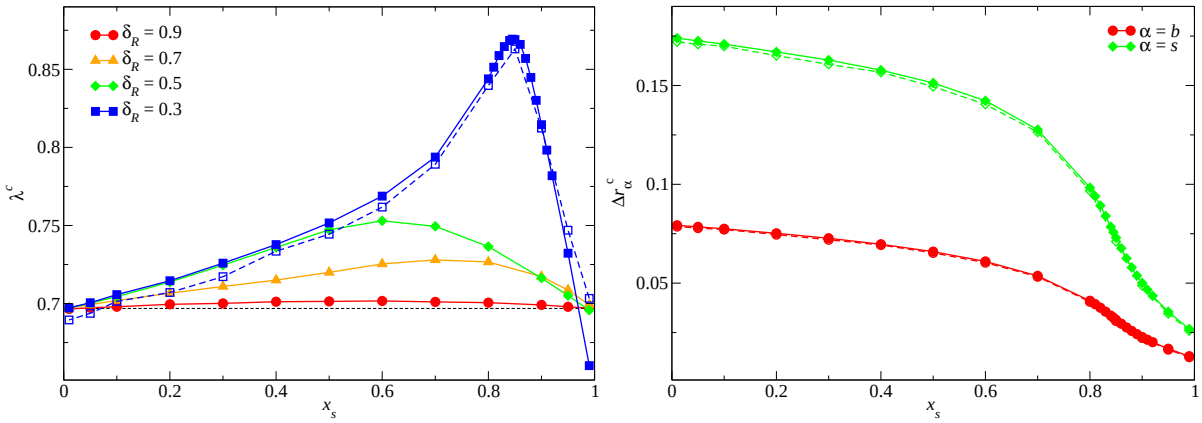

Figure 7.4: Left panel: Exponent parameters for the binary hard disk model in 2D. The horizontal dashed line marks the value for monodisperse hard disks. The open squares were calculated with $K = 400$ grid points instead of $K = 250$ showing that the influence of the high wave number cutoff becomes dominant for $x_s \to 1$. The systematic deviations occurring also for smaller x_s result from the fact that for the $K = 400$ model the values for φ^c were calculated only with an absolute error of 10^{-5} instead of 10^{-7} as done for the $K = 250$ case. Right panel: Critical localization length for the binary hard disk model in 2D at $\delta_R = 0.3$. The open symbols were calculated with $K = 400$ grid points instead of $K = 250$ demonstrating that Δr_α^c is not as sensitive to K and the error in φ^c as λ^c is.

To proceed, let us remember that Bayer et al. [18] have pointed out for monodisperse systems that there seems to be a connection between the critical MCT packing fraction φ^c and the random close packing fraction φ^{rcp}. The only fundamental problem in such considerations is the fact that random close packing is not uniquely defined and therefore depends on the procedure how it is realized. For the following, let us ignore this problem and consider random close packing values φ^{rcp} for binary hard disks in 2D calculated numerically by Okubo and Odagaki [49] by using a so-called infinitesimal gravity protocol. Our goal is now to compare the relative variation $(\varphi^c - \varphi_0^c)/\varphi_0^c$ of the critical MCT packing fraction for binary hard disks in 2D to corresponding random close packing values $(\varphi^{rcp} - \tilde{\varphi}_0^{rcp})/\tilde{\varphi}_0^{rcp}$ with some appropriately chosen $\tilde{\varphi}_0^{rcp}$. The data of Okubo and Odagaki [49] exhibit large uncertainties in the monodisperse limits $x_s = 0$, $x_s = 1$, and $\delta_R = 1$. This might result from the fact that for monodisperse hard disks the applied procedure tends to build up locally ordered structures. Thus, we have decided to choose $\tilde{\varphi}_0^{rcp} \cong 0.8139$ such that the relative variation $(\varphi^{rcp} - \tilde{\varphi}_0^{rcp})/\tilde{\varphi}_0^{rcp}$ vanishes below but close to $x_s = 1$. The right panel in Fig. 7.3 presents the obtained results for $(\varphi^{rcp} - \tilde{\varphi}_0^{rcp})/\tilde{\varphi}_0^{rcp}$ which show a striking similarity to $(\varphi^c - \varphi_0^c)/\varphi_0^c$ shown on the left panel in Fig. 7.3. The change from the minimum-shape to an S-shape and a maximum-shape upon decreasing δ_R is clearly reproduced by the random close packing results which strongly supports the quality of MCT in 2D.

Let us also briefly discuss further quantities characterizing the liquid-glass transitions of the binary hard disk model in 2D shown in Fig. 7.3. The left panel in Fig. 7.4 shows the corresponding exponent parameters λ^c. We observe the same generic trend as has been reported before by Götze and Voigtmann [25] for binary hard spheres in 3D: mixing leads to an increase in λ^c for all δ_R. For $\delta_R = 0.3$, λ^c develops a narrow but smooth maximum at $x_s \cong 0.845$ with $\lambda^c \cong 0.869$. This is a hint that there could be a higher-order singularity of type A_l, $l \geq 3$, in the surrounding of the control parameter triplet $\delta_R = 0.3$, $x_s = 0.845$, $\varphi = \varphi^c \cong 0.709$.

The right panel in Fig. 7.4 displays critical localization length Δr_α^c for the binary hard disk model in 2D at $\delta_R = 0.3$. The results for $\delta_R > 0.3$ are qualitatively similar (not shown in the figures). For both big and small particles, Δr_α^c shows a smooth and monotonic decrease upon increasing x_s. It is obvious that $\Delta r_b^c < \Delta r_s^c$ must hold for all x_s. Since we have chosen $2R_b$ as unit length, it is also obvious that $\Delta r_s^c(x_s = 1) = \delta_R \Delta r_b^c(x_s = 0)$. The lines in Fig. 7.4 interpolate smoothly and monotonically between these limits.

For binary hard spheres in 3D, multiple glassy states occur below $\delta_R \cong 0.4$ [50] where the liquid-glass transition line subdivides into two distinguishable parts. The unique point in the physical control parameter space where this first appears is an A_4-singularity with $\lambda^c = 1$. Below this value for δ_R, the critical localization length Δr_α^c as a function of x_s displays a jump indicating the transition from one glassy state into the other one. At the same point the liquid-glass transition line exhibits a kink. Now, from the smooth behavior of the glass transition line and the critical localization length at $\delta_R = 0.3$ in Figs. 7.3 and 7.4 close to the maximum value of λ^c we conclude that if multiple glassy states also exist for the binary hard disk model in 2D, then these will only occur for $0 < \delta_R < 0.3$. To investigate such small δ_R we would need larger k-grids to avoid disturbing discretization effects. Due to the much higher numerical effort for MCT calculations in 2D compared to 3D we leave it as an open challenge to investigate the occurrence of multiple glassy states for binary hard disks in 2D.

7.2.2 Mixing scenarios

In this section we demonstrate that the mixing scenarios presented by Götze and Voigtmann [25] for binary hard spheres in 3D can also be observed for binary hard disks in 2D. In order to follow their convention, we have decided to choose in this section φ, δ_R, and the packing contribution of the smaller particles $\hat{x}_s = \varphi_s/\varphi$ as independent control

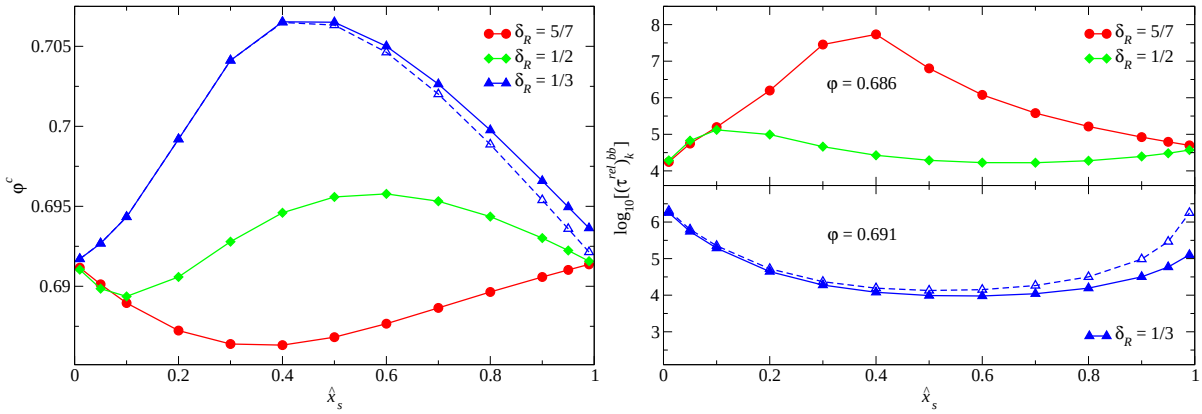

Figure 7.5: Left panel: Glass transition lines for the binary hard disk model in 2D, plotted as functions of the packing contribution of the smaller particles $\hat{x}_s = \varphi_s/\varphi$. Right panels: α-relaxation times defined by $\Phi_k^{bb}((\boldsymbol{\tau}^{rel})_k^{bb}) = 0.1(\boldsymbol{F}^c)_k^{bb}$ for the correlators of the big particles at $k = 5.1909$ for fixed δ_R and φ close below the corresponding glass transition lines for the binary hard disk model in 2D. In both panels, the open triangles calculated with $K = 400$ grid points (instead of $K = 250$) give an estimate for the error due to the high wave number cutoff.

parameters. It is related to x_s via

$$x_s = \frac{\hat{x}_s/\delta_R^d}{1 + \hat{x}_s(1/\delta_R^d - 1)}. \tag{7.3}$$

The left panel in Fig. 7.5 shows glass transition lines for the binary hard disk model in 2D, plotted as functions of $\hat{x}_s$ for three representative values for δ_R. The line for $\delta_R = 5/7$ shows a single, clearly pronounced minimum, the line for $\delta_R = 1/2$ is S-shaped, and the transition line for $\delta_R = 1/3$ exhibits a single maximum.

The total variation of the glass transition lines in Fig. 7.5 is quite small, it is of the order of 1%. Nevertheless, these small changes in φ^c may have a strong influence on time-dependent quantities which are easily accessible to both experiments and computer simulations. Let us fix some δ_R and φ such that for all $0 < \hat{x}_s < 1$ it is $0 < \varphi^c(\hat{x}_s, \delta_R) - \varphi \ll 1$. Eqs. (4.35) and (4.36) predict then a strong variation in the time scales $(\boldsymbol{\tau}^{rel})_k^{\alpha\beta} \sim (\varphi^c(\hat{x}_s, \delta_R) - \varphi)^{-\gamma(\hat{x}_s, \delta_R)}$ for the α-relaxation of the correlators $\Phi_k^{\alpha\beta}(t)$. This is exemplified on the right panel in Fig. 7.5 for the α-relaxation times defined by $\Phi_k^{bb}((\boldsymbol{\tau}^{rel})_k^{bb}) = 0.1(\boldsymbol{F}^c)_k^{bb}$ for the unnormalized correlators of the big particles at $k = 5.1909$. We have chosen this wave number to be located below the principal peak in $(\boldsymbol{F}^c)_k^{bb}/(\boldsymbol{S}^c)_k^{bb}$ at $x_s = 0$ (see Fig. 7.8), similar to the choice of Götze and Voigtmann [25] for binary hard spheres in 3D. The qualitative $\hat{x}_s$-dependencies of the corresponding glass transition lines in Fig. 7.5 are clearly reflected by the $\hat{x}_s$-dependencies of the α-relaxation times. $(\boldsymbol{\tau}^{rel})_k^{bb}$ shows a single maximum for $\delta_R = 5/7$, is S-shaped for

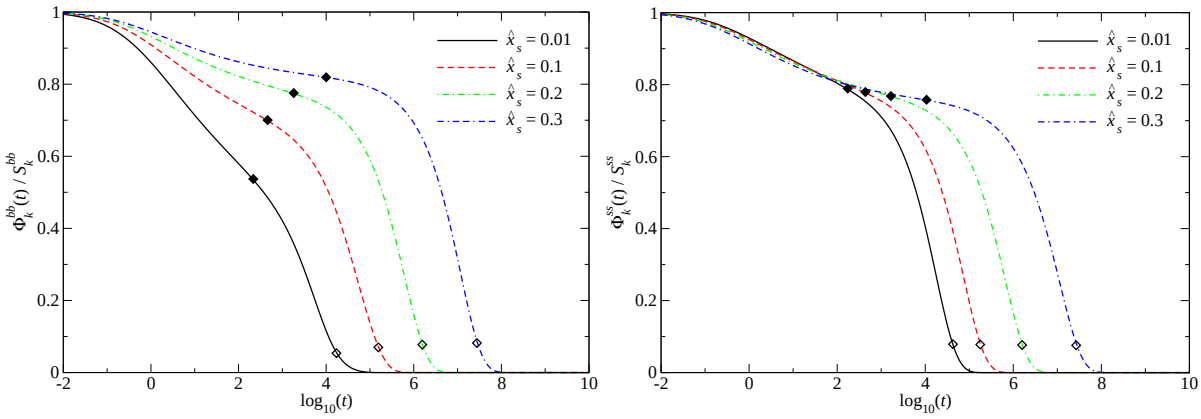

Figure 7.6: The left panel shows normalized correlators of the big particles for the binary hard disk model in 2D at $\varphi = 0.686$, $\delta_R = 5/7$, and $k = 5.1909$ for different packing contributions $\hat{x}_s = \varphi_s/\varphi$. Filled diamonds mark the crossings of the normalized critical plateau values $(\boldsymbol{F}^c)_k^{bb}/(\boldsymbol{S}^c)_k^{bb}$. Open diamonds mark the crossings of the values $0.1(\boldsymbol{F}^c)_k^{bb}/(\boldsymbol{S}^c)_k^{bb}$. The right panel shows the corresponding correlators for the small particles.

$\delta_R = 1/2$, and exhibits a single minimum for $\delta_R = 1/3$. For $\delta_R = 5/7$, $(\boldsymbol{\tau}^{rel})_k^{bb}$ varies by more than three decades.

Following Götze and Voigtmann [25], we analyze also some normalized density correlation functions $\Phi_k^{\alpha\alpha}(t)/S_k^{\alpha\alpha}$. Let us define $(\tilde{\boldsymbol{\tau}}^{rel})_k^{\alpha\alpha}$ as the characteristic time scale specified by 90% of the decay of such a correlator from its normalized plateau value $(\boldsymbol{F}^c)_k^{\alpha\alpha}/(\boldsymbol{S}^c)_k^{\alpha\alpha}$ to zero. Fig. 7.6 shows normalized correlators $\Phi_k^{\alpha\alpha}(t)/S_k^{\alpha\alpha}$ for the binary hard disk model in 2D at fixed $\varphi = 0.686$, $\delta_R = 5/7$, and $k = 5.1909$ for different packing contributions $\hat{x}_s$ of the smaller particles. For the chosen value of δ_R, the corresponding glass transition line shows a single minimum at $\hat{x}_s \cong 0.4$, see Fig. 7.5. Hence, starting from the almost monodisperse system at $\hat{x}_s = 0.01$ and increasing the packing contribution of the smaller disks to $\hat{x}_s = 0.3$ leads to a decrease of the distance $\varphi^c(\hat{x}_s, \delta_R) - \varphi$ to the critical line which is reflected by an increase in $(\tilde{\boldsymbol{\tau}}^{rel})_k^{\alpha\alpha}$ by more than three decades, see the open diamonds in Fig. 7.6.

The opposite scenario is shown in Fig. 7.7. It displays $\Phi_k^{\alpha\alpha}(t)/S_k^{\alpha\alpha}$ for the binary hard disk model in 2D at fixed $\varphi = 0.691$, $\delta_R = 1/3$, and $k = 5.1909$ for different packing contributions of the smaller disks. For the δ_R chosen here, the corresponding glass transition line exhibits a single maximum at $\hat{x}_s \cong 0.4$, see Fig. 7.5. Hence, starting at $\hat{x}_s = 0.01$ and increasing the packing contribution of the smaller disks to $\hat{x}_s = 0.3$ leads to an increase of the distance $\varphi^c(\hat{x}_s, \delta_R) - \varphi$ to the critical line, and thus $(\tilde{\boldsymbol{\tau}}^{rel})_k^{\alpha\alpha}$ decreases by about two decades as indicated by the open diamonds in Fig. 7.7.

Beside the variation in φ^c discussed above, Götze and Voigtmann [25] have reported two additional mixing effects for binary hard spheres in 3D. The first one is an increase in

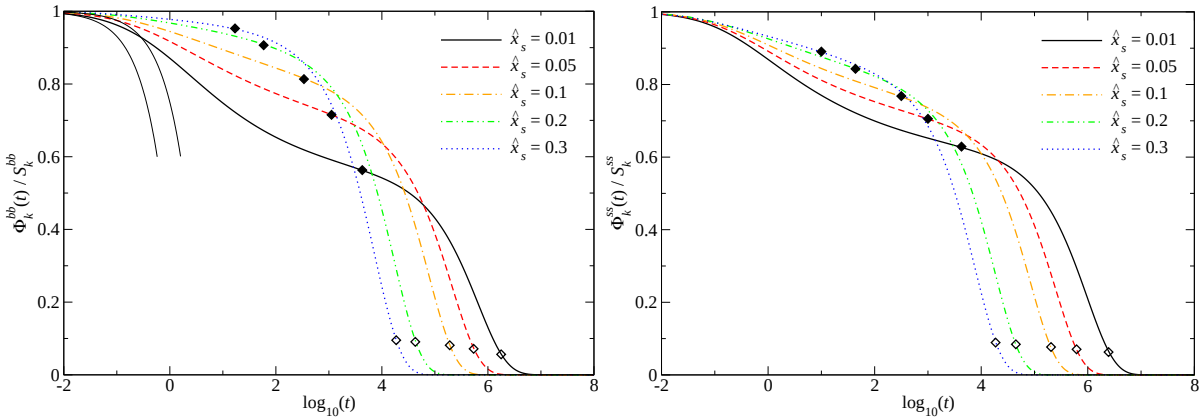

Figure 7.7: The same as Fig. 7.6 but for $\delta_R = 1/3$ and $\varphi = 0.691$. The thin lines on the left panel show the short-time asymptotes given by Eq. (4.3) for $\hat{x}_s = 0.01$ and $\hat{x}_s = 0.3$ (from left to right).

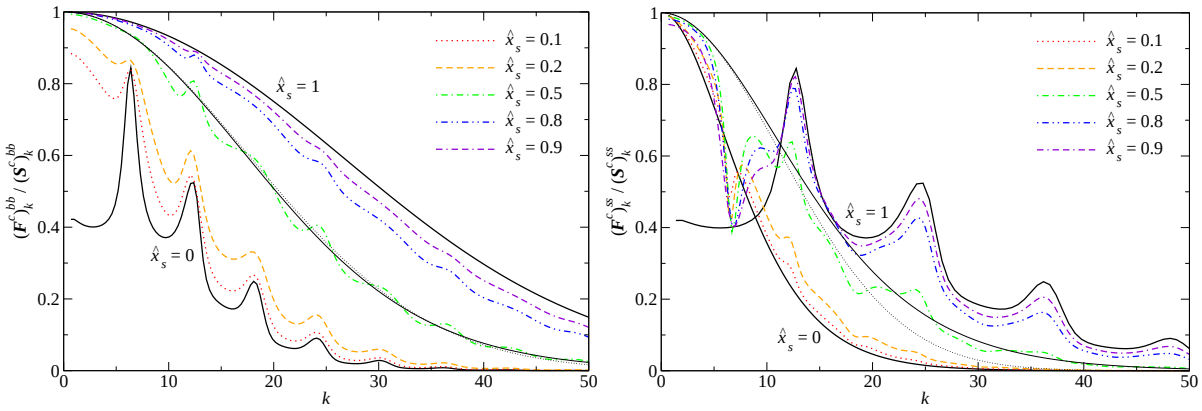

Figure 7.8: The left panel shows normalized critical NEPs for the big particles at $\delta_R = 1/2$ for the binary hard disk model in 2D. The thin line shows the self-NEPs for $\hat{x}_s = 0.5$. These can be approximated by the Gaussian function $F_{\alpha,k}^{self,c} \approx \exp(-(k\Delta r_\alpha^c)^2)$, as indicated by the thin dotted line. The right panel shows the corresponding NEPs for the small particles.

the normalized critical NEPs $(\boldsymbol{F}^c)_k^{\alpha\alpha}/(\boldsymbol{S}^c)_k^{\alpha\alpha}$ upon increasing $\hat{x}_s$ for not too small k which is related to an increase in the plateau values of the correlation functions for intermediate times. As exemplified in Fig. 7.8 for $\delta_R = 1/2$, this effect is also observable for the binary hard disk model in 2D for both the big and small particles, see also the filled diamonds in Figs. 7.6 and 7.7. The observed effect can be understood intuitively: for not too small k, the collective NEPs $(\boldsymbol{F}^c)_k^{\alpha\alpha}/(\boldsymbol{S}^c)_k^{\alpha\alpha}$ oscillate around the corresponding self-NEPs $F_{\alpha,k}^{self,c}$, as illustrated for $\hat{x}_s = 0.5$ by the thin lines in Fig. 7.8. These self-NEPs can roughly be approximated by the Gaussian function $F_{\alpha,k}^{self,c} \approx \exp(-(k\Delta r_\alpha^c)^2)$ obeying Eq. (3.11) which for $\hat{x}_s = 0.5$ is also indicated in Fig. 7.8 by the thin dotted lines. As already discussed above, the critical localization length Δr_α^c monotonically decreases upon increasing $\hat{x}_s$, see again Fig. 7.4, and thus we obtain an increase of both the collective and the self-NEPs as an overall trend.

The second remaining mixing effect is the slowing down of the relaxation towards the plateau values for the correlators of the big particles for not too large k in the sense that $\Phi_k^{bb}(t)/S_k^{bb}$ versus $\log_{10}(t)$ becomes flatter upon increasing $\hat{x}_s$ starting with $\hat{x}_s = 0$. This effect is clearly visible on the left panels in Figs. 7.6 and 7.7. In the framework of a more advanced analysis using the so-called equations of structural relaxation [25], Götze and Voigtmann have pointed out that the change in the short-time dynamics upon increasing $\hat{x}_s$ is not sufficient to explain the observed effect. Without going more into the details here, let us state that our results on the left panel in Fig. 7.7 support this statement. The shown short-time asymptotes resulting from Eq. (4.3) for $\hat{x}_s = 0.01$ and $\hat{x}_s = 0.3$ fall already at $\log_{10}(t) \cong -1$ significantly below the corresponding correlators. Thus, the enormous flattening of the curves in the region $0 < \log_{10}(t) < 2$ can not be simply explained by the slowing down of the diffusion at short times, but we can explain the observed effect along the lines of Götze and Voigtmann: for fixed $\hat{x}_s$ and fixed δ_R the relaxation of $\Phi_k^{bb}(t)/S_k^{bb}$ towards its plateau value can be described to leading order in $\sigma \propto \varepsilon = (\varphi - \varphi^c)/\varphi^c$ by that of the expression $[(\boldsymbol{F}^c)_k^{bb} + (\boldsymbol{H}^c)_k^{bb}\mathcal{G}(t)]/(\boldsymbol{S}^c)_k^{bb}$ with the β-correlator $\mathcal{G}(t)$ obeying Eqs. (4.29) and (4.30). Now, upon increasing $\hat{x}_s = 0.01$ to $\hat{x}_s = 0.3$ following the values in Figs. 7.6 and 7.7 we observe for both $\delta_R = 5/7$ and $\delta_R = 1/3$ a monotonic decrease in the critical exponent a, a monotonic decrease in the time constant t_0, and a monotonic decrease in the critical amplitudes $(\boldsymbol{H}^c)_k^{bb}/(\boldsymbol{S}^c)_k^{bb}$ for $0 < k < 6.1$ (not shown in the figures). These three effects all contribute to the flattening of the $\Phi_k^{bb}(t)/S_k^{bb}$ versus $\log_{10}(t)$ curves for times within the first scaling-law regime.

Let us conclude at this point that we have found the same four mixing effects for binary hard disks in 2D as have been reported for binary hard spheres in 3D by Götze

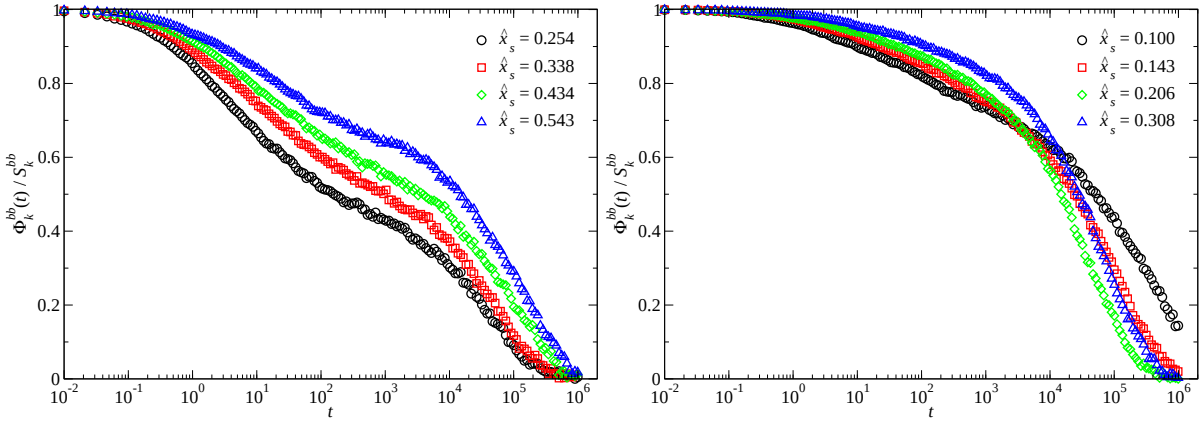

Figure 7.9: The left panel shows Brownian dynamics simulation results of Weysser [51] for the normalized collective density correlators of binary hard disk mixtures in 2D at $\delta_R = 5/7$, $\varphi = 0.79$, and $k = 8.5$. The single-particle short-time diffusion constants and the unit of time in the simulation were chosen such that $D_b^0 = D_s^0 = 0.005$, for simplicity. The right panel shows corresponding results for the same model at $\delta_R = 1/3$, $\varphi = 0.81$, and $k = 9.0$.

and Voigtmann [25]. The complex mixing scenario on the left panel in Fig. 7.7 is the result of an interplay of three of these mixing effects. Increasing $\hat{x}_s$ leads first to both an increase in the plateau values of the correlators at intermediate times and a slowing down of the decay toward these plateaus. However, increasing $\hat{x}_s$ also leads to a strong decrease in the α-relaxation times, and thus to a pair-wise crossing of the correlators.

Above, we have found for the binary hard disk model in 2D a striking similarity of the MCT glass transition lines to the corresponding random close packing lines, see Fig. 7.3. At this point, we ask ourselves whether our MCT predictions for the mixing effects on the time-dependent density correlators can also be tested by some independent approach, at least on a qualitative level. The answer is yes. The left panel in Fig. 7.9 shows normalized collective density correlators $\Phi_k^{bb}(t)/S_k^{bb}$ for the big particles of binary hard disk mixtures in 2D at $\delta_R = 5/7$, $\varphi = 0.79$, and $k = 8.5$ for different packing contributions $\hat{x}_s$ of the smaller disks calculated by Weysser [51] via Brownian dynamics simulations. Qualitatively, these data exhibit the same three mixing effects as the ones shown on the left panel in Fig. 7.6, namely an increase in the plateau values accompanied by a slowing down of the relaxation towards these plateaus and an additional slowing down of the α-relaxation process upon increasing $\hat{x}_s$. On the quantitative level, however, there are some deviations: from Fig. 7.5 we would expect that the slowest α-relaxation process occurs at $\hat{x}_s \cong 0.4$. The simulation data, however, exhibit the slowest α-relaxation at the highest investigated value $\hat{x}_s = 0.543$. Furthermore, for $\delta_R = 5/7$, MCT predicts $0.686 < \varphi^c < 0.692$ for all $\hat{x}_s$. The simulation data, however, imply $\varphi_{sim}^c \gtrsim 0.79$ which means that MCT underestimates the critical

packing fraction by about 15%.

The right panel in Fig. 7.9 shows Brownian dynamics simulation results of Weysser [51] for $\Phi_k^{bb}(t)/S_k^{bb}$ for binary hard disk mixtures in 2D at $\delta_R = 1/3$, $\varphi = 0.81$, and $k = 9.0$ for different packing contributions $\hat{x}_s$ of the smaller disks. On a qualitative level, the data for the three lowest values for $\hat{x}_s$ are fully consistent with all our MCT results in both Fig. 7.5 and the left panel in Fig. 7.7. Upon increasing $\hat{x}_s$, the simulation data exhibit an increase in the plateau values accompanied by a slowing down of the relaxation towards these plateaus. Furthermore, increasing $\hat{x}_s$ from 0.100 to 0.206 leads to a speeding up of the α-relaxation. Thus, the three correlators corresponding to the lowest values for $\hat{x}_s$ exhibit a pair-wise crossing. A further increase in $\hat{x}_s$ to 0.308 leads again to a slowing down of the α-relaxation process, although from the MCT results in Fig. 7.5 we would expect the fastest α-relaxation at $\hat{x}_s \cong 0.5$. The fact that the simulation data at $\delta_R = 5/7$ and $\varphi = 0.79$ and the ones at $\delta_R = 1/3$ and $\varphi = 0.81$ show very similar α-relaxation times is also consistent with the MCT result $\varphi^c(\hat{x}_s, \delta_R = 5/7) < \varphi^c(\hat{x}_s, \delta_R = 1/3)$ for $0 < \hat{x}_s < 1$.

Let us conclude here with the statement that, at least on a qualitative level, the four mixing effects predicted by MCT for the binary hard disk model in 2D are also observable in computer simulations which again supports the quality of MCT. At the time of writing of this thesis, a more detailed study concerning this topic was still work in progress [52].

7.2.3 Asymptotic scaling laws

For monodisperse hard spheres in 3D, Franosch et al. [24] have analyzed in detail the range of validity of the asymptotic scaling laws summarized in Sect. 4.6. Furthermore, they have also analyzed the leading-order corrections to these scaling laws. A similar analysis was carried out by Bayer et al. [18] for monodisperse hard disks in 2D with very similar results both qualitatively and quantitatively. Götze and Voigtmann [25] have also investigated the asymptotic laws for binary mixtures of hard spheres in 3D. Besides the trend that, compared to the monodisperse case, the exponent parameter λ^c for a mixture is always larger (see also Fig. 7.4) and the fact that the range of validity for the asymptotic laws depends on the chosen glass transition point, qualitatively nothing new occurred. Generically, one may state that nothing new appears on the qualitative level as long as one is sufficiently far away from higher-order singularities [2]. For the binary hard disk model in 2D, we have found similar results. Thus, in order to make this presentation not too lengthy, we restrict ourselves to a few representative examples.

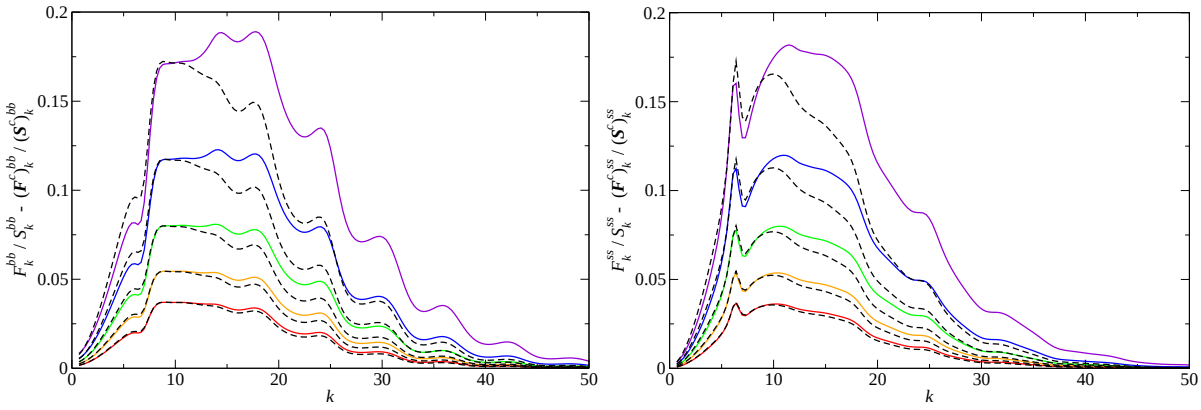

Figure 7.10: The left panel shows the increase of the normalized plateau values of the correlators of the big particles in the glassy state for the binary hard disk model in 2D at $\delta_R = 5/7$, $\hat{x}_s = 0.3$, and $\varepsilon = (\varphi - \varphi^c)/\varphi^c = 10^{-l/3}$, $l = 6, \ldots, 10$ (from up to down). The dashed lines show the leading-order $\varepsilon^{1/2}$-asymptotes $[(\boldsymbol{H}^c)_k^{bb}/(\boldsymbol{S}^c)_k^{bb}]\sqrt{\sigma/(1-\lambda^c)}$. $\sigma \cong 1.966\varepsilon$ can be obtained via numerical differentiation of Eq. (4.21) and $\lambda^c \cong 0.717$ follows from Eq. (4.22). The right panel shows the corresponding results for the small particles.

For the following, we consider the binary hard disk model in 2D. We fix $\delta_R = 5/7$ and $\hat{x}_s = 0.3$. For the corresponding critical point φ^c we further introduce the so-called distance parameter

$$\varepsilon = (\varphi - \varphi^c)/\varphi^c. \tag{7.4}$$

Fig. 7.10 shows the increase $F_k^{\alpha\alpha}/S_k^{\alpha\alpha} - (\boldsymbol{F}^c)_k^{\alpha\alpha}/(\boldsymbol{S}^c)_k^{\alpha\alpha}$ of the normalized NEPs in the glassy regime for $\varepsilon = 10^{-l/3}$, $l = 6, \ldots, 10$. The leading-order $\varepsilon^{1/2}$-asymptotes following from Eq. (4.23) are also included as dashed lines. For $k \leq 13.3$, the leading-order asymptotes describe the data for both the big and the small particles on a relative error level below 10% if $l \geq 8$, i.e. $\varepsilon \leq 0.002$. For larger k or ε, the deviations become larger.

Now, let us demonstrate the validity of the factorization theorem given by Eq. (4.28). The left panel in Fig. 7.11 shows the functions $\{\Phi_k^{bb}(t) - (\boldsymbol{F}^c)_k^{bb}\}/(\boldsymbol{H}^c)_k^{bb}$ for the big particles at $\varepsilon \pm 10^{-4}$ for three values of k. Also included are the corresponding numerical solutions for the β-correlator $\mathcal{G}(t)$. The data for $\{\Phi_k^{bb}(t) - (\boldsymbol{F}^c)_k^{bb}\}/(\boldsymbol{H}^c)_k^{bb}$ for the liquid case ($\varepsilon < 0$) deviate less than 10% from $\mathcal{G}(t)$ within the time interval $2.2 < \log_{10}(t) < 7.3$. For the glass ($\varepsilon > 0$), the data for $\{\Phi_k^{bb}(t) - (\boldsymbol{F}^c)_k^{bb}\}/(\boldsymbol{H}^c)_k^{bb}$ deviate less than 10% from $\mathcal{G}(t)$ for $\log_{10}(t) > 2.3$.

Let us finally consider density correlators $\boldsymbol{\Phi}(t)$ in the liquid regime for $\varepsilon = -10^{-l/3}$, $l = 9, ..., 15$, and $\alpha = b$ with $k = 9.9909$, and also for $\alpha = s$ with $k = 5.1909$. The validity of the α-scaling law given by Eqs. (4.35) and (4.36) can be demonstrated as follows [53]: rather than calculating the ε-independent constant prefactor on the r.h.s. of Eq. (4.35), we take the long-time part of the correlator for $l = 15$ as the best available numerical

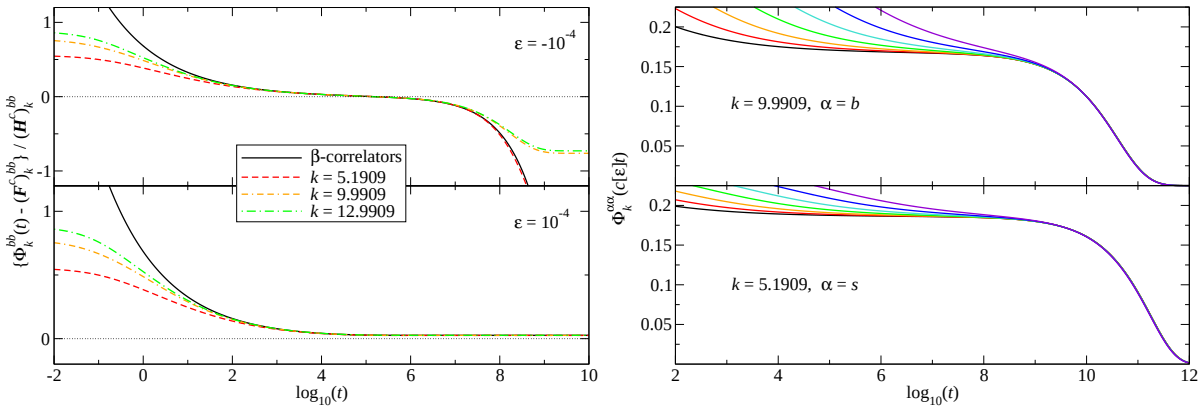

Figure 7.11: Left panels: The plots demonstrate the validity of the factorization theorem for the binary hard disk model in 2D at $\delta_R = 5/7$ and $\hat{x}_s = 0.3$ for both a liquid, $\varepsilon = (\varphi - \varphi^c)/\varphi^c < 0$ and a glassy state ($\varepsilon > 0$). The time constant $t_0 \cong 0.304$ needed for the unique determination of the β-correlator $\mathcal{G}(t)$ was read off from the plateau value of $t^a\{(\mathbf{\Phi}^c)_k^{bb}(t) - (\boldsymbol{F}^c)_k^{bb}\}/(\boldsymbol{H}^c)_k^{bb}$ at $k = 9.9909$. Right panels: The plots demonstrate the validity of the α-scaling law for the binary hard disk model in 2D at $\delta_R = 5/7$, $\hat{x}_s = 0.3$, and $\varepsilon = -10^{-l/3}$, $l = 9, ..., 15$ (from right to left). The scaling factors are chosen to be $c[\varepsilon] = (10^5|\varepsilon|)^\gamma$. The numerical value of the exponent $\gamma = (a+b)/(2ab) \cong 2.380$ follows directly from $\lambda^c \cong 0.717$. With this, the correlators collapse onto the corresponding curves with $l = 15$ for long times without the use of any fit parameters.

approximation for the α-master function and consider rescaled correlators $\mathbf{\Phi}(c[\varepsilon]t)$ with scaling factors $c[\varepsilon] = (10^5|\varepsilon|)^\gamma$. With this choice it is easy to verify that at long times all rescaled correlators for $l > 15$ collapse onto the one for $l = 15$. This is demonstrated for $\Phi_k^{\alpha\alpha}(t)$ on the right panel in Fig. 7.11. Within the time interval $7.5 < \log_{10}(t) < 11.1$ all data for $l > 15$ deviate less than 10% from the ones for $l = 15$ such that there holds additionally $\Phi_k^{\alpha\alpha}(c[\varepsilon]t) > 0.1(\boldsymbol{F}^c)_k^{\alpha\alpha}$.

7.3 Summary

We have analyzed the influence of composition changes on the glass transition behavior of binary hard disks in 2D and binary hard spheres in 3D in the framework of MCT. For both 2D and 3D, we have demonstrated the strong predictive power of our slope formula, Eq. (6.7), by evaluating it in the weak-mixing limits $x_\alpha \to 0$. For 3D, the numerical results for $x_s \to 0$ and $0 < \delta_R \ll 1$ are in quantitative agreement with Eq. (7.1) whose derivation was based on simple geometric arguments. The direct comparison of the models in 2D and 3D shows similar qualitative behavior. We have identified the same four mixing effects for binary hard disks in 2D as have been reported before by Götze and Voigtmann [25] for binary hard spheres in 3D. The extension of the glass regime

due to mixing for size ratios close to unity is more strongly pronounced in 2D than in 3D. For small size disparities the glass transition lines become almost symmetric with respect to the equimolar concentration $x_s = 1/2$ and are, to leading order, quadratic in the size disparity $(1 - \delta_R)$ for both 2D and 3D. The range of validity of the asymptotic scaling laws is also similar for both models. The glass transition lines we have found for binary hard disks in 2D strongly resemble the corresponding random close packing lines calculated by Okubo and Odagaki [49]. Furthermore, on a qualitative level, the four mixing effects predicted by MCT for the binary hard disk model in 2D are also observable in corresponding Brownian dynamics simulation results of Weysser [51]. These facts strongly support the quality of MCT in 2D. The simulation data of Weysser [51] also show that MCT underestimates the critical packing fraction for vitrification by about 15%, similar to the case of hard spheres in 3D [2].

Chapter 8

Binary mixtures of point dipoles in 2D

In this chapter, we present a detailed MCT study on the simplified model system introduced in Sect. 6.2, i.e. the binary point dipole model in 2D. The comparison of the obtained results to those for binary hard disk mixtures in 2D presented in the previous chapter will provide information about the influence of the type of the particle interactions on the glass transition behavior. It will also provide an answer to the question in how far the mixing effects we have found for binary hard disk mixtures in 2D have generic features. As a byproduct, we propose a simple empirical ansatz for the bridge functions in Eq. (4.45).

Let us further specify: the wave number k shall be discretized according to Eq. (4.16). For the offset we choose $\hat{o}_2 = 0.303$ since we have $d = 2$ [18]. The natural unit length is given by the inverse square-root $1/\sqrt{n}$ of the total particle number density. The choice $K = 250$ and $\Delta k = 0.2$ turns out to be sufficiently accurate to avoid larger discretization effects. If not stated explicitly otherwise, the single-particle short-time diffusion coefficients D_α^0 are assumed to obey the Stokes-Einstein law according to Eq. (5.14), and the unit of time is chosen such that $D_b^0 = 0.01$. Static structure factor input for MCT is taken from both MC simulations (see Appendix A.1) and a modified version of the hypernetted-chain (HNC) theory (see Sect. 8.2 and also Appendix A.2.2). The algorithm for the numerical calculation of time-dependent correlation functions is specified in Appendix A.4.

8.1 Previous results

Let us briefly discuss some results already known for the binary point dipole model in 2D. Assoud et al. [54] have computed the phase diagram at zero temperature. They have found 18 different stable crystal structures. We are not going to further discuss

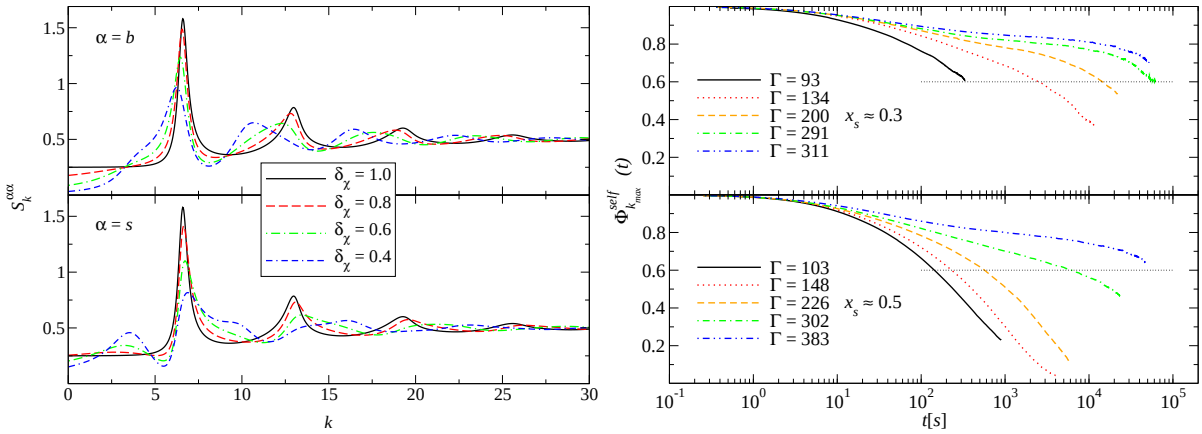

Figure 8.1: Left panels: Partial structure factors $S_k^{\alpha\alpha}$ for the big (upper left panel) and the small particles (lower left panel) for the binary point dipole model in 2D at $\Gamma = 95$ and $x_s = 0.5$ calculated by using the $T/2$-HNC closure (see Sect. 8.2). Right panels: Self-correlators of König et al. [26] for binary mixtures of dipolar particles in 2D measured experimentally at $\delta_\chi \cong 0.1$ and $x_s \cong 0.3$ (upper right panel) and $x_s \cong 0.5$ (lower right panel). The functions were averaged over big and small particles according to $\Phi_k^{self} = x_b \Phi_{b,k}^{self} + x_s \Phi_{s,k}^{self}$. k_{max} denotes the wave number corresponding to the first maximum of $g^{bb}(r)$. See Ref. [26] for details. The dotted horizontal lines mark the value 0.6 (see text).

crystallization effects in this thesis.

A further interesting phenomenon found by Hoffmann et al. [55] in the liquid regime is that the smaller particles in the binary point dipole model in 2D tend to form clusters with a sponge-like topology whereas the bigger particles remain more homogeneously distributed in space. This partial clustering seems to be a generic feature occurring for all $0 < \delta_\chi < 1$ and $0 < x_s < 1$ for not too small Γ and manifests itself by the occurrence of a prepeak in the partial structure factors S_k^{ss} of the smaller particles at low k. We are also able to reproduce this result both in the framework of MC simulations and integral equation theory with the so-called $T/2$-HNC closure (see the next section). This is exemplified on the left panel in Fig. 8.1 where we show $T/2$-HNC structure factors $S_k^{\alpha\alpha}$ for $\Gamma = 95$, $x_s = 0.5$, and $\delta_\chi = 1.0$, 0.8, 0.6, 0.4. The case $\delta_\chi = 1.0$ is a monodisperse system and by definition satisfies $S_k^{bb} = S_k^{ss}$. By decreasing δ_χ we can clearly observe a growing prepeak in S_k^{ss} at $2 < k < 5$.

Now, let us consider results for systems close to dynamical arrest. The right panel in Fig. 8.1 displays averaged self-correlators $\Phi_{k_{max}}^{self} = x_b \Phi_{b,k_{max}}^{self} + x_s \Phi_{s,k_{max}}^{self}$ for binary mixtures of dipolar particles in 2D measured experimentally by König et al. [26] at $\delta_\chi \cong 0.1$ and two different compositions $x_s \cong 0.3$ and $x_s \cong 0.5$. k_{max} denotes the wave number corresponding to the first maximum of $g^{bb}(r)$. These data clearly exhibit the stretched relaxation patterns of glass-forming liquids. We also observe that the correlators for $x_s \cong$

0.5 behave more liquid-like than the ones for $x_s \cong 0.3$. For the mixture with $x_s \cong 0.3$ the correlators for $\Gamma \geq 200$ already show clearly pronounced plateaus, while for the mixture with $x_s \cong 0.5$ the occurrence of plateaus becomes only visible for $\Gamma \geq 302$. Let us state these facts more quantitatively. The structural relaxation time $\tau_{exp}(\Gamma, x_s, \delta_\chi)$ shall be defined by $\Phi^{self}_{k_{max}}(\tau_{exp}, \Gamma, x_s, \delta_\chi) = 0.6$. It is $\tau_{exp}(\Gamma = 226, x_s \cong 0.5, \delta_\chi \cong 0.1) = 569s \ll \tau_{exp}(\Gamma = 200, x_s \cong 0.3, \delta_\chi \cong 0.1) = 14513s$. By assuming the validity of the α-scaling law given by Eqs. (4.35) and (4.36) we obtain $\tau_{exp}(\Gamma, x_s, \delta_\chi) \sim [\Gamma^c_{exp}(x_s, \delta_\chi) - \Gamma]^{-\gamma(x_s, \delta_\chi)}$ which can be read as the definition of the experimental value $\Gamma^c_{exp}(x_s, \delta_\chi)$ for the critical interaction parameter for vitrification. Assuming that for fixed $\delta_\chi \cong 0.1$ the exponent and the proportionality factor of this power law do not change sensitively under a change of $x_s \cong 0.3$ to $x_s \cong 0.5$, we obtain

$$\Gamma^c_{exp}(x_s \cong 0.3, \delta_\chi \cong 0.1) < \Gamma^c_{exp}(x_s \cong 0.5, \delta_\chi \cong 0.1). \tag{8.1}$$

We will demonstrate that MCT is able to reproduce this result.

8.2 Static structure

For the binary mixtures of hard spherical particles in 2D and 3D studied in the last chapter, we have used the well-established PY theory to calculate the static structure factor input for MCT without further commenting it. For dipolar particles in 2D, it turns out to be more challenging to calculate static structure factors with reasonable quality.

We first focus on the quality of the model system itself. The derivation of the pair-potentials given by Eq. (6.4) is based on two approximations: the negligence of both hard-core repulsions and mutual polarization effects. Thus, let us first test the validity of these approximations. The left panel in Fig. 8.2 shows partial structure factors $S^{\alpha\beta}_k$ for a binary mixture of dipolar particles in 2D at $\Gamma = 110$, $\delta_\chi \cong 0.1$, and $x_s = 0.48$ measured experimentally by Ebert [41]. The value for δ_χ is approximative due to the finite polydispersity of both species of colloidal particles. Also included are corresponding MC results for the binary point dipole model in 2D which we have obtained as described in Appendix A.1 but by using only $N = 600$ particles instead of $N = 1600$ and without data smoothing. Thus, for low k the MC structure factors are superimposed by oscillations stemming from an interplay of uncertainties of $h^{\alpha\beta}(r)$ at large r and the real space cutoff for its Fourier transform. Besides these technical artifacts, our MC results are in very good agreement with the experimental data without

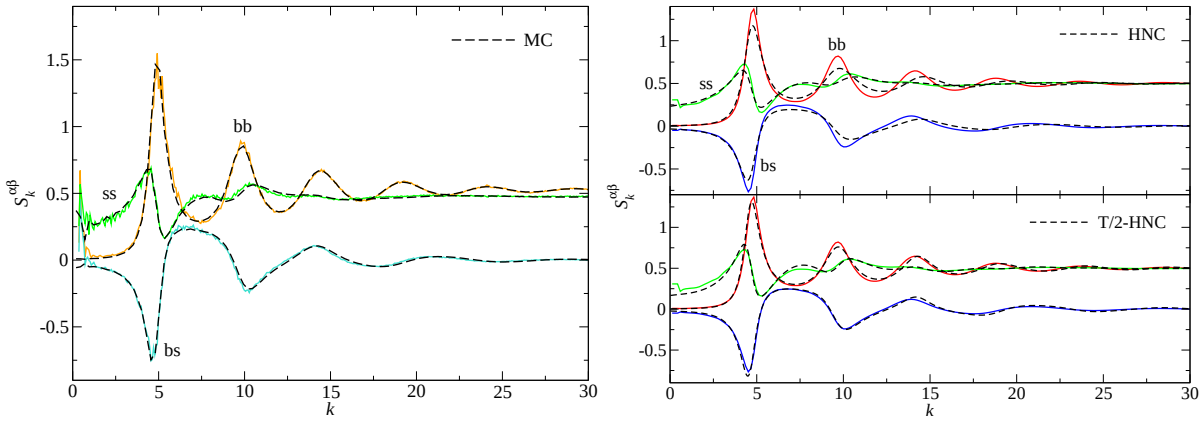

Figure 8.2: Left panel: Partial structure factors for a binary mixture of dipolar particles in 2D at $\Gamma = 110$, $\delta_\chi \cong 0.1$, and $x_s = 0.48$ measured experimentally by Ebert [41] (solid lines) and the corresponding MC results for the binary point dipole model in 2D (dashed lines) obtained with 600 particles without data smoothing. Right panels: Partial structure factors for the binary point dipole model in 2D at $\Gamma = 120$, $\delta_\chi = 0.1$, and $x_s = 0.5$ from MC simulation with 1600 particles with data smoothing (solid lines) and for HNC (dashed lines in upper right panel) and $T/2$-HNC (dashed lines in lower right panel).

the use of any adjustable parameters. With $N = 600$ particles, we were similarly able to reproduce experimentally measured partial structure factors within the parameter range $\delta_\chi \cong 0.1$, $0.29 \leq x_s \leq 0.48$, and $51 \leq \Gamma \leq 281$ (not shown in the figures). At smaller Γ, the structure factor peaks in the experimental data become more pronounced than in our MC simulation results for binary point dipoles in 2D which may indicate that the hard-core interactions of the particles become significant in the experiment. For larger Γ, we would need larger system sizes and longer simulation runs in order to reproduce the experimental data.

We can draw two important conclusions. First, for $\Gamma > 51$ the experimental system of König et al. [26] is very well described by the binary point dipole model in 2D. Second, we can be confident that our MC simulations using this model and 1600 particles will yield sufficiently realistic results for our purposes, since the MCT glass transitions discussed in this chapter will occur within the parameter range $80 < \Gamma < 160$.

Now, let us discuss the possibility of using integral equation theory for calculating static structure factors for the binary point dipole model in 2D. We have analyzed several established choices for the bridge functions $d_0^{\alpha\beta}(r)$ in Eq. (4.45). The PY approximation seems not to be reliable for the current model system. For instance, for a binary mixture with $\delta_\chi = 0.1$, $x_s = 0.5$, and $\Gamma = 10$, i.e. deep in the liquid regime, it underestimates the position of the principal peak of S_k^{bb} by about 10% and overestimates the maximum value of this peak by almost 100%. For higher values of Γ we have not

found stable numerical solutions for the PY structure factors. Another choice is the HNC approximation $d_0^{\alpha\beta}(r) = 0$. It describes the positions of the principal peaks of the partial structure factors correctly, but strongly underestimates their amplitudes (see the upper right panel in Fig. 8.2), as already noticed before by Zahn [56] and Hoffmann [57]. There are also more sophisticated closure relations which typically include adjustable parameters. This fact makes these methods unwieldy if more than one adjustable parameter is used. For instance, the Rogers-Young (RY) closure interpolating between PY and HNC has in principle three fit parameters for a binary mixture. Furthermore, the quality of the corresponding results is also not satisfactory. Fig. 3(a) in the work of Hoffmann at al. [55] clearly shows for the binary point dipole model in 2D that the RY closure relation underestimates the position of the principal peak of the partial structure factors of the big dipoles and in addition underestimates the amplitude of the oscillations beyond this peak.

For the binary point dipole model in 2D, we have found empirically that using HNC with temperature $T/2$ instead of T leads to a systematic improvement in the description of experimental and simulated data for $\boldsymbol{S}$ (see the lower right panel in Fig. 8.2). A similar observation was made before independently by Zahn [56]. Even more surprisingly, Klapp [58] has observed that also computer simulation results for specific dipolar systems in 3D can be well fitted by using HNC with $T/2$. Let us summarize alls these findings by proposing a simple empirical ansatz for the bridge functions:

$$d_0^{\alpha\beta}(r) = -\frac{u^{\alpha\beta}(r)}{k_B T}. \tag{8.2}$$

Since Eq. (8.2) has no adjustable parameters, it is well-suited for fast and systematic calculations. Eq. (8.2) will be called the $T/2$-HNC closure. For technical details, see Appendix A.2.2.

The right panel in Fig. 8.2 shows MC simulated partial structure factors for the binary point dipole model in 2D at $\Gamma = 120$, $\delta_\chi = 0.1$, and $x_s = 0.5$ compared to corresponding HNC and $T/2$-HNC results. While the HNC closure underestimates the amplitude of the oscillations of the partial structure factors, the $T/2$-HNC results are in a surprisingly good agreement with the MC data. Furthermore, we have found for all investigated examples within the control parameter range $0.1 \leq \delta_\chi \leq 0.6$, $0.1 \leq x_s \leq 0.9$, and $20 \leq \Gamma \leq 160$ that, compared to the standard HNC closure, the $T/2$-HNC closure leads to a similar improvement in the description of MC data as shown in Fig. 8.2. In the next section, this trend will also be strongly supported by the fact that using MC and $T/2$-HNC structure factors as input for MCT will lead to compatible glass transition

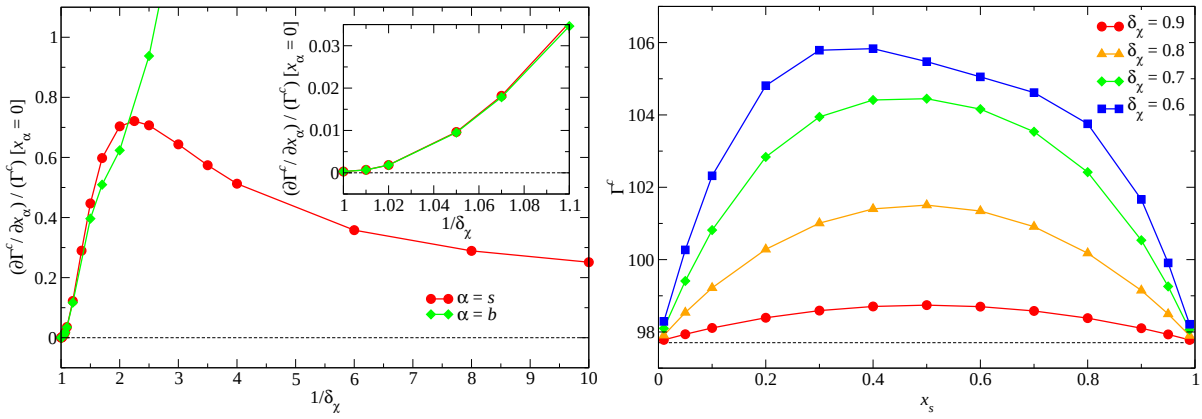

Figure 8.3: Left panel: Normalized slopes of the glass transition lines for the binary point dipole model in 2D at $x_s = 0$ and $x_b = 0$ calculated by using Eq. (6.7) and the $T/2$-HNC closure. It is $\Gamma_0^c \cong 97.704$ for the monodisperse limit. The inset presents the slopes on a much finer scale very close to $\delta_\chi = 1$. Right panel: Glass transition lines for the binary point dipole model in 2D with moderate susceptibility ratios δ_χ calculated by using the $T/2$-HNC closure. Γ_0^c is indicated by the dashed line.

scenarios on very similar temperature scales.

In the next section, we will use both MC and $T/2$-HNC for calculating the static structure factor input for MCT. This should assure that the MCT predictions we make for the binary point dipole model in 2D are not just artifacts of one of the specific techniques for the calculation of the static structure factor input.

8.3 Mode-coupling results

In the following, we present our numerical MCT results for binary point dipoles in 2D.

8.3.1 Glass transition lines

Let us start by demonstrating the predictive power of our slope formula, Eq. (6.7), for the binary point dipole model in 2D by applying it to the weak-mixing limits $x_\alpha \to 0$. The technical procedure for this is described in Appendix B.

The left panel in Fig. 8.3 shows normalized slopes $(\partial\Gamma^c/\partial x_\alpha)(\Gamma^c)^{-1}$ of the glass transition lines for the binary point dipole model in 2D at $x_\alpha = 0$, $\alpha = s, b$, as functions of $1/\delta_\chi$ calculated by using Eq. (6.7) and the $T/2$-HNC closure given by Eq. (8.2). By definition, the case $\delta_\chi = 1$ represents a one-component system with critical packing fraction $\Gamma^c(x_s, \delta_\chi = 1) \equiv \Gamma_0^c$, and thus the slopes have to be zero at this point. Our numerical results are consistent with this statement, see also the inset in Fig. 8.3. In

contrast to our results for hard spherical particles in the last chapter, the slopes for the binary point dipole model in 2D are always positive. This implies the following: compared to a corresponding one-component liquid, the presence of a small concentration of a second kind of point dipoles always increases the critical interaction parameter $\Gamma^c(x_s, \delta_\chi)$. This means that for fixed temperature T and fixed total particle density n the presence of a small concentration of a second kind of point dipoles enhances the critical value $m^c(x_s, \delta_\chi)$ of the average magnetization per particle at which the system vitrifies. In this sense, mixing always stabilizes the liquid state, i.e. MCT predicts always a plasticization effect in the weak-mixing limits.

Let us discuss the slopes in more detail. The slope curve for $x_s = 0$ starts from zero at $\delta_\chi = 1$ and first increases upon decreasing δ_χ. It exhibits a maximum at $\delta_\chi^+ \cong 0.444$ and monotonically decays upon further decreasing δ_χ. The slope curve for $x_b = 0$ starts from zero at $\delta_\chi = 1$ and strongly increases upon decreasing δ_χ. The inset in Fig. 8.3 demonstrates that the slope curves for $x_s = 0$ and $x_b = 0$ become identical for $0 < (1 - \delta_\chi) \ll 1$. This is a hint on the validity of Eq. (6.17), i.e. on the symmetry of the glass transition lines with respect to $x_s = 1/2$ for $0 < (1 - \delta_\chi) \ll 1$. As shown in Sect. 6.3, this symmetry would imply that the linear contribution in the Taylor series of $\Gamma^c(x_s, \delta_\chi)$ with respect to $0 < (1 - \delta_\chi) \ll 1$ vanishes. Indeed, the inset in Fig. 8.3 clearly demonstrates for the slope curves $s_\alpha^c(\delta_\chi) = (\partial\Gamma^c/\partial x_\alpha)(x_\alpha = 0, \delta_\chi)$ that there holds $(\partial s_\alpha^c/\partial\delta_\chi)(\delta_\chi = 1) = 0$.

The results for the slopes discussed above allow us to predict qualitative properties of the glass transition lines. Both $x_s = 0$ and $x_s = 1$ define one-component models with the same critical interaction parameter Γ_0^c. Hence, all glass transition lines must exhibit at least one maximum. Furthermore, for $0 < \delta_\chi < \delta_\chi^+$ the slope curve $s_s^c(\delta_\chi)$ ($s_b^c(\delta_\chi)$) decreases (increases) upon decreasing δ_χ. Hence, for two susceptibility ratios δ_χ^1 and δ_χ^2 with $0 < \delta_\chi^1 < \delta_\chi^2 < \delta_\chi^+$, the two corresponding glass transition lines must have an odd number of intersection points and thus at least one crossing. If, however, there holds $\delta_\chi^+ < \delta_\chi^1 < \delta_\chi^2 < 1$, then the number of intersection points is even, since for $\delta_\chi^+ < \delta_\chi < 1$ both $s_s^c(\delta_\chi)$ and $s_b^c(\delta_\chi)$ increase upon decreasing δ_χ. Furthermore, we expect that the glass transition lines become symmetric with respect to the equimolar composition $x_s = 1/2$ in the limit of small disparity in the susceptibilities which implies that the linear contribution in the Taylor series of $\Gamma^c(x_s, \delta_\chi)$ with respect to $0 < (1 - \delta_\chi) \ll 1$ vanishes.

In the following, we present glass transition lines calculated both by using $T/2$-HNC and MC structure factors as input for MCT. Due to crystallization effects, the control parameters for the MC data had to be restricted to $0.1 \leq x_s \leq 0.9$ and $0 < \delta_\chi \leq 0.6$.

The right panel in Fig. 8.3 shows glass transition lines for the binary point dipole

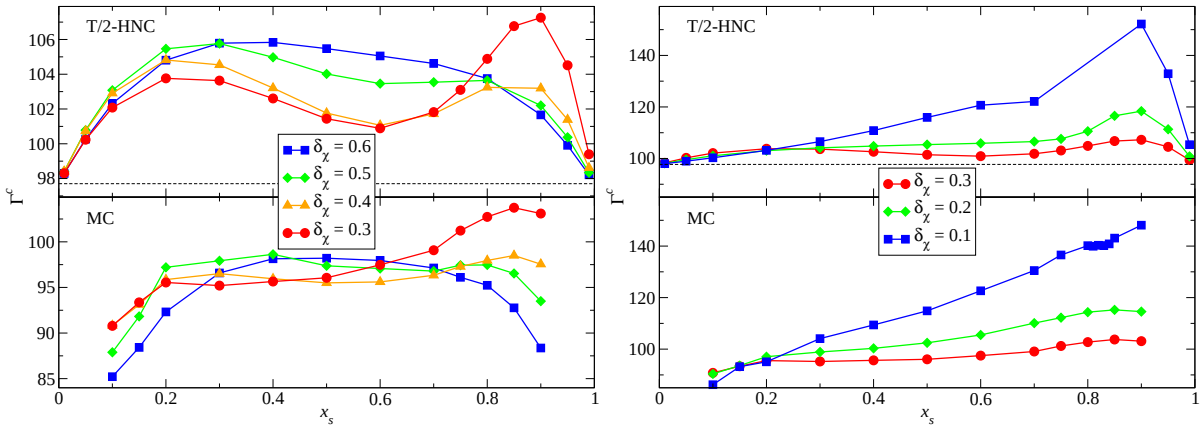

Figure 8.4: Left panels: Glass transition lines for the binary point dipole model in 2D calculated by using $T/2$-HNC structure factors (upper left panel) and MC structure factors (lower left panel). The dashed line in the upper left panel indicates the $T/2$-HNC value for Γ_0^c. Right panels: Glass transition lines for the binary point dipole model in 2D with larger disparities in the susceptibilities calculated by using $T/2$-HNC structure factors (upper right panel) and MC structure factors (lower right panel). The dashed line in the upper right panel indicates the $T/2$-HNC value for Γ_0^c. In the neighborhood of $x_s = 0.8$ and $\delta_\chi = 0.1$ we had problems in finding stable numerical solutions for the $T/2$-HNC structure factors, and thus there are no data points for Γ^c in this region in the upper right panel.

model in 2D for moderate susceptibility ratios $\delta_\chi^+ < 0.6 \leq \delta_\chi \leq 0.9$ calculated by using $T/2$-HNC structure factors as input for MCT. For $0 < x_s < 1$, all lines are strictly above the monodisperse value Γ_0^c and exhibit a single maximum. In addition, the glass transition lines do not intersect. The three lines for $0.7 \leq \delta_\chi \leq 0.9$ are almost symmetric with respect to the equimolar composition $x_s = 1/2$. Furthermore, a numerical test for $x_s = 1/4$ has confirmed a quadratic dependence on $0 < (1 - \delta_\chi) \ll 1$ (not shown in the figures). All these properties are compatible with the results for the slopes shown on the left panel in Fig. 8.3.

The left panel in Fig. 8.4 presents glass transition lines for the binary point dipole model in 2D for $0.3 \leq \delta_\chi \leq 0.6$ calculated both by using $T/2$-HNC and MC structure factors as input for MCT. The $T/2$-HNC curves again are strictly above the monodisperse value Γ_0^c for $0 < x_s < 1$. We can not verify this statement for the MC curves, since in this case we have no reasonable estimate for Γ_0^c due to crystallization effects. Let us first focus on the $T/2$-HNC results. The glass transition line for $\delta_\chi = 0.6$ exhibits only a single rather flat maximum. The other ones with $0.3 \leq \delta_\chi \leq 0.5$ develop two local maxima with a local minimum at $x_s \cong 0.6$ in between. For the pair $\delta_\chi^1 = 0.5$ and $\delta_\chi^2 = 0.6$ it is $\delta_\chi^+ < \delta_\chi^1 < \delta_\chi^2 < 1$ and thus the results for the slopes in Fig. 8.3 predict an even number of intersection points for the corresponding two glass transition lines. Indeed, these lines intersect twice. For the pair $\delta_\chi^1 = 0.3$ and $\delta_\chi^2 = 0.4$ it is $0 < \delta_\chi^1 < \delta_\chi^2 < \delta_\chi^+$

and the corresponding two glass transition lines have a single intersection point which is also consistent with the results for the slopes in Fig. 8.3. Now, let us consider the MC results on the left panel in Fig. 8.4. The data are numerically less precise and the occurring extrema in the curves are not as clearly pronounced as for the $T/2$-HNC results. Furthermore, the MC curves do not for all pairs δ_χ^1 and δ_χ^2 exhibit the same number of intersection points as the corresponding $T/2$-HNC ones. Nevertheless, the MC data clearly support at least the qualitative x_s-dependencies of the glass transition lines predicted by the $T/2$-HNC closure. Note that the scales for Γ^c and its total variation are also similar for both approaches.

The right panel in Fig. 8.4 shows glass transition lines for the binary point dipole model in 2D for larger disparities in the susceptibilities, $0.1 \leq \delta_\chi \leq 0.3 < \delta_\chi^+$, calculated both by using $T/2$-HNC and MC structure factors as input for MCT. We first focus on the $T/2$-HNC data. Again, all glass transition lines are strictly above the monodisperse value Γ_0^c for $0 < x_s < 1$. The glass transition line for $\delta_\chi = 0.3$ (also shown on the left panel in Fig. 8.4 on a finer scale for Γ^c) exhibits two local maxima at $x_s \cong 0.2$ and $x_s \cong 0.9$ and in between a local minimum at $x_s \cong 0.6$. Upon decreasing δ_χ, the amplitude of the maximum at $x_s \cong 0.9$ strongly increases while the maximum at $x_s \cong 0.2$ and thus also the minimum at $x_s \cong 0.6$ become less pronounced. Consequently, the glass transition line for $\delta_\chi = 0.2$ exhibits only a single maximum at $x_s \cong 0.9$. The line for $\delta_\chi = 0.1$ seems to show a similar qualitative x_s-dependence. However, in the neighborhood of $x_s = 0.8$ and $\delta_\chi = 0.1$ we had problems in finding stable numerical solutions for the $T/2$-HNC structure factors at higher Γ, and thus we have no data points for Γ^c in this region. In agreement with the predictions from slopes presented in Fig. 8.3, each pair of the shown glass transition lines exhibits a single intersection point. The MC results on the right panel in Fig. 8.4 clearly support the trends predicted by the $T/2$-HNC closure. Note especially the similarity of the intersection points of the curves. Furthermore, both approaches yield almost identical scales for Γ^c and its total variation.

A central result we can read off from all $T/2$-HNC data in Figs. 8.3 and 8.4 is that there holds strictly

$$\Gamma^c(x_s, \delta_\chi) > \Gamma_0^c \tag{8.3}$$

for all tested $0 < \delta_\chi < 1$ and $0 < x_s < 1$. The corresponding MC results in Fig. 8.4 are also consistent with these findings. Thus we can conclude: for the binary point dipole model in 2D, MCT predicts always a stabilization of the liquid state due to mixing. Further, the amplitude of this plasticization effect is quite large. For instance, the glass transition lines for $\delta_\chi = 0.1$ on the right panel in Fig. 8.4 vary by more than 50%.

In particular, MCT predicts with both $T/2$-HNC and MC structure factors as input the inequality

$$\Gamma^c(x_s = 0.3, \delta_\chi = 0.1) < \Gamma^c(x_s = 0.5, \delta_\chi = 0.1) \tag{8.4}$$

which qualitatively reproduces the experimental result given by Eq. (8.1). This first comparison of our MCT predictions for the binary point dipole model in 2D to available experimental data indicates that at least on a qualitative level MCT may be able to describe the change in the relaxation behavior upon composition changes. The Γ values on the right panel in Fig. 8.1 also indicate that MCT tends to overestimate the temperature scale at which vitrification sets in. For $\delta_\chi = 0.1$ and $x_s = 0.3$ MCT yields $\Gamma^c \cong 105$ by both using $T/2$-HNC and MC structure factors as input. On the upper right panel in Fig. 8.1, however, the development of a plateau as a precursor of a possible glass transition only becomes clearly visible in the experimental data for $\Gamma \geq 200$. Hence, MCT overestimates the scale for the glass transition temperature by more than a factor of two, as well-known for other systems [2]. To test our MCT predictions more systematically, it would be necessary to have data from experiments or computer simulations for a much larger range of both x_s and δ_χ.

At this point, let us also speculate about the physical origin of the predicted plasticization effect for the binary point dipole model in 2D. As already discussed in Sect. 8.1, a generic mixing effect on the static structure occurring for all $0 < x_s < 1$ and $0 < \delta_\chi < 1$ is a partial clustering of the smaller dipoles which manifests itself by the occurrence of a prepeak in the partial structure factors S_k^{ss} of the smaller particles at low k. In our case, all partial structure factors S_k^{ss} with $0 < \delta_\chi < 1$ and $0 < x_s < 1$ used for calculating the glass transition lines in Figs. 8.3 and 8.4 exhibit such a prepeak. On the other hand, MCT predicts plasticization for all $0 < \delta_\chi < 1$ and $0 < x_s < 1$. Thus, it could be that the partial clustering of the smaller particles is the physical origin for the plasticization effect predicted by MCT. In order to test this conjecture, let us again consider the $T/2$-HNC structure factors $S_k^{\alpha\alpha}$ shown on the left panel in Fig. 8.1 for $\Gamma = 95$, $x_s = 0.5$, and $\delta_\chi = 1.0$, 0.8, 0.6, 0.4. The case $\delta_\chi = 1.0$ is a monodisperse system close to its MCT glass transition point which shows no clustering. Now, by decreasing δ_χ we observe five qualitative effects on $S_k^{\alpha\alpha}$: (i) a growing prepeak in S_k^{ss} at $2 < k < 5$, (ii) a decrease in S_k^{bb} for $0 < k < 3$, (iii) a decrease in the amplitude in the principal and the subsequent peaks in both S_k^{bb} and S_k^{ss}, (iv) a shrinking of the k-scale for the oscillations of S_k^{bb}, and (v) a stretching of the k-scale for the oscillations of S_k^{ss}. The plasticization effect predicted by MCT must be a result from a complicated interplay of these five competing effects. Thus, at least from our analysis here it is not obvious whether there is a connection between clustering and plasticization or not. It remains a challenge to

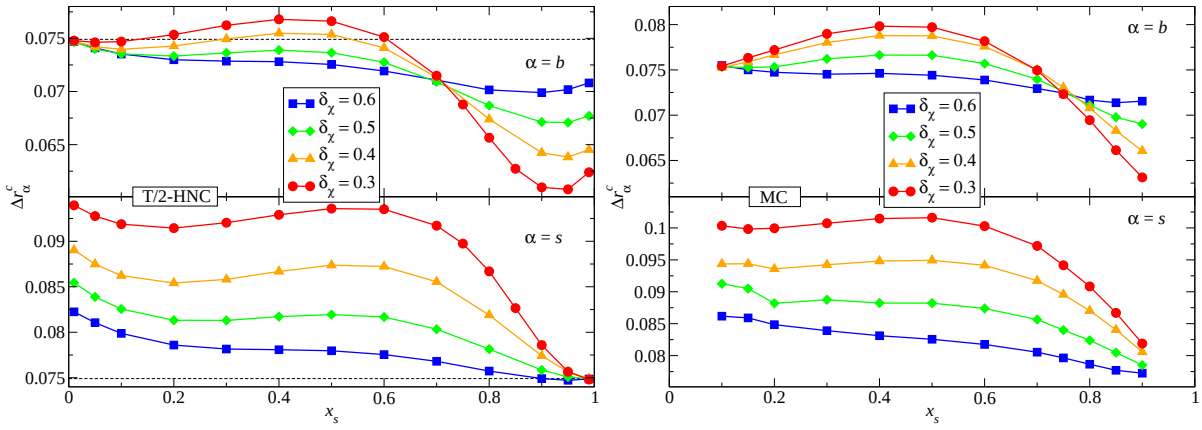

Figure 8.5: The left panels show critical localization length of the big (upper left panel) and the small particles (lower left panel) for the binary point dipole model in 2D calculated by using $T/2$-HNC structure factors. The dashed lines mark the value for monodisperse point dipoles in 2D. The right panels show the corresponding results calculated by using MC structure factors.

understand the complex x_s and δ_χ dependencies of $\Gamma^c(x_s, \delta_\chi)$.

Let us also investigate some further important quantities characterizing the glass transition lines shown in Figs. 8.3 and 8.4. Fig. 8.5 shows critical localization length Δr_α^c for $0.3 \leq \delta_\chi \leq 0.6$ for the binary point dipole model in 2D calculated both by using $T/2$-HNC and MC structure factors as input for MCT. Since we have chosen the inverse square-root $1/\sqrt{n}$ of the total particle number density as unit length, it is clear that it must be $\Delta r_b^c(x_s = 0, \delta_\chi) = \Delta r_s^c(x_s = 1, \delta_\chi) \equiv \Delta r_0^c$ where Δr_0^c is the critical localization length for monodisperse point dipoles in 2D. Furthermore, it is also clear that $\Delta r_b^c(x_s, \delta_\chi) < \Delta r_s^c(x_s, \delta_\chi)$ for all x_s if $0 < \delta_\chi < 1$. Thus, by naively interpolating these results we would obtain a monotonic decrease in Δr_α^c upon increasing x_s. The numerical results, however, demonstrate that Δr_α^c does not monotonically interpolate between the two boundaries $\Delta r_\alpha^c(x_s = 0, \delta_\chi) > \Delta r_\alpha^c(x_s = 1, \delta_\chi)$. Let us focus on the $T/2$-HNC data on the left panel in Fig. 8.5. For instance, the curve for Δr_s^c with $\delta_\chi = 0.3$ clearly exhibits a local minimum at $x_s \cong 0.2$ followed by a local maximum at $x_s \cong 0.6$. The corresponding curve for Δr_b^c is even more complex. It shows three local extrema, two local minima at $x_s \cong 0.05$ and $x_s \cong 0.95$ and a local maximum in between at $x_s \cong 0.4$. It seems that Δr_b^c becomes maximal (minimal) close to the regions in x_s where Γ^c becomes minimal (maximal), see also Fig. 8.4. It is further remarkable that all curves for Δr_b^c for different values of δ_χ intersect at $x_s \cong 0.7$. Now, let us consider the MC results on the right panel in Fig. 8.5. Beside the fact that these data are numerically less accurate (especially for $x_s \leq 0.2$), they support at least the qualitative trends predicted by the $T/2$-HNC approach. Note that the MC results for the curves

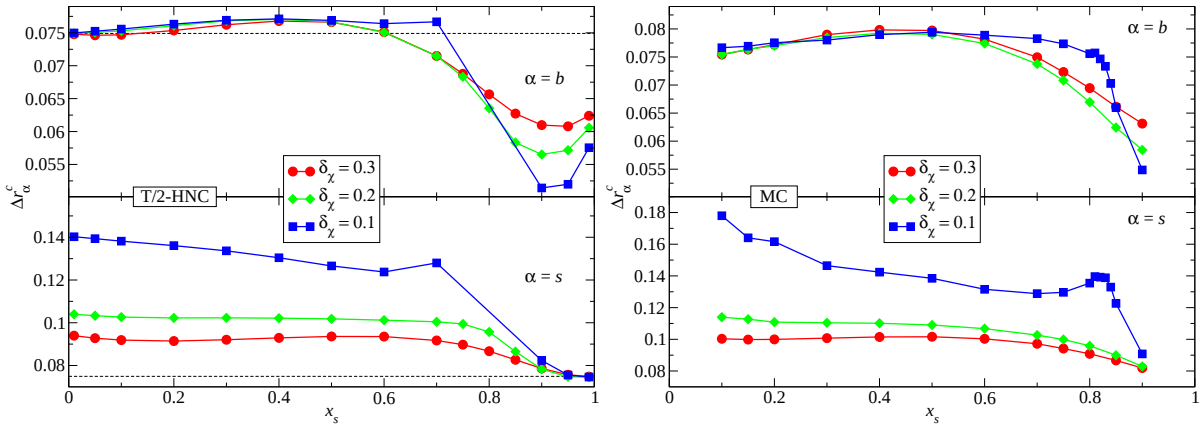

Figure 8.6: The left panels show critical localization length of the big (upper left panel) and the small particles (lower left panel) for the binary point dipole model in 2D with larger disparities in the susceptibilities calculated by using $T/2$-HNC structure factors. The dashed lines mark the value for monodisperse point dipoles in 2D. In the neighborhood of $x_s = 0.8$ and $\delta_\chi = 0.1$ we had problems in finding stable numerical solutions for the $T/2$-HNC structure factors, and thus there are no data points for Δr_α^c in this region. The right panels show the corresponding results calculated by using MC structure factors.

for Δr_b^c for different values of δ_χ also show a common intersection point at $x_s \cong 0.75$.

Fig. 8.6 shows critical localization length Δr_α^c for the binary point dipole model in 2D for larger disparities in the susceptibilities, $0.1 \leq \delta_\chi \leq 0.3$, calculated both by using $T/2$-HNC and MC structure factors as input for MCT. Let us again first focus on the $T/2$-HNC data shown on the left panel in Fig. 8.6. The curve for Δr_s^c for $\delta_\chi = 0.2$ behaves similar to the case $\delta_\chi = 0.3$ which we have already discussed above. It shows two very weakly pronounced extrema, a minimum at $x_s \cong 0.2$ followed by a maximum at $x_s \cong 0.3$. In contrast to the case for $\delta_\chi = 0.3$, the curve for Δr_b^c for $\delta_\chi = 0.2$ exhibits only two local extrema, a maximum at $x_s \cong 0.4$ followed by a minimum at $x_s \cong 0.9$. Apart from the data points for $x_s = 0.7$, the curves for Δr_α^c for $\delta_\chi = 0.1$ are qualitatively similar to the results for $\delta_\chi = 0.2$. As already stated above, in the neighborhood of $x_s = 0.8$ and $\delta_\chi = 0.1$ we had problems in finding stable numerical solutions for the $T/2$-HNC structure factors at higher Γ, and thus we have no data points for Δr_α^c in this region. Let us now turn to the MC results shown on the right panel in Fig. 8.6. On a qualitative level, the data show a similar behavior as the ones for $T/2$-HNC. For $\delta_\chi = 0.1$, the data indicate the development of a new maximum for both Δr_b^c and Δr_s^c at $x_s \cong 0.82$. This may be physically correct, but it also may be a numerical artifact as we will explain in the next paragraphs.

The left panel in Fig. 8.7 shows exponent parameters λ^c for the binary point dipole model in 2D for $0.3 \leq \delta_\chi \leq 0.6$ calculated both by using $T/2$-HNC and MC structure

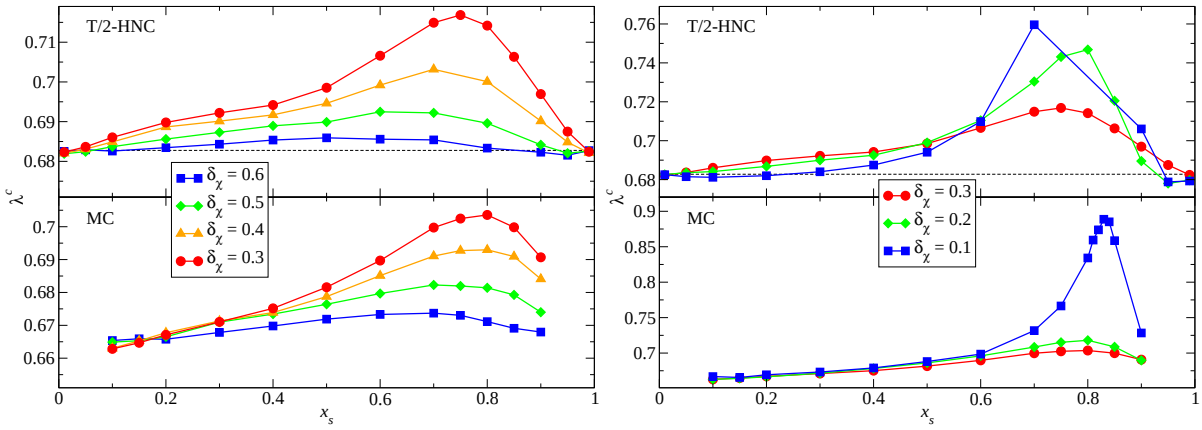

Figure 8.7: Left panels: Exponent parameters for the binary point dipole model in 2D calculated by using $T/2$-HNC structure factors (upper left panel) and MC structure factors (lower left panel). The dashed line in the upper left panel indicates the monodisperse $T/2$-HNC value. Right panels: Exponent parameters for the binary point dipole model in 2D with larger disparities in the susceptibilities calculated by using $T/2$-HNC structure factors (upper right panel) and MC structure factors (lower right panel). The dashed line in the upper right panel indicates the monodisperse $T/2$-HNC value. In the neighborhood of $x_s = 0.8$ and $\delta_\chi = 0.1$ we had problems in finding stable numerical solutions for the $T/2$-HNC structure factors, and thus there are no data points for λ^c in this region in the upper right panel.

factors as input for MCT. Up to smaller numerical uncertainties, the $T/2$-HNC data in the upper left panel indicate that, compared to the monodisperse case, λ^c is always increased for a binary mixture. The corresponding MC results in the lower left panel are qualitatively consistent with the $T/2$-HNC data. Within both approaches, λ^c varies by less than 10%.

The right panel in Fig. 8.7 shows exponent parameters λ^c for the binary point dipole model in 2D for larger disparities in the susceptibilities, $0.1 \leq \delta_\chi \leq 0.3$. For the $T/2$-HNC data in the upper right panel we find $0.67 \leq \lambda^c \leq 0.76$, however, as already stated above, in the neighborhood of $x_s = 0.8$ and $\delta_\chi = 0.1$ we had problems in finding stable numerical solutions for the $T/2$-HNC structure factors at higher Γ, and thus we have no data points for λ^c in this region. Let us now consider the corresponding MC results in the lower right panel. For $\delta_\chi = 0.1$ we observe that λ^c exhibits a narrow maximum at $x_s \cong 0.83$ with maximum value $\lambda^c_{max} \cong 0.89$. This is an indication for the existence of a higher-order singularity of type A_l, $l \geq 3$, in the neighborhood of the control parameter triplet $\delta_\chi = 0.1$, $x_s = 0.83$, $\Gamma = \Gamma^c \cong 140$.

Now, let us come back to the critical localization length Δr^c_α for $\delta_\chi = 0.1$ shown on the right panel in Fig. 8.6. Now we give a reasoning for the conjecture that the development of the maxima at $x_s \cong 0.82$ might be a numerical artifact. As explained in Appendix A.3.2, we use a bisection algorithm monitoring the NEPs for determining

Γ^c for given x_s and δ_χ. At every bisection step, the NEPs are calculated by iterating Eq. (4.18) where for practical purposes we have to limit the maximum number of allowed iterations. It is well-known that in the neighborhood of a higher-order singularity the convergence of this iteration scheme drastically slows down. Thus, for given x_s and δ_χ, our fully automatized computer program for the determination of Γ^c starts to misinterpret values for Γ lying in truth inside the liquid regime as glassy states. In other words, the applied numerical procedure tends to underestimate Γ^c in the neighborhood of higher-order singularities. Such a numerical underestimation of Γ^c would lead to an underestimation of the critical vertices in the MCT functionals which might be the reason for the overestimation of Δr_α^c. Indeed, the glass transition line for $\delta_\chi = 0.1$ shown on the lower right panel in Fig. 8.4 exhibits a weakly pronounced dip at $x_s \cong 0.82$. In order to suppress such problems and investigate in more detail the occurrence of higher-order singularities we would have to increase the maximum number of allowed iterations by about two decades for a more precise determination of the NEPs. At the time of writing of this thesis, this was not possible due to lack of computing time. Let us only remark here that by using MC structure factors for $\delta_\chi = 0.09$ as input for MCT our standard procedure leads to a more strongly pronounced dip in Γ^c at $x_s \cong 0.83$ with $\lambda_{max}^c \cong 0.96$ where, in addition, Δr_s^c displays a sharp peak with maximum value $\Delta r_{s,max}^c \cong 0.36$ (not shown in the figures). At this critical point we also observe that the prepeak in $(\boldsymbol{S}^c)_k^{ss}$ at $k \cong 2.66$ with a maximum value of about 1.78 becomes lager than the "principal" peak in $(\boldsymbol{S}^c)_k^{ss}$ at $k \cong 8.10$ with a maximum value of about 1.76. All these data give strong evidence for the existence a higher-order singularity which is possibly induced by the strong cluster formation of the smaller dipoles [55]. We may even speculate about a glassy state where clusters of small particles behave like bigger dipolar objects which are arrested inside their local potential minima whereas inside such a cluster the small dipoles remain more mobile. Such a mechanism could also explain the strong increase in Δr_s^c. At this point, however, we have to clearly state that our numerical standard procedure may break down in the close neighborhood of higher-order singularities. We leave this topic as an open challenge for the future.

Finally, let us provide an a-posteriori justification for the derivation of Eq. (8.1). It was based on the assumption that the exponent γ following from λ^c does not vary too strongly upon a change from $x_s = 0.3$ to $x_s = 0.5$. By using the MC structure factors for binary point dipoles in 2D we obtain $\lambda^c(x_s = 0.3, \delta_\chi = 0.1) \cong 0.673$ and $\lambda^c(x_s = 0.5, \delta_\chi = 0.1) \cong 0.688$ leading to $\gamma(x_s = 0.3, \delta_\chi = 0.1) \cong 2.21$ and $\gamma(x_s = 0.5, \delta_\chi = 0.1) \cong 2.26$, i.e. the relative change in γ is indeed only about 2%.

Before closing this section, let us conclude that the glass transition scenario for the

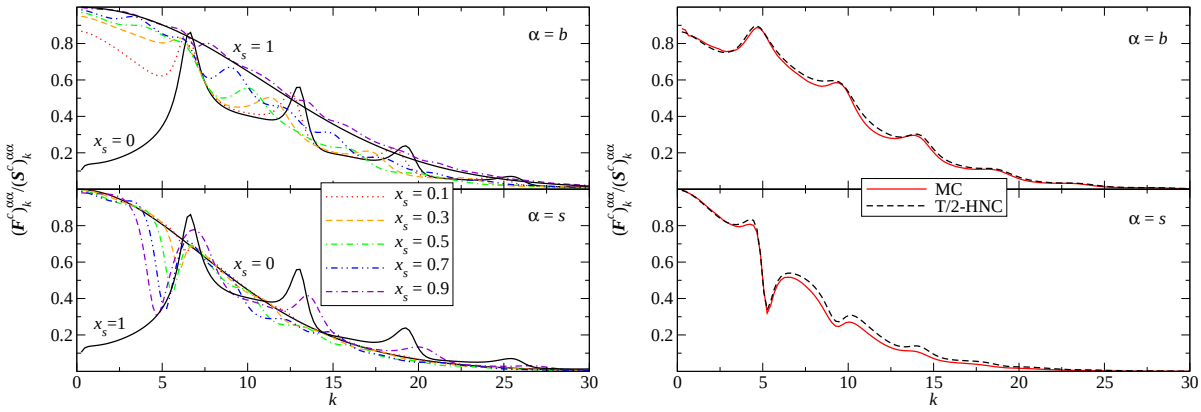

Figure 8.8: Left panels: Normalized critical NEPs for the big (upper left panel) and the small particles (lower left panel) for the binary point dipole model in 2D at $\delta_\chi = 0.3$ calculated by using $T/2$-HNC structure factors. Right panels: Normalized critical NEPs for the big (upper right panel) and the small particles (lower right panel) for the binary point dipole model in 2D at $\delta_\chi = 0.1$ and $x_s = 0.5$ calculated by using $T/2$-HNC structure factors compared to those obtained with MC structure factors.

binary point dipole model in 2D differs qualitatively from those of binary hard disk in 2D or hard spheres in 3D. While for the latter two models a small size disparity leads to a stabilization of the glass, for binary point dipoles in 2D we have found always a stabilization of the liquid due to mixing. However, we have also presented some features shared by all investigated models. For all cases we have found for instance that the glass transition lines become almost symmetric with respect to the equimolar composition $x_s = 1/2$ in the limit of small disparity in the sizes or susceptibilities, respectively. It remains a challenge to understand the basic physical mechanisms leading to all the complex mixing scenarios presented in this and in the previous chapter.

8.3.2 Mixing scenarios

In this section we analyze in how far the mixing effects on the density correlation functions we have found for the binary hard disk model in 2D in the previous chapter can also be rediscovered for binary mixtures of point dipoles in 2D.

Let us first focus on the NEPs. Due to the non-monotonic x_s-dependencies of the critical localization length Δr^c_α, see Figs. 8.5 and 8.6, we can not expect that the normalized critical NEPs $(\boldsymbol{F}^c)^{\alpha\alpha}_k/(\boldsymbol{S}^c)^{\alpha\alpha}_k$ show a monotonic variation with x_s as we have found for the binary hard disk model in 2D for not too small k. This is exemplified on the left panel in Fig. 8.8 which shows normalized critical NEPs for the binary point dipole model in 2D at $\delta_\chi = 0.3$ calculated by using $T/2$-HNC structure factors as input for MCT. We can not read off such a systematic trend from these data as from the

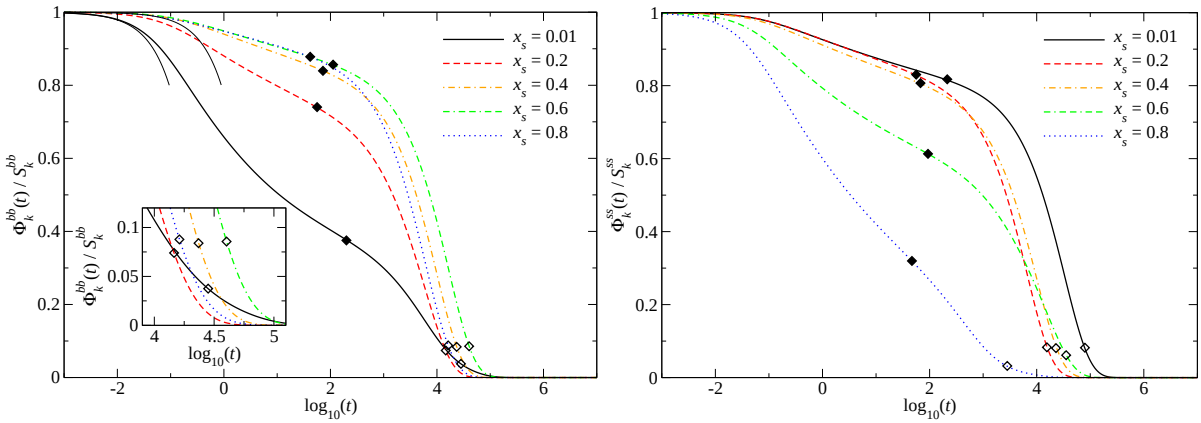

Figure 8.9: The left panel shows normalized correlators of the big particles for the binary point dipole model in 2D at $\Gamma = 95$, $\delta_\chi = 0.3$, and $k = 4.8606$ calculated by using $T/2$-HNC structure factors as input for MCT. Filled diamonds mark the crossings of the normalized critical plateau values $(\boldsymbol{F}^c)_k^{bb}/(\boldsymbol{S}^c)_k^{bb}$. Open diamonds mark the crossings of the values $0.1(\boldsymbol{F}^c)_k^{bb}/(\boldsymbol{S}^c)_k^{bb}$. The thin lines on the left panel show the short-time asymptotes given by Eq. (4.3) for $x_s = 0.01$ and $x_s = 0.4$ (from left to right). The right panel shows the corresponding correlators for the small particles.

NEPs for binary hard disks in 2D shown in Fig. 7.8 which increase monotonically upon increasing the concentration of the smaller particles if k is not too small.

The right panel in Fig. 8.8 shows a comparison of critical NEPs $(\boldsymbol{F}^c)_k^{\alpha\alpha}/(\boldsymbol{S}^c)_k^{\alpha\alpha}$ for a binary mixture of point dipoles in 2D at $\delta_\chi = 0.1$ and $x_s = 0.5$ calculated by using $T/2$-HNC structure factors as input for MCT to the corresponding ones obtained by using MC simulated structure factors. The results from both approaches agree very well, hence we can be confident that the results on the left panel in Fig. 8.8 should not contain $T/2$-HNC specific artifacts on the qualitative level.

Now we consider time-dependent quantities. Fig. 8.9 shows normalized correlators $\Phi_k^{\alpha\alpha}(t)/S_k^{\alpha\alpha}$ for the binary point dipole model in 2D at $\Gamma = 95$, $\delta_\chi = 0.3$, and $k = 4.8606$ calculated by using $T/2$-HNC structure factors as input for MCT. We have chosen this wave number to be located below the principal peak in $(\boldsymbol{F}^c)_k^{bb}/(\boldsymbol{S}^c)_k^{bb}$ at $x_s = 0$ (see Fig. 8.8), similar to our choice for the binary hard disk model in 2D in the previous chapter. Again, we define $(\tilde{\boldsymbol{\tau}}^{rel})_k^{\alpha\alpha}$ as the characteristic time scale specified by 90% of the decay of such a correlator from its normalized plateau value $(\boldsymbol{F}^c)_k^{\alpha\alpha}/(\boldsymbol{S}^c)_k^{\alpha\alpha}$ to zero (see the open diamonds in Fig. 8.9). For the considered value of δ_χ, the corresponding glass transition line exhibits two maxima at $x_s \cong 0.2$ and $x_s \cong 0.9$ and a local minimum in between at $x_s \cong 0.6$, see Fig. 8.4. Hence, starting with the almost monodisperse system at $x_s = 0.01$ and increasing the concentration of the smaller dipoles to $x_s = 0.2$ leads to an increase in the distance $\Gamma^c(x_s, \delta_\chi) - \Gamma$ to the glass transition line and thus to

a decrease in $(\tilde{\boldsymbol{\tau}}^{rel})_k^{\alpha\alpha}$. Upon further increasing the concentration of the smaller dipoles up to $x_s = 0.6$ leads to a decrease in $\Gamma^c(x_s, \delta_\chi) - \Gamma$ which then leads to an increase in $(\tilde{\boldsymbol{\tau}}^{rel})_k^{\alpha\alpha}$. If we continue increasing the concentration of the smaller dipoles to $x_s = 0.8$, then the distance $\Gamma^c(x_s, \delta_\chi) - \Gamma$ to the glass transition line increases again, leading to a decrease in $(\tilde{\boldsymbol{\tau}}^{rel})_k^{\alpha\alpha}$. For the chosen value of k, the plateau values $(\boldsymbol{F}^c)_k^{\alpha\alpha}/(\boldsymbol{S}^c)_k^{\alpha\alpha}$ indicated by the filled diamonds in Fig. 8.9 for $\alpha = b$ increase monotonically with x_s while the corresponding ones for $\alpha = s$ exhibit a non-monotonic x_s-dependence for the three lowest considered values for x_s, see also Fig. 8.8.

So far, the binary point dipole model in 2D shows a mixing scenario which differs in some aspects from the one of the binary hard disk model in 2D studied in the last chapter. However, we can also observe a mixing effect which we have already found for binary mixtures of hard disks in 2D, namely the slowing down of the relaxation of the correlators of the big particles at not too large k towards their plateaus in the sense that $\Phi_k^{bb}(t)/S_k^{bb}$ versus $\log_{10}(t)$ becomes flatter upon increasing the concentration x_s of the smaller particles. On the left panel in Fig. 8.9 we can clearly observe the above described flattening of $\Phi_k^{bb}(t)/S_k^{bb}$ upon increasing $x_s = 0.01$ to 0.4. The shown short-time asymptotes for $x_s = 0.01$ and $x_s = 0.4$ resulting from Eq. (4.3) which fall already at $\log_{10}(t) \cong -1$ significantly below the corresponding correlators give evidence that the flattening of the curves in the region $0 < \log_{10}(t) < 2$ is not only a trivial result following from the slowing down of the diffusion at short times. In fact, for our choice $\delta_\chi = 0.3$ we observe upon increasing $x_s = 0.01$ to $x_s = 0.4$ a monotonic increase in the time constant t_0 [see Eq. (4.30)] which competes with a slight monotonic decrease in the critical exponent a and a monotonic decrease in the critical amplitudes $(\boldsymbol{H}^c)_k^{bb}/(\boldsymbol{S}^c)_k^{bb}$ for $2.9 < k < 5.7$ (not shown in the figures). The latter two effects contribute to the flattening of the $\Phi_k^{bb}(t)/S_k^{bb}$ versus $\log_{10}(t)$ curves for times within the first scaling-law regime. Let us also note that for $0.01 \leq x_s \leq 0.2$ the critical amplitudes $(\boldsymbol{H}^c)_k^{bb}/(\boldsymbol{S}^c)_k^{bb}$ decrease monotonically upon increasing x_s for all $0 < k < 6.2$ which is qualitatively similar to our results for binary hard disks in 2D.

8.3.3 Asymptotic scaling laws

Let us also test the validity of the asymptotic scaling laws for the binary point dipole model in 2D along the lines of Sect. 7.2.3. For this purpose, we use MC simulated static structure factors as input for MCT. Furthermore, we have decided to choose the control parameters to be close to the ones of König et al. [26]. For the following, we consider binary mixtures of point dipoles in 2D with $\delta_\chi = 0.1$ and $x_s = 0.3$, 0.5. Following

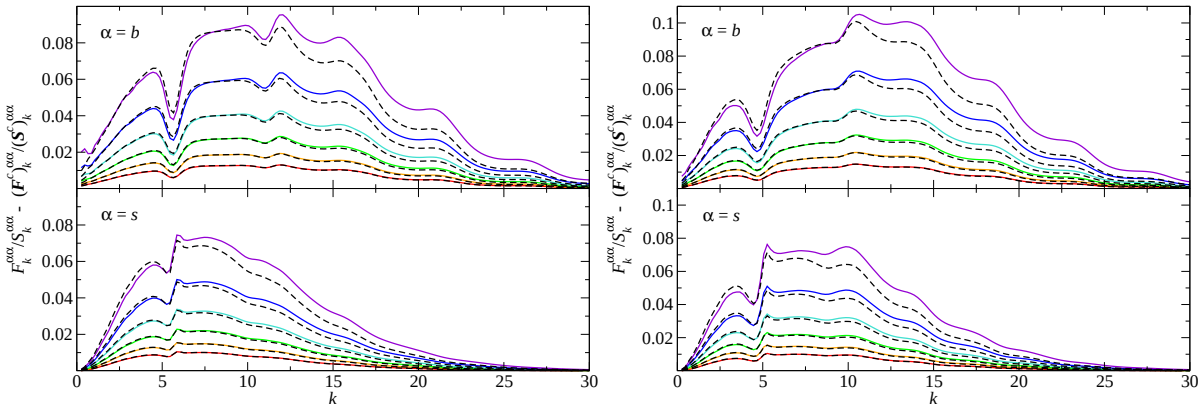

Figure 8.10: Left panels: The increase of the normalized plateau values of the correlators of the big (upper left panel) and the small particles (lower left panel) in the glassy state for the binary point dipole model in 2D at $\delta_\chi = 0.1$, $x_s = 0.3$, and $\varepsilon = (\Gamma - \Gamma^c)/\Gamma^c = 10^{-l/3}$, $l = 5, \ldots, 10$ (from up to down). The dashed lines show the leading-order $\varepsilon^{1/2}$-asymptotes $[(\boldsymbol{H}^c)_k^{\alpha\alpha}/(\boldsymbol{S}^c)_k^{\alpha\alpha}]\sqrt{\sigma/(1-\lambda^c)}$. $\sigma \cong 0.25\varepsilon$ is obtained via numerical differentiation of Eq. (4.21) and $\lambda^c \cong 0.673$ follows from Eq. (4.22). The data were all calculated by using MC structure factors. Right panels: The same as the left panels but for $x_s = 0.5$, $\lambda^c \cong 0.688$, and $\sigma \cong 0.25\varepsilon$.

Sect. 7.2.3, for fixed δ_χ and x_s we introduce the distance parameter

$$\varepsilon = (\Gamma - \Gamma^c)/\Gamma^c. \tag{8.5}$$

In contrast to the previous section, the unit of time and the the single-particle short-time diffusion coefficients are now chosen such that $D_b^0 = 0.01$ and $D_s^0 = 0.0167$ which obeys the Stokes-Einstein law according to Eq. (5.13) with the experimental value $\delta_R \cong 0.6$ for the size ratio [26].

Fig. 8.10 shows the increase $F_k^{\alpha\alpha}/S_k^{\alpha\alpha} - (\boldsymbol{F}^c)_k^{\alpha\alpha}/(\boldsymbol{S}^c)_k^{\alpha\alpha}$ of the normalized NEPs in the glassy regime for $x_s = 0.3$, 0.5 and $\varepsilon = 10^{-l/3}$, $l = 5, \ldots, 10$. The leading-order $\varepsilon^{1/2}$-asymptotes following from Eq. (4.23) are shown as dashed lines. We observe that the leading-order asymptotic formula describes the increase of the NEPs for the binary point dipole model in 2D more accurately than for the binary hard disk model in 2D, see Fig. 7.10. Apart from the numerical artifacts at the lowest k values, all data for $F_k^{\alpha\alpha}/S_k^{\alpha\alpha} - (\boldsymbol{F}^c)_k^{\alpha\alpha}/(\boldsymbol{S}^c)_k^{\alpha\alpha}$ in Fig. 8.10 with $l \geq 8$, i.e. $\varepsilon \leq 0.002$, are described by the leading-order asymptotic formula on a relative error level below 10% if $k \leq 20.3$.

We also demonstrate the validity of the factorization theorem given by Eq. (4.28) for the binary point dipole model in 2D. The left panel in Fig. 8.11 shows the functions $\{\Phi_k^{bb}(t) - (\boldsymbol{F}^c)_k^{bb}\}/(\boldsymbol{H}^c)_k^{bb}$ for the big dipoles at $\varepsilon \pm 10^{-4}$ for three values of k. Also included are the corresponding numerical solutions for the β-correlator $\mathcal{G}(t)$. The data for $\{\Phi_k^{bb}(t) - (\boldsymbol{F}^c)_k^{bb}\}/(\boldsymbol{H}^c)_k^{bb}$ for the liquid case ($\varepsilon < 0$) deviate less than 10% from $\mathcal{G}(t)$

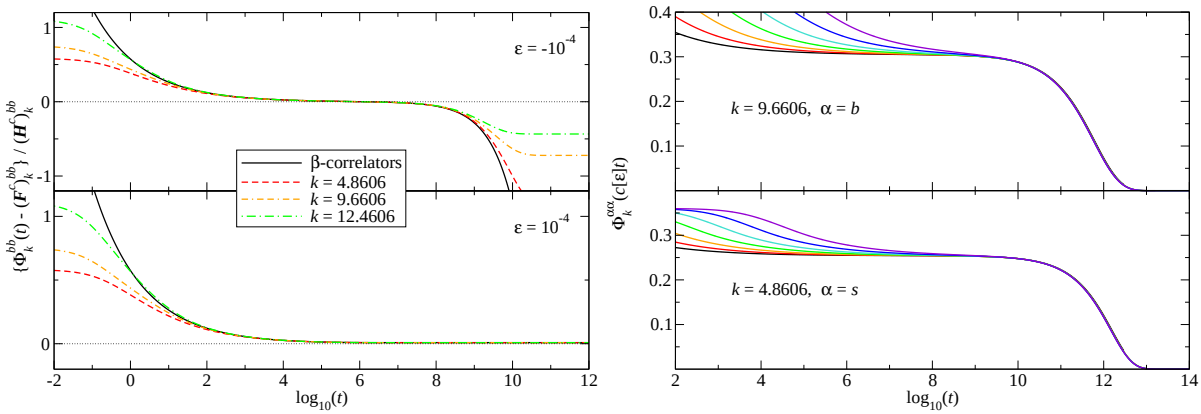

Figure 8.11: Left panels: The plots demonstrate the validity of the factorization theorem for the binary point dipole model in 2D at $\delta_\chi = 0.1$ and $x_s = 0.3$ for both a liquid, $\varepsilon = (\Gamma - \Gamma^c)/\Gamma^c < 0$ and a glassy state ($\varepsilon > 0$). The time constant $t_0 \cong 0.194$ needed for the unique determination of the β-correlator $\mathcal{G}(t)$ was read off from the plateau value of $t^a\{(\boldsymbol{\Phi}^c)_k^{bb}(t) - (\boldsymbol{F}^c)_k^{bb}\}/(\boldsymbol{H}^c)_k^{bb}$ at $k = 9.6606$. Right panels: The plots demonstrate the validity of the α-scaling law for the binary point dipole model in 2D at $\delta_\chi = 0.1$, $x_s = 0.3$, and $\varepsilon = -10^{-l/3}$, $l = 9, ..., 15$ (from right to left). The scaling factors are chosen to be $c[\varepsilon] = (10^5|\varepsilon|)^\gamma$. The numerical value of the exponent $\gamma = (a+b)/(2ab) \cong 2.21$ follows directly from $\lambda^c \cong 0.673$. With this, the correlators collapse onto the corresponding curves with $l = 15$ for long times without the use of any fit parameters. All data were calculated by using MC structure factors.

within the time interval $1.8 < \log_{10}(t) < 8.2$. This interval is more than one decade larger than the corresponding one for the binary hard disk model in 2D. For the glass ($\varepsilon > 0$), the data for $\{\Phi_k^{bb}(t) - (\boldsymbol{F}^c)_k^{bb}\}/(\boldsymbol{H}^c)_k^{bb}$ deviate less than 10% from $\mathcal{G}(t)$ for $\log_{10}(t) > 1.8$.

Finally, let us also investigate the α-scaling law given by Eqs. (4.35) and (4.36) for binary point dipoles in 2D. The right panel in Fig. 8.11 shows rescaled density correlators $\Phi_k^{\alpha\alpha}(c[\varepsilon]t)$ with scaling factors $c[\varepsilon] = (10^5|\varepsilon|)^\gamma$ for $\varepsilon = -10^{-l/3}$, $l = 9, ..., 15$, and $\alpha = b$ with $k = 9.6606$, and also for $\alpha = s$ with $k = 4.8606$. Within the time interval $7.0 < \log_{10}(t) < 12.3$ all data for $l > 15$ deviate less than 10% from the ones for $l = 15$ such that there holds additionally $\Phi_k^{\alpha\alpha}(c[\varepsilon]t) > 0.1(\boldsymbol{F}^c)_k^{\alpha\alpha}$. This interval is also more than one decade larger than the corresponding one for binary hard disks in 2D.

8.4 Summary

By comparing experimentally measured partial structure factors to those from our MC simulations for the binary point dipole model in 2D we have demonstrated that the thermodynamic equilibrium state of the experimental system of König et al. [26] is indeed well described by assuming point particles in 2D which interact only via magnetic

dipole-potentials induced by an external magnetic field. With the $T/2$-HNC closure given by Eq. (8.2) we have proposed a simple empirical ansatz for a bridge function in Eq. (4.45) which yields reasonable results for the static structure factors for the considered model system without the use of adjustable parameters. Again, we have demonstrated the strong predictive power of our slope formula, Eq. (6.7), by evaluating it in the weak-mixing limits $x_\alpha \to 0$. For a large range of susceptibility ratios $0.1 \leq \delta_\chi \leq 0.9$ we have calculated the glass transition lines for the binary point dipole model in 2D in the framework of MCT. We have found that mixing always stabilizes the liquid state, in contrast to the results for binary hard disks in 2D or binary hard spheres in 3D presented in the previous chapter. However, we have also found some similarities. For small disparities in the susceptibilities, i.e. $0 < (1 - \delta_\chi) \ll 1$, the glass transition lines become almost symmetric with respect to the equimolar composition $x_s = 1/2$ and are, to leading order, quadratic in the disparity $(1 - \delta_\chi)$. Furthermore, for $\delta_\chi = 0.3$ we have demonstrated that starting with $x_s = 0$ and increasing the concentration x_s of the smaller particles leads for not too large k to a slowing down of the relaxation of the normalized correlators $\Phi_k^{bb}(t)/S_k^{bb}$ of the big dipoles towards their plateaus in the sense that the $\Phi_k^{bb}(t)/S_k^{bb}$ versus $\log_{10}(t)$ curve becomes flatter upon increasing x_s. The asymptotic scaling laws seem to have a somewhat larger range of validity for the binary point dipole model in 2D than for the binary hard disk model in 2D, at least for the liquid-glass transition points we have investigated. The relaxation behavior of the experimentally obtained self-correlators of König et al. [26] at $\delta_\chi \cong 0.1$ for $x_s \cong 0.3$ and $x_s \cong 0.5$ clearly supports the plasticization effect predicted by MCT. This indicates that at least on a qualitative level MCT may be able to describe the change in the relaxation behavior upon composition changes. The experimental data also show that MCT systematically overestimates the scale for the glass transition temperature by more than a factor of two, as is well-known also for other systems [2].

Chapter 9

Binary mixtures of dipolar hard disks

Motivated by the experiments of König et al. [26] we have formulated the model of dipolar hard disks in 2D whose pair-potentials are given by Eq. (5.12) in Sect. 5.4. This model system includes two types of particle interactions, the short-ranged hard-core repulsions and the long-ranged repulsive dipole-potentials. By neglecting one of these contributions we have obtained two model systems showing qualitatively different glass transition scenarios, the binary hard disk model in 2D and the binary point dipole model in 2D, which we have studied both in detail in the two previous chapters. Now we ask for the glass transition behavior of the full binary dipolar hard disk model in 2D. Since the thermodynamic equilibrium state of this model depends on five independent physical control parameters, namely φ, Γ, δ_R, δ_χ, x_s, the set of liquid-to-glass transition points predicted by MCT will form some 4-dimensional critical hypersurface which we can locally represent for instance as $\Gamma^c(x_s, \varphi, \delta_R, \delta_\chi)$.

Rather than producing a zoo of data for $\Gamma^c(x_s, \varphi, \delta_R, \delta_\chi)$, we dedicate this brief chapter to finding answers to following questions: how would the glass transition behavior of the experimental system of König et al. [26] be influenced if one would use more dense colloidal dispersion such that the 2D packing fraction on the interface plane becomes so large that the system can not be described anymore by a binary mixture of point dipoles in 2D? In addition, how large is the threshold for the 2D packing fraction at which the influence of the hard-core repulsions becomes significant? To explore these questions, we will fix δ_R and δ_χ to the experimental values and calculate Γ^c as a function of x_s for several values of φ.

In the following, we consider binary mixtures of dipolar hard disks in 2D with size ratio $\delta_R = 0.6$ and susceptibility ratio $\delta_\chi = 0.1$ which are roughly the experimental values of König et al. [26]. We further specify that the wave number k shall be discretized according to Eq. (4.16) with $K = 250$ and $\Delta k = 0.2$. For the offset we choose $\hat{o}_2 =$

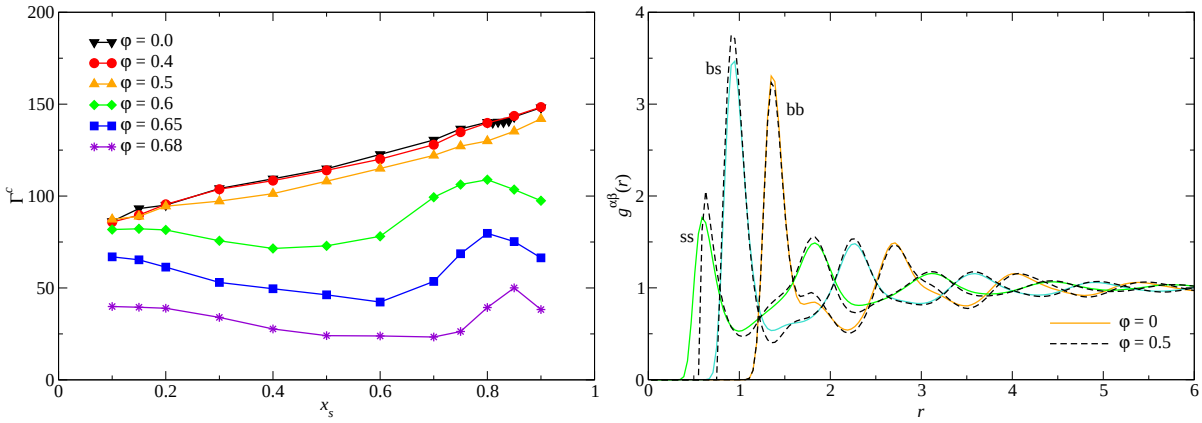

Figure 9.1: Left panel: Glass transition lines for binary mixtures of dipolar hard disks in 2D with size ratio $\delta_R = 0.6$ and susceptibility ratio $\delta_\chi = 0.1$ calculated by using MC structure factors. Right panel: Pair distribution functions for the binary point dipole model in 2D (solid lines) at $\Gamma = 100$, $\delta_\chi = 0.1$, and $x_s = 0.5$ compared to a corresponding binary mixture of dipolar hard disks in 2D (dashed lines) with size ratio $\delta_R = 0.6$ and packing fraction $\varphi = 0.5$. The data were obtained from MC simulations.

0.303 [18]. The natural unit length is given by the inverse square-root $1/\sqrt{n}$ of the total particle number density. Since we will only calculate glass transition lines for the specified model system, i.e. we will calculate Γ^c as a function of x_s for several values of the packing fraction φ, it is not necessary to specify the single-particle short-time diffusion coefficients D^0_α. Static structure factor input for MCT is taken from MC simulations (see Appendix A.1).

9.1 Mode-coupling results

The left panel in Fig. 9.1 shows glass transition lines for binary mixtures of dipolar hard disk in 2D at $\delta_R = 0.6$, $\delta_\chi = 0.1$, and different values for the total packing fraction φ, calculated by using MC simulated static structure factors as input for MCT. We observe that the glass transition line for $\varphi = 0.4$ is almost identical to the one for $\varphi = 0$ with the data taken from Fig. 8.4. The influence of the hard-core repulsions becomes significant for $\varphi \geq 0.5$. As expected, Γ^c shifts to smaller values upon further increasing φ. The glass transition lines for $\varphi \geq 0.6$ are S-shaped with a minimum followed by a maximum. These glass transition lines qualitatively resemble the ones for binary mixtures of hard disks in 2D at similar values for δ_R (see Fig. 7.3). With this, we can conclude that the glass transition scenario in Fig. 9.1 results from a competition of the mixing effects for binary hard disks in 2D and those for binary point dipoles in 2D.

Let us also briefly discuss the underlying physical mechanisms. The right panel in

Fig. 9.1 shows a comparison of MC simulated pair distribution functions $g^{\alpha\beta}(r)$ for a binary mixture of point dipoles in 2D ($\varphi = 0$) at $\delta_\chi = 0.1$, $x_s = 0.5$, and $\Gamma = 100$ (which is close to the MCT liquid-glass transition point) to those of a corresponding binary mixture of dipolar hard disk in 2D with $\delta_R = 0.6$, and $\varphi = 0.5$. While $g^{bb}(r)$ and $g^{bs}(r)$ are only slightly influenced by the change from $\varphi = 0$ to $\varphi = 0.5$, the shape of the principal peak in $g^{ss}(r)$ changes from a smooth maximum to a sharp spike whose left wing exhibits a large discontinuous jump from zero to some finite contact value which indicates that collisions of the hard cores of the smaller disks become highly probable. This behavior is intuitively clear since for the chosen control parameters the dipolar pair-potentials obey $u^{ss}(r) = 0.01u^{bb}(r)$ and $u^{bs}(r) = 0.1u^{bb}(r)$ whereas for the radii of the disks we have $R_s = 0.6R_b$. Compared to the case $\varphi = 0$, the discontinuity in $g^{ss}(r)$ occurring for $\varphi = 0.5$ leads to more strongly pronounced oscillations in S_k^{ss} (not shown in the figures) which encodes stronger static correlations and thus leads to a decrease in the critical interaction parameter Γ^c.

9.2 Summary

In this brief chapter we have investigated the glass transition behavior of binary mixtures of dipolar hard disks in 2D with size ratio $\delta_R = 0.6$ and susceptibility ratio $\delta_\chi = 0.1$ which are roughly the experimental values of König et al. [26]. While for $0 < \varphi \leq 0.4$ the glass transition lines are almost identical to the corresponding one of the binary point dipole model in 2D at $\delta_\chi = 0.1$, at higher values for φ the glass transition lines qualitatively resemble the S-shaped curves for binary mixtures of hard disks in 2D at similar values for δ_R shown in Fig. 7.3. These results demonstrate that there is a competition between the mixing effects for binary hard disks in 2D and those for binary point dipoles in 2D. We have given evidence that the influence of the hard-core repulsions on the glass transition lines becomes significant at packing fractions where collisions of the hard cores of the smaller dipolar disks become highly probable, and thus these become less mobile.

Chapter 10

Summary and conclusions

Let us summarize the most important results presented in this thesis and also draw some conclusions from them.

Concerning analytical results, we have extended the well-established MCT equations [2] to multicomponent systems in $d \geq 2$ spatial dimensions, see Eqs. (4.1)-(4.15). Furthermore, we have derived a general expression, Eq. (2.26), for the slope of a so-called critical line. On the basis of MCT for two model systems, namely the d-dimensional hard sphere model (with $d = 2$ and $d = 3$), and the binary point dipole model in 2D, we have demonstrated that our slope formula can serve as a powerful tool for a fast and precise prediction of some properties of glass transition lines. This was achieved by evaluating the slopes of the glass transition lines in the low concentration limits of one particle species. Note that the applicability of our slope formula is not restricted to MCT for binary mixtures. For instance, applying it to MCT for monodisperse hard sphere models with additional attractive potentials [59] in the limit of vanishing interaction strength should allow a precise determination of the parameter regime at which reentrant glass transitions occur. More generally, Eq. (2.26) can, in principle, be applied to any physical model system which exhibits a locally smooth critical hypersurface.

Motivated by the experiments of König et al. [26], we have applied our new MCT equations to three model systems in 2D: binary mixtures of hard disks, binary mixtures of point dipoles, and binary mixtures of dipolar hard disks.

The glass transition scenarios predicted by MCT for binary hard disks in 2D and binary hard spheres in 3D are qualitatively identical. In particular, for the 2D model we have found the same four mixing effects as have been reported before by Götze and Voigtmann [25] for the 3D case. The stabilization of the glass due to mixing occurring for small size disparities is more strongly pronounced in 2D. For both systems we have found that for small size disparities the glass transition lines become symmetric with

respect to the equimolar composition $x_s = 1/2$ and are, to leading order, quadratic in the disparity $(1-\delta_R)$. The stabilization of the glass becomes then maximal at $x_s = 1/2$. All these results give evidence that the physical mechanisms for glass formation are not sensitive to changing $d = 2$ to $d = 3$.

The glass transition lines we have found for binary hard disks in 2D show a striking similarity to the corresponding random close packing lines calculated by Okubo and Odagaki [49]. To our knowledge, such a systematic comparison has never been published before. Furthermore, the four mixing effects predicted by MCT for the binary hard disk model in 2D are, on a qualitative level, also observable in corresponding Brownian dynamics simulation results of Weysser [51]. These two facts strongly support the quality of MCT in 2D. The simulation data of Weysser [51] also show that MCT underestimates the critical packing fraction for vitrification by about 15%, similar to the case of hard spheres in 3D [2]. A more detailed study, including a quantitative comparison of MCT results for binary hard disk in 2D to corresponding simulation data, was still work in progress [52] at the time of writing of this thesis.

For larger size disparities MCT predicts plasticization, i.e. an enhancement of the liquid regime due to mixing, for both binary hard disks in 2D and binary hard spheres in 3D. In previous works this effect was related to entropic forces [25, 59, 60, 61]. However, the maximum-shape variation of the critical packing fraction φ^c for binary hard disks in 2D in this parameter regime is very similar to the one of the random close packing fraction φ^{rcp} (see Fig. 7.3) obtained by Okubo and Odagaki [49] with a non-equilibrium procedure which locally maximizes the density. Furthermore, for binary hard spheres in 3D, the numerical results for the slopes of the glass transition lines in the limit $x_s \to 0$ and $0 < \delta_R \ll 1$ shown on the left panel in Fig. 7.1 are in quantitative agreement with Eq. (7.1) whose derivation was based on simple geometric arguments. These facts give evidence that the plasticization effect predicted by MCT for binary hard disks in 2D and binary hard spheres in 3D is of geometric rather than entropic origin.

Let us also add that we have still not found an intuitive physical explanation for the stabilization of the glass predicted by MCT for both binary hard disks in 2D and binary hard spheres in 3D with small size disparities. The minimum-shape variation of the critical packing fraction φ^c for binary hard disks in 2D in this parameter regime is again very similar to the one of the random close packing fraction φ^{rcp} obtained by Okubo and Odagaki [49], see Fig. 7.3. Thus, we may speculate that the stabilization of the glass due to mixing could also be of geometric origin.

Götze and Voigtmann [25] have tried to explain the stabilization of the glass predicted by MCT for binary hard spheres in 3D by a qualitative discussion of the total structure

factors $S_k^{tot} = \sum_{\alpha\beta} S_k^{\alpha\beta}$. They have argued that the slight broadening of the principal peak in S_k^{tot} upon changing $\delta_R = 1$ to $0 < (1-\delta_R) \ll 1$, which also occurs for binary hard disks in 2D, may explain the observed effect. At this point we have to state that one has to be more careful in using such arguments: if we take the above argument by word then we should at least for $0 < (1 - \delta_R) \ll 1$ be able to reproduce the glass transition lines shown in Fig. 7.3 on a qualitative level by using the one-component versions of the MCT equations with S_k^{tot} as input. For the binary hard disk model in 2D we have found, however, that this approach yields even for the largest investigated $\delta_R = 0.9$ an increase in φ^c due to mixing. To proceed in understanding the stabilization of the glass (liquid) predicted by MCT, we would need to find clear criteria under which changes in the static structure factor matrix $\boldsymbol{S}$ lead to positive-semi-definite (negative-semi-definite) leading-order increments in the Taylor series of the mode-coupling functional $\boldsymbol{\mathcal{F}}[\boldsymbol{X}, \boldsymbol{X}]$ with respect to $0 < (1 - \delta_R) \ll 1$ for fixed $\boldsymbol{X}$. We leave this issue an an open challenge for the future.

Now, let us review our results for the dipolar model systems. By comparing experimentally measured partial structure factors to those from our MC simulations for the binary point dipole model in 2D we have demonstrated that, at least in the parameter range where the MCT glass transition occurs, the thermodynamic equilibrium state of the experimental system of König et al. [26] is well described by assuming point particles in 2D which interact only via magnetic dipole-potentials induced by an external magnetic field where mutual polarization effects are neglected. As a side result we have suggested a new empirical bridge function approximation for calculating the static structure factors of dipolar systems.

For a large range of susceptibility ratios $0.1 \leq \delta_\chi \leq 0.9$ we have calculated the glass transition lines for the binary point dipole model in 2D in the framework of MCT. We have found that mixing always stabilizes the liquid state, in contrast to the results for binary hard disks in 2D or binary hard spheres in 3D. This demonstrates that the mixing effects strongly depend on the type of particle interactions. We conjecture that the plasticization effect predicted by MCT for the binary point dipole model in 2D is connected to the partial clustering of the smaller dipoles [55], although we have no convincing proof for this. There are also similarities to the results for binary hard disk in 2D. For small disparities in the susceptibilities the glass transition lines become symmetric with respect to the equimolar composition $x_s = 1/2$ and are, to leading order, quadratic in the disparity $(1 - \delta_\chi)$. The plasticization effect becomes then maximal at $x_s = 1/2$. Furthermore, we have demonstrated that the flattening of the $\Phi_k^{bb}(t)/S_k^{bb}$ versus $\log_{10}(t)$ curves upon increasing the concentration x_s of the smaller particles starting with $x_s = 0$

is also observable for the binary point dipole model in 2D at not too large k. This effect can be interpreted as a stiffening of the cages (in case of hard spherical particles) or the local potential minima (in case of point particles), in which the particles are trapped, with respect to spontaneous fluctuations [25].

The relaxation behavior of the experimentally obtained self-correlators of König et al. [26] at $\delta_\chi \cong 0.1$ for $x_s \cong 0.3$ and $x_s \cong 0.5$ clearly supports the plasticization effect predicted by MCT. This indicates that at least on a qualitative level MCT may be able to describe the change in the relaxation behavior upon composition changes. The experimental data also show that MCT systematically overestimates the scale for the glass transition temperature by more than a factor of two, as is well-known also for other systems [2]. To test our MCT predictions more systematically it would be necessary to have data from experiments or computer simulations for a much larger range of both x_s and δ_χ.

The asymptotic scaling laws seem to have a somewhat larger range of validity for the binary point dipole model in 2D than for the binary hard disk model in 2D, at least for the liquid-glass transition points we have investigated. This originates from the fact that for binary hard disks in 2D the separation parameter σ shows a stronger dependence on $(\varphi - \varphi^c)/\varphi^c$ than on $(\Gamma - \Gamma^c)/\Gamma^c$ for binary point dipoles in 2D. It is remarkable that this qualitative feature is also consistent with available data from experiments and computer simulations. From the Brownian dynamics simulation data of Weysser [51], at fixed $x_s = 0.5$, $\delta_R = 5/7$, and $k = 8.5$, we can extrapolate a critical packing fraction of $\varphi^c_{sim} \cong 0.799$. The corresponding correlators at $\varphi = 0.77$, i.e. less than 5% below φ^c_{sim}, show already an almost exponential relaxation without the occurrence of a plateau (not shown in the figures). Now, let us again consider the self-correlators of König et al. [26] at $x_s \cong 0.3$ shown on the upper right panel in Fig. 8.1. The curve for $\Gamma = 200$ develops a plateau, but is still within the liquid regime since the data clearly indicate the onset of the α-relaxation process. The curve for $\Gamma = 134$, i.e. more than 30% below $\Gamma = 200$, still exhibits stretched dynamics. These results indicate that the long-ranged dipolar interactions lead also deeper in the liquid regime to a more efficient suppression of particle rearrangements as the hard-core repulsions do.

For binary hard spheres in 3D, higher-order singularities (connected to the existence of multiple glassy states) occur below $\delta \approx 0.4$ [50]. Although we have already presented some evidence for the existence of such transitions for the 2D model systems studied in this thesis, we leave their systematic investigation as an open challenge for the future, for technical reasons. For the binary point dipole model in 2D we conjecture that the existence of multiple glassy states is also connected to the strong cluster formation of

the smaller dipoles [55].

Finally, we have investigated the glass transition behavior of binary mixtures of dipolar hard disks in 2D with size ratio $\delta_R = 0.6$ and susceptibility ratio $\delta_\chi = 0.1$ which are roughly the experimental values of König et al. [26]. These results demonstrate that at 2D packing fractions which are much higher than the ones in the experiments of König et al. [26] there is a competition of the mixing effects for binary hard disks in 2D and those for binary point dipoles in 2D. This result again supports our conjecture above that the stabilization of the glass due to mixing which occurs for binary hard disk in 2D and hard spheres in 3D is of geometric origin.

Appendix A

Numerical methods

A.1 Monte Carlo simulation

To calculate static structure factors for the model system introduced in Sect. 5.4, we simulate $N = 1600$ particles within a cubic 2D box of dimensionless length $L = \sqrt{N} = 40$ with the standard periodic boundary conditions for particle motion. The unit length is given by $1/\sqrt{n}$, i.e. by the inverse square-root of the particle number density. We arrange 8 virtual copies of the simulation box around it. These so-called image boxes contain at every simulation step exactly the same particle configurations as the main simulation box. To calculate the potential energy of a particle inside the main simulation box, the interactions with all particles within the main and the 8 image boxes are taken into account. This is necessary due to the long-ranged $1/r^3$-parts of the pair-potentials. However, these potentials are absolutely integrable in 2D and thus we can calculate the potential energies without advanced techniques like Ewald summation. A trial move for a chosen particle consists of a local random displacement $\Delta x, \Delta y \in [-\varepsilon, \varepsilon]$, $\varepsilon = 0.15$, of the considered particle (and also of its copies in the image boxes) followed by calculating the potential energy cost Δu for this displacement and choosing a random number $z \in [0, 1]$. The trial move is accepted if $z \leq \exp(-\Delta u / k_B T)$, and rejected, otherwise. Typical acceptance probabilities are between 0.3 and 0.5. A so-called sweep is a sequence consisting of exactly one trial move for every particle in the main simulation box.

The calculation of the static structure factor matrix $\boldsymbol{S}$ consists of four steps. First, we randomly distribute the $N = 1600$ particles. For the simplified version of the model system introduced in Sect. 6.2, i.e. the binary point dipole model in 2D, this step is trivial. For finite particle radii R_α, however, we subsequently include the particles into the simulation box as follows: we declare one of the edges of the box parallel to the x-direction as the "top" and the opposite edge as the "bottom" of the main simulation box.

A randomly chosen particle to be included is first placed by a trial-and-error method at a random position close to the top the box such that its hard core has no overlap with the ones of the particles already located inside the box and also with those of their 8 virtual copies inside the image boxes. Then, a simulated "sedimentation" of the newly included particle towards the bottom of the box follows by applying 10000 trial moves with the random displacements $\Delta x \in [-\varepsilon, \varepsilon]$, $\Delta y \in [-0.09\varepsilon, 0.01\varepsilon]$ and switched-off dipolar interactions where, in addition, the center of the particle is not allowed to cross the top or the bottom of the simulation box. The particle is then fixed at its final position before the procedure is repeated for the next randomly chosen particle to be included. The procedure yields a non-overlapping, densely packed particle configuration located at the bottom of the box. By maximally stretching the y-coordinates of the centers of all particles measured from the bottom of the box by a common factor such that no overlap of the hard cores of the particles and their 8 virtual copies occurs leads to a random configuration which is well-suited to initialize the simulation. As second step, we perform 10000 sweeps for equilibrating the system. As third step, we perform 20000 sweeps to record a histogram for the radial distribution functions $g^{\alpha\beta}(r)$. For this purpose, r is discretized as a Lado grid [62] with a real space cutoff $r_{max} = L/2 = 20$ and 500 grid points. By calculating the Fourier transform of $h^{\alpha\beta}(r) = g^{\alpha\beta}(r) - 1$ according to the Lado method [62] we obtain the raw data for $\boldsymbol{h}$. As last step, we smooth the data. The raw data for $h_k^{\alpha\beta}$ plotted as functions of k are superimposed by oscillations stemming from an interplay of uncertainties of $h^{\alpha\beta}(r)$ at large r and the real space cutoff r_{max}. These oscillations are most significant at small k. We smooth them out by taking the arithmetic average of the upper and lower envelope functions. With this result we calculate the raw data for $\boldsymbol{S}$. Now, for the first few of the lowest k grid points the positive-definiteness of $\boldsymbol{S}_k$ may be violated. We repair this as follows: let l be the smallest index for which $\boldsymbol{S}_{k_j} \succ \boldsymbol{0}$ holds for all $j \geq l$. We set $\boldsymbol{S}_{k_j} = \boldsymbol{S}_{k_{l+1}}$ for $j \leq l$. The whole procedure can be fully automatized.

In order to be able to preform MCT calculations, we transfer the numerical result for $\boldsymbol{S}$ from the Lado grid to the k-grid of the discretized MCT models by linear interpolation. Furthermore, for fixed $0 < x_s < 1$, $0 < \delta_R < 1$, $0 < \delta_\chi < 1$, and $0 < \varphi < 1$ it turns out to be sufficient to calculate and transfer $\boldsymbol{S}$ to the MCT grid for $\Gamma = 20, 40, 60, \ldots$, and then make use of linearly interpolated values for $\boldsymbol{S}$ in between these discrete Γ values. $\boldsymbol{c}$ is then calculated self-consistently from the numerical data for $\boldsymbol{S}$ on the MCT grid via Eq. (4.8).

A.2 Solution of the Ornstein-Zernike equation

We summarize some technical details on the numerical procedure for the solution of the Ornstein-Zernike equation (4.43).

A.2.1 Binary mixtures of hard disks/spheres

For the binary d-dimensional hard sphere model we use the PY closure given by [36]

$$\begin{aligned} h^{\alpha\beta}(r) &= -1, \quad r < (R_\alpha + R_\beta), \\ c^{\alpha\beta}(r) &= 0, \quad r > (R_\alpha + R_\beta). \end{aligned} \tag{A.1}$$

In odd dimensions the coupled Eqs. (4.43) and (A.1) can be solved analytically [63]. In even dimensions numerical methods must be employed. In our numerical solution of the 2D system we use the classical Lado algorithm [62] with a real space cutoff $r_{max} = 50$ with 4000 grid points. The static structure factor matrix $\boldsymbol{S}$ follows then from Eq. (4.8). We transfer the numerical result for $\boldsymbol{S}$ from the Lado grid to the k-grid of the discretized MCT models by linear interpolation. Furthermore, for fixed $0 < x_s < 1$ and $0 < \delta_R < 1$, it turns out to be sufficient to calculate and transfer $\boldsymbol{S}$ to the MCT grid for $\varphi = 0.68$, 0.70, 0.72, and then make use of linearly interpolated values for $\boldsymbol{S}$ for $0.68 < \varphi < 0.70$ and $0.70 < \varphi < 0.72$, respectively. For the calculations on the 3D model, we evaluate the analytical formula for $\boldsymbol{S}$ at $\varphi = 0.514$, 0.518 directly on the MCT grid and use linearly interpolated values for φ in between these boundaries, for convenience. For both 2D and 3D, $\boldsymbol{c}$ is then calculated self-consistently from the numerical data for $\boldsymbol{S}$ on the MCT grid via Eq. (4.8).

In order to analyze in more detail the predictions of MCT as the evaluation of Eq. (6.7) for $x_s \to 0$, we require not only the total and direct correlation functions $\boldsymbol{h}^{(0)}$ and $\boldsymbol{c}^{(0)}$ evaluated in this limit, but also their derivatives $\boldsymbol{h}^{(1)}$ and $\boldsymbol{c}^{(1)}$ with respect to x_s at $x_s = 0$ and $\varphi = \varphi_0^c$, i.e. at the critical packing fraction of the monodisperse system, see Appendix B. For this purpose we solve the linear integral equations resulting from direct differentiation of the Eqs. (4.43) and (A.1). For the d-dimensional binary hard sphere model these are given explicitly by Eqs. (B.31) and (B.32) which require the solution of Eqs. (4.43) and (A.1) at $x_s = 0$ and $\varphi = \varphi_0^c$ as input. Thus, we first determine the critical packing fractions φ_0^c of the monodisperse models as follows: we set $x_s = 1/2$, $\delta_R = 1$, and evaluate $\boldsymbol{S}$ for $\varphi = 0.690$, 0.692 for $d = 2$ and $\varphi = 0.514$, 0.518 for $d = 3$. Then by using linearly interpolated values for $\boldsymbol{S}$ for $0.69 < \varphi < 0.692$ and $0.514 < \varphi < 0.518$, respectively, we apply the procedure described in Appendix A.3.1. For the 2D model,

we use then a straightforward modified version of the original Lado algorithm [62] at φ_0^c with a real space cutoff $r_{max} = 50$ and 4000 grid points. The obtained numerical results for $\boldsymbol{c}^{(0)}$ and $\boldsymbol{c}^{(1)}$ are then transferred to the k-grid of the discretized MCT model by linear interpolation. In 3D, we directly evaluate the analytical formulas for $\boldsymbol{c}^{(0)}$ and $\boldsymbol{c}^{(1)}$ on the MCT k-grid at φ_0^c. For both 2D and 3D, $\boldsymbol{S}^{(0)}$ and $\boldsymbol{S}^{(1)}$ follow then self-consistently from Eq. (4.8). For $x_s = 1$, the procedure is the same.

A.2.2 Binary mixtures of point dipoles in 2D

For the binary point dipole model in 2D we use the $T/2$-HNC closure relation given by

$$\ln[h^{\alpha\beta}(r) + 1] = -2u^{\alpha\beta}(r)/(k_B T) + h^{\alpha\beta}(r) - c^{\alpha\beta}(r). \tag{A.2}$$

For the numerical solution of Eqs. (4.43) and (A.2) we use the classical Lado algorithm [62] with a real space cutoff $r_{max} = 100$ with 4000 grid points and transfer the numerical result for $\boldsymbol{S}$ from the Lado grid to the k-grid of the discretized MCT models by linear interpolation. For fixed $0 < x_s < 1$ and $0 < \delta_\chi < 1$ it turns out to be sufficient to calculate and transfer $\boldsymbol{S}$ to the MCT grid for $\Gamma = 5$, 10, 15, ..., and then make use of linearly interpolated values for $\boldsymbol{S}$ in between these discrete Γ values. $\boldsymbol{c}$ is then calculated self-consistently from the numerical data for $\boldsymbol{S}$ on the MCT grid via Eq. (4.8).

For the MCT calculations in the weak-mixing limit $x_s \to 0$, we determine $\boldsymbol{c}^{(0)}$ and $\boldsymbol{c}^{(1)}$ by solving the linear integral equations resulting from direct differentiation of the Eqs. (4.43) and (A.2) at $x_s = 0$. These are given explicitly by Eqs. (B.31) and (B.33) which require the solution of Eqs. (4.43) and (A.2) at $x_s = 0$ and $\Gamma = \Gamma_0^c$ as input, i.e. at the critical interaction parameter of the monodisperse system. Γ_0^c is determined as follows: We set $x_s = 1/2$, $\delta_\chi = 1$, and evaluate $\boldsymbol{S}$ for $\Gamma = 97.5$, 98.0. Then by using linearly interpolated values for $\boldsymbol{S}$ for $97.5 < \Gamma < 98.0$ we apply the procedure described in Appendix A.3.2. After this, we apply a straightforward modified version of the original Lado algorithm [62] at Γ_0^c with a real space cutoff $r_{max} = 100$ and 4000 grid points. The obtained numerical results for $\boldsymbol{c}^{(0)}$ and $\boldsymbol{c}^{(1)}$ are then transferred to the k-grid of the discretized MCT model by linear interpolation. $\boldsymbol{S}^{(0)}$ and $\boldsymbol{S}^{(1)}$ follow then self-consistently from Eq. (4.8). For $x_s = 1$, the procedure is the same.

A.3 Determination of glass transition lines

We briefly describe the procedure for the determination of glass transition lines.

A.3.1 Binary mixtures of hard disks/spheres

$\varphi^c(x_s, \delta_R)$ can be determined numerically by a simple bisection algorithm monitoring the NEPs. For this purpose, we fix $0 < x_s < 1$ and $0 < \delta_R < 1$, and nest φ until $0 < \varphi - \varphi^c \leq 10^{-7}$ is reached. For the corresponding maximum eigenvalues of $\boldsymbol{\mathcal{C}}$ we obtain typically $r \cong 0.9995$. Such a high accuracy is needed for a quantitative test of the asymptotic scaling laws. For the determination of $\boldsymbol{F}$, which is necessary at each bisection step, we iterate Eq. (4.18) starting with $\boldsymbol{X} = \boldsymbol{S}$ until either (i) $\boldsymbol{F} = \boldsymbol{0}$ (within the numerical accuracy of the used computer) is reached, or (ii) $|\mathcal{I}_k^{\alpha\beta}[\boldsymbol{F}] - F_k^{\alpha\beta}|/|\mathcal{I}_k^{\alpha\beta}[\boldsymbol{F}]| < \varepsilon_1$ for all k, α, β with $\mathcal{I}_k^{\alpha\beta}[\boldsymbol{F}] \neq 0$ is satisfied, or (iii) the maximum allowed number of iterations I_{max} is reached. Finally, we calculate the norm $\|\boldsymbol{F}\| = \max_{k,\alpha,\beta} |F_k^{\alpha\beta}|$ and identify the present state as a liquid if $\|\boldsymbol{F}\| < \varepsilon_2$, and as a glass, otherwise. For the automatized procedure we choose $\varepsilon_1 = 10^{-10}$, $\varepsilon_2 = 10^{-2}$, and $I_{max} = 100000$. We also perform some calculations to quantify discretization effects on φ^c. For this purpose it turns out to be sufficient to choose $\varepsilon_1 = 10^{-6}$ and nest φ until $0 < \varphi - \varphi^c \leq 10^{-5}$ is reached.

So far, there is an intrinsic problem in the procedure: upon approaching the (mathematically) true value of φ^c, the convergence of the iteration scheme toward the true value of $\boldsymbol{F}$ drastically slows down. For a large window of iteration steps, the intermediate results remain close to the critical NEPs. Hence it may happen that the true value for $\boldsymbol{F}$ at given φ is $\boldsymbol{0}$, criterion (ii) or (iii), however, is satisfied before $\|\boldsymbol{F}\| < \varepsilon_2$ holds. In this case, the computer misinterprets the current state as a glass. Then the obtained approximate value for φ^c in truth lies in the liquid regime. Obviously, this problem can never be completely avoided on a real computer where, in addition, also rounding errors occur. Anyhow, to have more confidence in our results, for the final determination of $\boldsymbol{F}^c$ at the numerically obtained φ^c we choose $\varepsilon_1 = 10^{-12}$ and $I_{max} = 200000$, similarly for the eigenvectors $\boldsymbol{H}^c$ and $\hat{\boldsymbol{H}}^c$ (see below). In almost all cases we obtain stable reasonable results. In the remaining few percent of the cases, we choose some appropriate $10^{-12} < \varepsilon_1 < 10^{-6}$ to obtain a reasonable approximation for the critical NEPs. These few problematic data have no influence on the qualitative trends in our results, hence we do not further comment them.

Having determined some $\boldsymbol{F} \succ \boldsymbol{0}$, the right-eigenvector $\boldsymbol{H}$ can be calculated up to a normalization constant by alternately iterating Eq. (4.19) and dividing the intermediate result by its norm. The sequence of the norms obviously converges towards the maximum eigenvalue r of $\boldsymbol{\mathcal{C}}$. The left-eigenvector $\hat{\boldsymbol{H}}$ can be obtained similarly. In a final step, $\boldsymbol{H}$ and $\hat{\boldsymbol{H}}$ have to be normalized according to Eq. (4.20).

A.3.2 Binary mixtures of point dipoles in 2D

The procedure is in principle the same as in Appendix A.3.1. We fix $0 < x_s < 1$ and $0 < \delta_\chi < 1$, and nest Γ until $0 < \Gamma - \Gamma^c \leq 10^{-4}$ is reached. For the corresponding maximum eigenvalues of $\boldsymbol{\mathcal{C}}$ we obtain typically $r \cong 0.9995$. This accuracy is needed for a quantitative test of the asymptotic scaling laws. To quantify discretization effects on Γ^c, it turns out to be sufficient to nest Γ until $0 < \Gamma - \Gamma^c \leq 10^{-2}$ is reached.

A.3.3 Binary mixtures of dipolar hard disks

We fix the parameters $0 < x_s < 1$, $0 < \delta_\chi < 1$, $0 < \delta_R < 1$, and $0 < \varphi < 1$, and determine Γ^c as described in Appendix A.3.2.

A.4 Calculation of time-dependent quantities

For the numerical determination of $\boldsymbol{\Phi}(t)$ we implement the so-called time-decimation algorithm. This multigrid algorithm first published in Ref. [64] is described in detail in Ref. [65] for a schematic MCT model. The generalization to our matrix-valued and k-dependent models is straightforward. One only has to carefully take into account that products of matrices in general do not commute. Our time grids consist of 256 points, as initial step size we choose 10^{-8} time units. For each time step, the implicit equation for $\boldsymbol{\Phi}(t)$ corresponding to Eq. (1.22) in Ref. [65] is iterated until either for all components corresponding to the index triplet k, α, β the relative difference between two subsequent iteration steps is less than 10^{-6} or the maximum number of 10000 iterations is exceeded. Having determined $\boldsymbol{\Phi}(t)$, we can similarly calculate $\underline{\Phi}_\alpha^{self}(t)$ and finally also the $\delta r_\alpha^2(t)$. For the latter, it is convenient to differentiate Eq. (4.13) yielding

$$\frac{1}{D_\alpha^0}\frac{\mathrm{d}}{\mathrm{d}t}[\delta r_\alpha^2(t)] + \int_0^t \mathrm{d}t'\; m_\alpha^{msd}(t-t')\frac{\mathrm{d}}{\mathrm{d}t'}[\delta r_\alpha^2(t')] - 2d = 0. \tag{A.3}$$

Then it is straightforward to modify the time-decimation algorithm to solve Eq. (A.3). The β-correlator $\mathcal{G}(t)$ is determined exactly as described in Ref. [65].

Appendix B

Equations for the weak-mixing limit

Here we will describe how to evaluate the slope of a glass transition line for a binary mixture as specified in Sect. 6.3 at $x_s = 0$, i.e. for a vanishing concentration of the smaller particles. The procedure for a vanishing concentration of the bigger particles $x_b = 0$ is the same. The corresponding formulas are obtained by interchanging the particle indices $b \leftrightarrow s$. Let us further remark that the explicit specialization on a certain model system occurs only on the level of the static input for MCT.

B.1 Rewriting the mode-coupling functional

For the following, it is convenient to rewrite the mode-coupling functional as

$$\boldsymbol{\mathcal{F}} = n\boldsymbol{x}^{-1}\hat{\boldsymbol{\mathcal{F}}}\boldsymbol{x}^{-1} \tag{B.1}$$

where the elements of the matrix $\boldsymbol{x}$ are defined by $x_k^{\alpha\beta} = x_\alpha \delta_{\alpha\beta}$. As can be read off from Eqs. (4.5)-(4.7), $\hat{\boldsymbol{\mathcal{F}}}$ has a binlinear functional dependence on the matrix $\boldsymbol{c}$ of direct correlation functions, and shows no further explicit dependence on the control parameters. $\hat{\boldsymbol{\mathcal{F}}}$ can be considered as a special case of a more general functional $\tilde{\boldsymbol{\mathcal{F}}}$,

$$\hat{\boldsymbol{\mathcal{F}}}[\boldsymbol{X}, \boldsymbol{Y}] = \tilde{\boldsymbol{\mathcal{F}}}[\boldsymbol{c}, \boldsymbol{c}; \boldsymbol{X}, \boldsymbol{Y}], \tag{B.2}$$

$$\tilde{\mathcal{F}}_k^{\alpha\beta}[\boldsymbol{a}, \boldsymbol{b}; \boldsymbol{X}, \boldsymbol{Y}] = \frac{\Omega_{d-1}}{(4\pi)^d} \sum_{\alpha',\beta',\alpha'',\beta''} \int_0^\infty \mathrm{d}p \int_{|k-p|}^{k+p} \mathrm{d}q \; \tilde{V}_{k;p,q}^{\alpha\beta;\alpha'\beta',\alpha''\beta''}[\boldsymbol{a}, \boldsymbol{b}] X_p^{\alpha'\beta'} Y_q^{\alpha''\beta''}, \tag{B.3}$$

$$\tilde{V}_{k;p,q}^{\alpha\beta;\alpha'\beta',\alpha''\beta''}[\boldsymbol{a}, \boldsymbol{b}] = \frac{pq}{k^{d+2}} \tilde{v}_{kpq}^{\alpha\alpha'\alpha''}[\boldsymbol{a}] \tilde{v}_{kpq}^{\beta\beta'\beta''}[\boldsymbol{b}], \tag{B.4}$$

$$\tilde{v}_{kpq}^{\alpha\beta\gamma}[\boldsymbol{z}] = \frac{(k^2 + p^2 - q^2) z_p^{\alpha\beta} \delta_{\alpha\gamma} + (k^2 - p^2 + q^2) z_q^{\alpha\gamma} \delta_{\alpha\beta}}{[4k^2p^2 - (k^2 + p^2 - q^2)^2]^{(3-d)/4}}. \tag{B.5}$$

Hence, for fixed $\boldsymbol{X}$ and $\boldsymbol{Y}$ and some arbitrary external control parameter ξ_i we can write

$$(\partial\hat{\boldsymbol{\mathcal{F}}}/\partial\xi_i)[\boldsymbol{X},\boldsymbol{Y}] = \hat{\boldsymbol{\mathcal{G}}}[\boldsymbol{X},\boldsymbol{Y}], \tag{B.6}$$

$$\hat{\boldsymbol{\mathcal{G}}}[\boldsymbol{X},\boldsymbol{Y}] = \tilde{\boldsymbol{\mathcal{F}}}[\partial\boldsymbol{c}/\partial\xi_i,\boldsymbol{c};\boldsymbol{X},\boldsymbol{Y}] + \tilde{\boldsymbol{\mathcal{F}}}[\boldsymbol{c},\partial\boldsymbol{c}/\partial\xi_i;\boldsymbol{X},\boldsymbol{Y}]. \tag{B.7}$$

B.2 Derivatives of the separation parameter

B.2.1 General case

For a general model system, the calculation of the slope of an arbitrary critical line via Eq. (2.26) requires the calculation of a pair of derivatives of the separation parameter of the form $\partial\sigma/\partial(\Delta\xi_i)|_{\Delta\vec{\xi}=\vec{0}}$. Since in the framework of MCT σ follows from $\tilde{\sigma}$ given by Eq. (4.21) by linearization around $\vec{\xi}^c$, we can write

$$\partial\sigma/\partial(\Delta\xi_i)|_{\Delta\vec{\xi}=\vec{0}} = \partial\tilde{\sigma}/\partial\xi_i|_{\vec{\xi}=\vec{\xi}^c}. \tag{B.8}$$

Only, those quantities on the r.h.s. of Eq. (4.21) without the superscript c are differentiated. Then, all quantities in the resulting formula have to be taken at the critical point $\vec{\xi}^c$. For the following, we drop the superscript c for convenience. With Eqs. (4.21), (B.6) and (B.8) we obtain explicitly

$$\begin{aligned}
\partial\sigma/\partial(\Delta\xi_i)|_{\Delta\vec{\xi}=\vec{0}} \;=\; & n^{-1}(\partial n/\partial\xi_i)(\hat{\boldsymbol{H}}|\{\boldsymbol{S}-\boldsymbol{F}\}n\boldsymbol{x}^{-1}\hat{\boldsymbol{\mathcal{F}}}[\boldsymbol{F},\boldsymbol{F}]\boldsymbol{x}^{-1}\{\boldsymbol{S}-\boldsymbol{F}\}) \\
& +(\hat{\boldsymbol{H}}|\{\boldsymbol{S}-\boldsymbol{F}\}n\boldsymbol{x}^{-1}\hat{\boldsymbol{\mathcal{G}}}[\boldsymbol{F},\boldsymbol{F}]\boldsymbol{x}^{-1}\{\boldsymbol{S}-\boldsymbol{F}\}) \\
& +(\hat{\boldsymbol{H}}|\{\boldsymbol{S}-\boldsymbol{F}\}\boldsymbol{S}^{-1}\{\partial\boldsymbol{S}/\partial\xi_i\}n\boldsymbol{x}^{-1}\hat{\boldsymbol{\mathcal{F}}}[\boldsymbol{F},\boldsymbol{F}]\boldsymbol{x}^{-1}\{\boldsymbol{S}-\boldsymbol{F}\}) \\
& +(\hat{\boldsymbol{H}}|\{\boldsymbol{S}-\boldsymbol{F}\}n\boldsymbol{x}^{-1}\hat{\boldsymbol{\mathcal{F}}}[\boldsymbol{F},\boldsymbol{F}]\boldsymbol{x}^{-1}\{\partial\boldsymbol{S}/\partial\xi_i\}) \\
& +(\hat{\boldsymbol{H}}|\{\boldsymbol{S}-\boldsymbol{F}\}n\{\partial\boldsymbol{x}^{-1}/\partial\xi_i\}\hat{\boldsymbol{\mathcal{F}}}[\boldsymbol{F},\boldsymbol{F}]\boldsymbol{x}^{-1}\{\boldsymbol{S}-\boldsymbol{F}\}) \\
& +(\hat{\boldsymbol{H}}|\{\boldsymbol{S}-\boldsymbol{F}\}n\boldsymbol{x}^{-1}\hat{\boldsymbol{\mathcal{F}}}[\boldsymbol{F},\boldsymbol{F}]\{\partial\boldsymbol{x}^{-1}/\partial\xi_i\}\{\boldsymbol{S}-\boldsymbol{F}\}).
\end{aligned} \tag{B.9}$$

Note that for a one-component model we have $\boldsymbol{x} = \boldsymbol{x}^{-1} = 1$ and thus $\partial\boldsymbol{x}^{-1}/\partial\xi_i = 0$. Let us further remark that the first scalar product on the r.h.s. of Eq. (B.9) is nothing but the well-known exponent parameter $\lambda = (\hat{\boldsymbol{H}}|\{\boldsymbol{S}-\boldsymbol{F}\}\boldsymbol{\mathcal{F}}[\boldsymbol{F},\boldsymbol{F}]\{\boldsymbol{S}-\boldsymbol{F}\})$.

B.2.2 Weak-mixing limit

We specialize Eq. (B.9) to evaluate Eq. (6.7) at $x_s = 0$. Let us start with summarizing some important properties of $\boldsymbol{S}$, $\boldsymbol{F}$, $\hat{\boldsymbol{\mathcal{F}}}$, and $\hat{\boldsymbol{\mathcal{G}}}$. By definition, for $x_s \to 0$ the elements

of $\boldsymbol{S}$ and $\boldsymbol{F}$ satisfy

$$\begin{aligned} S_k^{\alpha\beta} &= \mathcal{O}(x_s) \quad \text{if} \quad (\alpha,\beta) \neq (b,b), \\ F_k^{\alpha\beta} &= \mathcal{O}(x_s) \quad \text{if} \quad (\alpha,\beta) \neq (b,b). \end{aligned} \tag{B.10}$$

Due to the Kronecker deltas in Eq. (B.5), we also have

$$\begin{aligned} \hat{\mathcal{F}}_k^{\alpha\beta}[\boldsymbol{F},\boldsymbol{F}] &= \mathcal{O}(x_s) \quad \text{if} \quad (\alpha,\beta) \neq (b,b), \\ \hat{\mathcal{G}}_k^{\alpha\beta}[\boldsymbol{F},\boldsymbol{F}] &= \mathcal{O}(x_s) \quad \text{if} \quad (\alpha,\beta) \neq (b,b). \end{aligned} \tag{B.11}$$

For the following, we assume Taylor expansions for n, $\boldsymbol{c}$, $\boldsymbol{S}$, $\boldsymbol{F}$, $\boldsymbol{H}$, and $\hat{\boldsymbol{H}}$ in powers of x_s around $x_s = 0$ of the form

$$\boldsymbol{Z} = \boldsymbol{Z}^{(0)} + x_s \boldsymbol{Z}^{(1)} + \mathcal{O}(x_s^2). \tag{B.12}$$

Eq. (B.10) implies

$$\begin{aligned} (\boldsymbol{S}^{(0)})_k^{\alpha\beta} &= 0 \quad \text{if} \quad (\alpha,\beta) \neq (b,b), \\ (\boldsymbol{F}^{(0)})_k^{\alpha\beta} &= 0 \quad \text{if} \quad (\alpha,\beta) \neq (b,b). \end{aligned} \tag{B.13}$$

The Taylor expansions of $\hat{\boldsymbol{\mathcal{F}}}[\boldsymbol{F},\boldsymbol{F}]$ and $\hat{\boldsymbol{\mathcal{G}}}[\boldsymbol{F},\boldsymbol{F}]$ needed below read explicitly

$$\hat{\boldsymbol{\mathcal{F}}}[\boldsymbol{F},\boldsymbol{F}] = \hat{\boldsymbol{\mathcal{F}}}^{(0)}[\boldsymbol{F}^{(0)},\boldsymbol{F}^{(0)}] + x_s \hat{\boldsymbol{\mathcal{G}}}^{(0)}[\boldsymbol{F}^{(0)},\boldsymbol{F}^{(0)}] + 2x_s \hat{\boldsymbol{\mathcal{F}}}^{(0)}[\boldsymbol{F}^{(0)},\boldsymbol{F}^{(1)}] + \mathcal{O}(x_s^2), \tag{B.14}$$

$$\hat{\boldsymbol{\mathcal{G}}}[\boldsymbol{F},\boldsymbol{F}] = \hat{\boldsymbol{\mathcal{G}}}^{(0)}[\boldsymbol{F}^{(0)},\boldsymbol{F}^{(0)}] + \mathcal{O}(x_s), \tag{B.15}$$

where the leading-order functionals are given by

$$\hat{\boldsymbol{\mathcal{F}}}^{(0)}[\boldsymbol{X},\boldsymbol{Y}] = \tilde{\boldsymbol{\mathcal{F}}}[\boldsymbol{c}^{(0)},\boldsymbol{c}^{(0)};\boldsymbol{X},\boldsymbol{Y}], \tag{B.16}$$

$$\hat{\boldsymbol{\mathcal{G}}}^{(0)}[\boldsymbol{X},\boldsymbol{Y}] = \tilde{\boldsymbol{\mathcal{F}}}[\boldsymbol{c}^{(1)},\boldsymbol{c}^{(0)};\boldsymbol{X},\boldsymbol{Y}] + \tilde{\boldsymbol{\mathcal{F}}}[\boldsymbol{c}^{(0)},\boldsymbol{c}^{(1)};\boldsymbol{X},\boldsymbol{Y}]. \tag{B.17}$$

Eq. (B.13) and the Kronecker deltas in Eq. (B.5) imply

$$\begin{aligned} (\hat{\boldsymbol{\mathcal{F}}}^{(0)}[\boldsymbol{F}^{(0)},\boldsymbol{F}^{(0)}])_k^{\alpha\beta} &= 0 \quad \text{if} \quad (\alpha,\beta) \neq (b,b), \\ (\hat{\boldsymbol{\mathcal{G}}}^{(0)}[\boldsymbol{F}^{(0)},\boldsymbol{F}^{(0)}])_k^{\alpha\beta} &= 0 \quad \text{if} \quad (\alpha,\beta) \neq (b,b). \end{aligned} \tag{B.18}$$

A further important implication is the fact that $(\hat{\boldsymbol{\mathcal{F}}}^{(0)}[\boldsymbol{F}^{(0)},\boldsymbol{F}^{(1)}])_k^{\alpha\beta}$ is not dependent on $(\boldsymbol{F}^{(1)})_k^{bb}$ if $(\alpha,\beta) \neq (b,b)$.

Now we consider the numerator in Eq. (6.7). It follows from Eq. (B.9) by choosing $\xi_i = x_s$. Let us focus on the scalar product in the first term on the r.h.s. of Eq. (B.9). The factors $\{\boldsymbol{S}-\boldsymbol{F}\}\boldsymbol{x}^{-1}$, n, $\hat{\boldsymbol{\mathcal{F}}}[\boldsymbol{F},\boldsymbol{F}]$, and $\boldsymbol{x}^{-1}\{\boldsymbol{S}-\boldsymbol{F}\}$ have all well-defined limits for

$x_s \to 0$ which can be calculated independently. Hence, the limit of the second argument of the considered scalar product also exists. Thus, the $x_s \to 0$ limit of the first argument of the scalar product, namely that of $\hat{\boldsymbol{H}}$, can be performed independently with $\hat{\boldsymbol{H}}^{(0)}$ as result. Because of Eqs. (B.14) and (B.18), the final result for the $x_s \to 0$ limit of the first term on the r.h.s. of Eq. (B.9) depends only on the matrix elements with indices $(\alpha, \beta) = (b, b)$. We can write the result explicitly as $\{n^{(1)}/n^{(0)}\}\lambda^{(0)}$ where

$$\lambda^{(0)} = n^{(0)} \sum_k (\hat{\boldsymbol{H}}^{(0)})_k^{bb} \{(\boldsymbol{S}^{(0)})_k^{bb} - (\boldsymbol{F}^{(0)})_k^{bb}\} (\hat{\boldsymbol{\mathcal{F}}}^{(0)}[\boldsymbol{F}^{(0)}, \boldsymbol{F}^{(0)}])_k^{bb} \{(\boldsymbol{S}^{(0)})_k^{bb} - (\boldsymbol{F}^{(0)})_k^{bb}\} \tag{B.19}$$

is nothing but the well-known exponent parameter of the corresponding monodisperse MCT model [2, 24]. The second term on the r.h.s. of Eq. (B.9) can be discussed similarly, here Eqs. (B.15) and (B.18) lead to

$$\mu^{(0)} = n^{(0)} \sum_k (\hat{\boldsymbol{H}}^{(0)})_k^{bb} \{(\boldsymbol{S}^{(0)})_k^{bb} - (\boldsymbol{F}^{(0)})_k^{bb}\} (\hat{\boldsymbol{\mathcal{G}}}^{(0)}[\boldsymbol{F}^{(0)}, \boldsymbol{F}^{(0)}])_k^{bb} \{(\boldsymbol{S}^{(0)})_k^{bb} - (\boldsymbol{F}^{(0)})_k^{bb}\}. \tag{B.20}$$

The treatment of the remaining terms in Eq. (B.9) is somewhat more tedious. For this purpose we write the matrix products occurring as second arguments of the scalar products explicitly in components. By using Eqs. (B.10) and (B.11) we realize that all the inverse powers of x_s stemming from $\boldsymbol{x}^{-1}$ and its derivative with respect to x_s can be compensated by other factors which are of the order x_s. Hence, the $x_s \to 0$ limits for all matrix products occurring as second arguments of the scalar products exist. Thus, for each scalar product, the $x_s \to 0$ limit of $\hat{\boldsymbol{H}}$ can be performed independently yielding $\hat{\boldsymbol{H}}^{(0)}$. The final result for the numerator in Eq. (6.7) evaluated at $x_s = 0$ can be written as

$$\partial\tilde{\sigma}/\partial x_s|_{x_s=0} = \{2 + n^{(1)}/n^{(0)}\}\lambda^{(0)} + \mu^{(0)} + (\hat{\boldsymbol{H}}^{(0)}|\{\hat{\boldsymbol{A}}^{(0)} + \hat{\boldsymbol{B}}^{(0)}\}), \tag{B.21}$$

$$\begin{aligned}
(\hat{\boldsymbol{A}}^{(0)})_k^{\alpha\beta} \;=\; & n^{(0)} \{(\boldsymbol{S}^{(0)})_k^{\alpha b} - (\boldsymbol{F}^{(0)})_k^{\alpha b}\} (\hat{\boldsymbol{\mathcal{F}}}^{(0)}[\boldsymbol{F}^{(0)}, \boldsymbol{F}^{(0)}])_k^{bb} (\boldsymbol{S}^{(1)})_k^{b\beta} \\
& + 2n^{(0)} \{(\boldsymbol{S}^{(0)})_k^{\alpha b} - (\boldsymbol{F}^{(0)})_k^{\alpha b}\} (\hat{\boldsymbol{\mathcal{F}}}^{(0)}[\boldsymbol{F}^{(0)}, \boldsymbol{F}^{(1)}])_k^{bs} (\boldsymbol{F}^{(1)})_k^{s\beta} \\
& - 2n^{(0)} \{(\boldsymbol{S}^{(1)})_k^{\alpha s} - (\boldsymbol{F}^{(1)})_k^{\alpha s}\} (\hat{\boldsymbol{\mathcal{F}}}^{(0)}[\boldsymbol{F}^{(0)}, \boldsymbol{F}^{(1)}])_k^{sb} \{(\boldsymbol{S}^{(0)})_k^{b\beta} - (\boldsymbol{F}^{(0)})_k^{b\beta}\} \\
& - 4n^{(0)} \{(\boldsymbol{S}^{(1)})_k^{\alpha s} - (\boldsymbol{F}^{(1)})_k^{\alpha s}\} (\hat{\boldsymbol{\mathcal{F}}}^{(0)}[\boldsymbol{F}^{(0)}, \boldsymbol{F}^{(1)}])_k^{ss} \{(\boldsymbol{S}^{(1)})_k^{s\beta} - (\boldsymbol{F}^{(1)})_k^{s\beta}\} \\
& + 2n^{(0)} \{(\boldsymbol{S}^{(1)})_k^{\alpha s} - (\boldsymbol{F}^{(1)})_k^{\alpha s}\} (\hat{\boldsymbol{\mathcal{F}}}^{(0)}[\boldsymbol{F}^{(0)}, \boldsymbol{F}^{(1)}])_k^{ss} (\boldsymbol{S}^{(1)})_k^{s\beta},
\end{aligned} \tag{B.22}$$

$$\hat{\boldsymbol{B}}^{(0)} = \hat{\boldsymbol{K}}^{(0)} \hat{\boldsymbol{L}}^{(0)}, \tag{B.23}$$

$$
\begin{aligned}
(\hat{\boldsymbol{K}}^{(0)})_k^{bb} &= 1-(\boldsymbol{F}^{(0)})_k^{bb}/(\boldsymbol{S}^{(0)})_k^{bb},\\
(\hat{\boldsymbol{K}}^{(0)})_k^{bs} &= (\boldsymbol{F}^{(0)})_k^{bb}(\boldsymbol{S}^{(1)})_k^{bs}/(\boldsymbol{S}^{(0)})_k^{bb}-(\boldsymbol{F}^{(1)})_k^{bs},\\
(\hat{\boldsymbol{K}}^{(0)})_k^{sb} &= 0,\\
(\hat{\boldsymbol{K}}^{(0)})_k^{ss} &= 1-(\boldsymbol{F}^{(1)})_k^{ss},
\end{aligned}
\tag{B.24}
$$

$$
\begin{aligned}
(\hat{\boldsymbol{L}}^{(0)})_k^{\alpha\beta} &= n^{(0)}(\boldsymbol{S}^{(1)})_k^{\alpha b}(\hat{\boldsymbol{\mathcal{F}}}^{(0)}[\boldsymbol{F}^{(0)},\boldsymbol{F}^{(0)}])_k^{bb}\{(\boldsymbol{S}^{(0)})_k^{b\beta}-(\boldsymbol{F}^{(0)})_k^{b\beta}\}\\
&\quad +2n^{(0)}(\boldsymbol{S}^{(1)})_k^{\alpha s}(\hat{\boldsymbol{\mathcal{F}}}^{(0)}[\boldsymbol{F}^{(0)},\boldsymbol{F}^{(1)}])_k^{sb}\{(\boldsymbol{S}^{(0)})_k^{b\beta}-(\boldsymbol{F}^{(0)})_k^{b\beta}\}\\
&\quad +2n^{(0)}(\boldsymbol{S}^{(1)})_k^{\alpha s}(\hat{\boldsymbol{\mathcal{F}}}^{(0)}[\boldsymbol{F}^{(0)},\boldsymbol{F}^{(1)}])_k^{ss}\{(\boldsymbol{S}^{(1)})_k^{s\beta}-(\boldsymbol{F}^{(1)})_k^{s\beta}\}.
\end{aligned}
\tag{B.25}
$$

Due to the statement below Eq. (B.18), the final result, Eq. (B.21), does not depend on $(\boldsymbol{F}^{(1)})_k^{bb}$. The term $2\lambda^{(0)}$ results from the bb-elements of the last two scalar products in Eq. (B.9). The matrix $\hat{\boldsymbol{B}}^{(0)}$ represents the contribution of the third term in Eq. (B.9) where $\hat{\boldsymbol{K}}^{(0)}$ is nothing but the $x_s \to 0$ limit of $\{\boldsymbol{S}-\boldsymbol{F}\}\boldsymbol{S}^{-1}$ while $\hat{\boldsymbol{L}}^{(0)}$ is the corresponding limit for the expression $\{\partial\boldsymbol{S}/\partial x_s\}n\boldsymbol{x}^{-1}\hat{\boldsymbol{\mathcal{F}}}[\boldsymbol{F},\boldsymbol{F}]\boldsymbol{x}^{-1}\{\boldsymbol{S}-\boldsymbol{F}\}$. All remaining quantities are summarized to the matrix $\hat{\boldsymbol{A}}^{(0)}$.

Let us now consider the denominator in Eq. (6.7) which follows from Eq. (B.9) by choosing $\xi_i = \xi$. Since Eqs. (B.10) and (B.11) remain valid if one replaces the corresponding quantities by their derivatives with respect to ξ and since $\partial\boldsymbol{x}^{-1}/\partial\xi = \boldsymbol{0}$, the final result depends only on the bb-matrix elements. Thus, the denominator in Eq. (6.7) taken at $x_s = 0$ follows directly from the separation parameter of the monodisperse system. It is a positive constant.

B.3 Slope of a critical line

The explicit results above allow us to define a procedure for the calculation of the slope of a glass transition line at $x_s = 0$. It consists of five steps.

B.3.1 Calculation of the critical point

The first step is the determination of the critical coupling parameter ξ_0^c and the corresponding NEPs $(\boldsymbol{F}^{c,(0)})_k^{bb}$ of the corresponding one-component model of big particles. In the following, all quantities have to be taken at $\xi = \xi_0^c$, the critical coupling parameter of the one-component system. We drop the superscript c for convenience. The denominator in Eq. (6.7) taken at $x_s = 0$ also follows directly from the separation parameter of the monodisperse system. It is a positive constant which we calculate by numerical differentiation, for simplicity.

B.3.2 Calculation of the static structure functions

$\boldsymbol{S}^{(0)}$ and $\boldsymbol{S}^{(1)}$ entering into $\partial\tilde{\sigma}/\partial x_s|_{x_s=0}$ trough Eqs. (B.19)-(B.25) can be easily determined from $\boldsymbol{c}^{(0)}$ and $\boldsymbol{c}^{(1)}$ by using Eq. (4.8). The result reads

$$\begin{aligned}(\boldsymbol{S}^{(0)})_k^{bb} &= 1/\{1-n^{(0)}(\boldsymbol{c}^{(0)})_k^{bb}\},\\ (\boldsymbol{S}^{(0)})_k^{bs} &= 0,\\ (\boldsymbol{S}^{(0)})_k^{ss} &= 0,\end{aligned} \tag{B.26}$$

$$\begin{aligned}(\boldsymbol{S}^{(1)})_k^{ss} &= 1,\\ (\boldsymbol{S}^{(1)})_k^{bs} &= n^{(0)}(\boldsymbol{S}^{(0)})_k^{bb}(\boldsymbol{c}^{(0)})_k^{bs},\\ (\boldsymbol{S}^{(1)})_k^{bb} &= \{(\boldsymbol{S}^{(0)})_k^{bb}\}^2\{n^{(0)}[(\boldsymbol{c}^{(1)})_k^{bb}+(\boldsymbol{c}^{(0)})_k^{ss}]-(n^{(0)}-n^{(1)})(\boldsymbol{c}^{(0)})_k^{bb}-(n^{(0)})^2\\ &\quad\times[(\boldsymbol{c}^{(0)})_k^{bb}(\boldsymbol{c}^{(0)})_k^{ss}-(\boldsymbol{c}^{(0)})_k^{bs}(\boldsymbol{c}^{(0)})_k^{sb}]\}-(\boldsymbol{S}^{(0)})_k^{bb}\{1+n^{(0)}(\boldsymbol{c}^{(0)})_k^{ss}\}.\end{aligned} \tag{B.27}$$

Hence, in the second step we have to determine $\boldsymbol{c}^{(0)}$ and $\boldsymbol{c}^{(1)}$. Substituting $n = n^{(0)} + x_s n^{(1)} + \ldots$, $\boldsymbol{c} = \boldsymbol{c}^{(0)} + x_s\boldsymbol{c}^{(1)} + \ldots$, $\boldsymbol{h}$ analogous, and $\boldsymbol{x} = \boldsymbol{x}^{(0)} + x_s\boldsymbol{x}^{(1)}$ into Eqs. (4.43) and (4.44) leads to equations for $\boldsymbol{c}^{(l)}$ and $\boldsymbol{h}^{(l)}$ which have to be solved recursively. For $l = 0$ and $l = 1$, they read

$$\boldsymbol{h}^{(0)} = \boldsymbol{c}^{(0)} + n^{(0)}\boldsymbol{c}^{(0)}\boldsymbol{x}^{(0)}\boldsymbol{h}^{(0)} \tag{B.28}$$

with the zeroth-order PY closure for the d-dimensional binary hard sphere model

$$\begin{aligned}(\boldsymbol{h}^{(0)})^{\alpha\beta}(r) &= -1, \quad r<(R_\alpha+R_\beta),\\ (\boldsymbol{c}^{(0)})^{\alpha\beta}(r) &= 0, \quad r>(R_\alpha+R_\beta),\end{aligned} \tag{B.29}$$

and the zeroth-order $T/2$-HNC closure for the binary point dipole model in 2D

$$\begin{aligned}\ln[(\boldsymbol{h}^{(0)})^{\alpha\beta}(r)+1] &= (\boldsymbol{h}^{(0)})^{\alpha\beta}(r)-(\boldsymbol{c}^{(0)})^{\alpha\beta}(r)-(\boldsymbol{u}_{eff}^{(0)})^{\alpha\beta}(r),\\ (\boldsymbol{u}_{eff}^{(0)})^{\alpha\beta}(r) &= \frac{2}{[\pi n^{(0)}]^{3/2}}\frac{\chi_\alpha\chi_\beta}{\chi_b^2}\frac{\Gamma}{r^3},\end{aligned} \tag{B.30}$$

and

$$\boldsymbol{h}^{(1)} = \boldsymbol{c}^{(1)} + n^{(1)}\boldsymbol{c}^{(0)}\boldsymbol{x}^{(0)}\boldsymbol{h}^{(0)} + n^{(0)}\{\boldsymbol{c}^{(1)}\boldsymbol{x}^{(0)}\boldsymbol{h}^{(0)} + \boldsymbol{c}^{(0)}\boldsymbol{x}^{(1)}\boldsymbol{h}^{(0)} + \boldsymbol{c}^{(0)}\boldsymbol{x}^{(0)}\boldsymbol{h}^{(1)}\} \tag{B.31}$$

with the first-order PY closure for the d-dimensional binary hard sphere model

$$\begin{aligned}(\boldsymbol{h}^{(1)})^{\alpha\beta}(r) &= 0, \quad r<(R_\alpha+R_\beta),\\ (\boldsymbol{c}^{(1)})^{\alpha\beta}(r) &= 0, \quad r>(R_\alpha+R_\beta),\end{aligned} \tag{B.32}$$

and the first-order $T/2$-HNC closure for the binary point dipole model in 2D

$$\begin{aligned}(\boldsymbol{h}^{(1)})^{\alpha\beta}(r) &= \{(\boldsymbol{h}^{(0)})^{\alpha\beta}(r)+1\}\{(\boldsymbol{h}^{(1)})^{\alpha\beta}(r)-(\boldsymbol{c}^{(1)})^{\alpha\beta}(r)-(\boldsymbol{u}_{eff}^{(1)})^{\alpha\beta}(r)\},\\ (\boldsymbol{u}_{eff}^{(1)})^{\alpha\beta}(r) &= 2\{1-\delta\}(\boldsymbol{u}_{eff}^{(0)})^{\alpha\beta}(r).\end{aligned} \tag{B.33}$$

Furthermore, we have $(\boldsymbol{x}^{(0)})_k^{bb}=1$, $(\boldsymbol{x}^{(1)})_k^{bb}=-1$, $(\boldsymbol{x}^{(1)})_k^{ss}=1$, and all other components are zero, and for the d-dimensional binary hard sphere model $n^{(0)}$ and $n^{(1)}$ are given by

$$\begin{aligned}n^{(0)} &= (\varphi d)/(\Omega_d R_b^d),\\ n^{(1)} &= n^{(0)}(1-(R_s/R_b)^d),\end{aligned} \tag{B.34}$$

while for the binary point dipole model in 2D its is

$$\begin{aligned}n^{(0)} &= n,\\ n^{(1)} &= 0,\end{aligned} \tag{B.35}$$

since for this model it is convenient to keep n fixed for all Γ, x_s, δ_χ. Note that Eqs. (B.29), (B.30), (B.32), (B.33), (B.34), and (B.35) are the only explicitly model-dependent equations. Hence, the procedure can be easily extended for both to arbitrary binary mixtures and to closure relations different from PY or $T/2$-HNC. Let us further remark that $(\boldsymbol{c}^{(0)})_k^{bb}$ and $(\boldsymbol{h}^{(0)})_k^{bb}$ are nothing but the direct and total correlations functions for the one-component system of big particles.

B.3.3 Calculation of the critical nonergodicity parameters

Beside $(\boldsymbol{F}^{(0)})_k^{bb}$, the evaluation of Eqs. (B.19)-(B.25) requires also $(\boldsymbol{F}^{(1)})_k^{bs}$ and $(\boldsymbol{F}^{(1)})_k^{ss}$ as input. It is straightforward to derive the equations for these quantities from the fixed-point equation $\boldsymbol{F}=\boldsymbol{\mathcal{I}}[\boldsymbol{F}]$ following from Eq. (4.18) by considering the limit $x_s\to 0$. We obtain

$$(\boldsymbol{F}^{(1)})_k^{ss} = 1-\{1+2n^{(0)}(\hat{\boldsymbol{\mathcal{F}}}^{(0)}[\boldsymbol{F}^{(0)},\boldsymbol{F}^{(1)}])_k^{ss}\}^{-1}, \tag{B.36}$$

$$\begin{aligned}(\boldsymbol{F}^{(1)})_k^{bs} &= 2n^{(0)}(\boldsymbol{S}^{(1)})_k^{bs}(\hat{\boldsymbol{\mathcal{F}}}^{(0)}[\boldsymbol{F}^{(0)},\boldsymbol{F}^{(1)}])_k^{ss}\{1-(\boldsymbol{F}^{(1)})_k^{ss}\}\\ &\quad +2n^{(0)}(\boldsymbol{S}^{(0)})_k^{bb}(\hat{\boldsymbol{\mathcal{F}}}^{(0)}[\boldsymbol{F}^{(0)},\boldsymbol{F}^{(1)}])_k^{bs}\{1-(\boldsymbol{F}^{(1)})_k^{ss}\}\\ &\quad +n^{(0)}(\boldsymbol{S}^{(0)})_k^{bb}(\hat{\boldsymbol{\mathcal{F}}}^{(0)}[\boldsymbol{F}^{(0)},\boldsymbol{F}^{(0)}])_k^{bb}\{(\boldsymbol{S}^{(1)})_k^{bs}-(\boldsymbol{F}^{(1)})_k^{bs}\}.\end{aligned} \tag{B.37}$$

Since $(\boldsymbol{F}^{(0)})_k^{bb}$ have already been determined in the first step, Eq. (B.36) allows to calculate $(\boldsymbol{F}^{(1)})_k^{ss}$. The r.h.s. of Eq. (B.36) does neither depend on $(\boldsymbol{F}^{(1)})_k^{bs}$ nor on $(\boldsymbol{F}^{(1)})_k^{bb}$. The $(\boldsymbol{F}^{(1)})_k^{ss}$ are nothing but the tagged-particle NEPs for a single small particle in the

fluid of the big particles. Finally, Eq. (B.37) allows us to calculate $(\boldsymbol{F}^{(1)})_k^{bs}$, since it is not dependent on $(\boldsymbol{F}^{(1)})_k^{bb}$ due to the statement below Eq. (B.18).

B.3.4 Calculation of the critical eigenvectors

The evaluation of Eqs. (B.19)-(B.25) requires the zeroth-order left-eigenvector $\hat{\boldsymbol{H}}^{(0)}$ as last input. For its unique determination, also the zeroth-order right-eigenvector $\boldsymbol{H}^{(0)}$ is needed. For $x_s \to 0$, Eq. (4.19) reduces to

$$\boldsymbol{\mathcal{C}}^{(0)}[\boldsymbol{Y}] = 2n^{(0)}\hat{\boldsymbol{M}}^{(0)}\hat{\boldsymbol{\mathcal{F}}}^{(0)}[\boldsymbol{F}^{(0)}, \boldsymbol{Y}]\hat{\boldsymbol{N}}^{(0)}, \tag{B.38}$$

$$\begin{aligned}
(\hat{\boldsymbol{M}}^{(0)})_k^{bb} &= (\boldsymbol{S}^{(0)})_k^{bb} - (\boldsymbol{F}^{(0)})_k^{bb}, \\
(\hat{\boldsymbol{M}}^{(0)})_k^{bs} &= (\boldsymbol{S}^{(1)})_k^{bs} - (\boldsymbol{F}^{(1)})_k^{bs}, \\
(\hat{\boldsymbol{M}}^{(0)})_k^{sb} &= 0, \\
(\hat{\boldsymbol{M}}^{(0)})_k^{ss} &= 1 - (\boldsymbol{F}^{(1)})_k^{ss},
\end{aligned} \tag{B.39}$$

$$\begin{aligned}
(\hat{\boldsymbol{N}}^{(0)})_k^{bb} &= (\boldsymbol{S}^{(0)})_k^{bb} - (\boldsymbol{F}^{(0)})_k^{bb}, \\
(\hat{\boldsymbol{N}}^{(0)})_k^{bs} &= 0, \\
(\hat{\boldsymbol{N}}^{(0)})_k^{sb} &= (\boldsymbol{S}^{(1)})_k^{sb} - (\boldsymbol{F}^{(1)})_k^{sb}, \\
(\hat{\boldsymbol{N}}^{(0)})_k^{ss} &= 1 - (\boldsymbol{F}^{(1)})_k^{ss}.
\end{aligned} \tag{B.40}$$

Now, $\boldsymbol{\mathcal{C}}^{(0)}$ and the corresponding adjoint map $\boldsymbol{\mathcal{C}}^{\dagger(0)}$ allow us to calculate the eigenvectors $\boldsymbol{H}^{(0)}$ and $\hat{\boldsymbol{H}}^{(0)}$ obeying the normalization

$$\sum_k (\hat{\boldsymbol{H}}^{(0)})_k^{bb} (\boldsymbol{H}^{(0)})_k^{bb} = 1, \tag{B.41}$$

$$\sum_k (\hat{\boldsymbol{H}}^{(0)})_k^{bb} \{(\boldsymbol{H}^{(0)})_k^{bb}\}^2 / \{(\boldsymbol{S}^{(0)})_k^{bb} - (\boldsymbol{F}^{(0)})_k^{bb}\} = 1. \tag{B.42}$$

While for $\boldsymbol{H}^{(0)}$ only the *bb*-elements are nonvanishing, $\hat{\boldsymbol{H}}^{(0)}$ has nontrivial contributions for all particle indices. $(\boldsymbol{H}^{(0)})_k^{bb}$ and $(\hat{\boldsymbol{H}}^{(0)})_k^{bb}$ are the eigenvectors for the one-component model of big particles.

B.3.5 Calculation of the slope

Now, we have determined all quantities for the evaluation of Eqs. (B.19)-(B.25) and are able to calculate the slope of the glass transition line by using Eqs. (6.7) and (B.8).

Bibliography

[1] U. Bengtzelius, W. Götze, and A. Sjölander, J. Phys. C **17**, 5915 (1984).

[2] W. Götze, *Complex Dynamics of Glass-Forming Liquids, A Mode-Coupling Theory* (Oxford University Press, Oxford, 2009).

[3] R. Schilling and T. Scheidsteger, Phys. Rev. E **56**, 2932 (1997).

[4] J.-L. Barrat and A. Latz, J. Phys.: Condens. Matter **2**, 4289 (1990).

[5] M. Fuchs and M. E. Cates, Phys. Rev. Lett. **89**, 248304 (2002).

[6] M. Fuchs and M. E. Cates, J. Phys.: Condens. Matter **17**, S1681 (2005).

[7] M. Fuchs and M. E. Cates, Faraday Discuss. **123**, 267 (2003).

[8] D. Hajnal and M. Fuchs, Eur. Phys. J. E **28**, 125 (2009).

[9] J. J. Crassous, M. Siebenbürger, M. Ballauff, M. Drechsler, D. Hajnal, O. Henrich, and M. Fuchs, J. Chem. Phys. **128**, 204902 (2008).

[10] M. Siebenbürger, M. Fuchs, H. Winter, and M. Ballauff, J. Rheol. **53**, 707 (2009).

[11] J. M. Brader, Th. Voigtmann, M. E. Cates, and M. Fuchs, Phys. Rev. Lett. **98**, 058301 (2007).

[12] J. M. Brader, M. E. Cates, and M. Fuchs, Phys. Rev. Lett. **101**, 138301 (2008).

[13] J. Zausch, J. Horbach, M. Laurati, S. U. Egelhaaf, J. M. Brader, Th. Voigtmann, and M. Fuchs, J. Phys.: Condens. Matter **20**, 404210 (2008).

[14] V. Krakoviack, Phys. Rev. Lett. **94**, 065703 (2005).

[15] V. Krakoviack, Phys. Rev. E **75**, 031503 (2007).

[16] V. Krakoviack, Phys. Rev. E **79**, 061501 (2009).

[17] J. Kurzidim, D. Coslovich, and G. Kahl, Phys. Rev. Lett. **103**, 138303 (2009).

[18] M. Bayer, J. M. Brader, F. Ebert, M. Fuchs, E. Lange, G. Maret, R. Schilling, M. Sperl, and J. P. Wittmer, Phys. Rev. E **76**, 011508 (2007).

[19] W. T. Kranz, M. Sperl, and A. Zippelius, Phys. Rev. Lett. **104**, 225701 (2010).

[20] S. Lang, V. Boţan, M. Oettel, D. Hajnal, T. Franosch, and R. Schilling, Phys. Rev. Lett. **105**, 125701 (2010).

[21] J. Mittal, T. M. Truskett, J. R. Errington, and G. Hummer, Phys. Rev. Lett. **100**, 145901 (2008).

[22] B. Schmid and R. Schilling, Phys. Rev. E **81**, 041502 (2010).

[23] L. Santen and W. Krauth, Nature (London) **405**, 550 (2000).

[24] T. Franosch, M. Fuchs, W. Götze, M. R. Mayr, and A. P. Singh, Phys. Rev. E **55**, 7153 (1997).

[25] W. Götze and Th. Voigtmann, Phys. Rev. E **67**, 021502 (2003).

[26] H. König, R. Hund, K. Zahn, and G. Maret, Eur. Phys. J. E **18**, 287 (2005).

[27] V. I. Arnol'd, *Catastrophe Theory, 3rd ed.* (Springer, Berlin, 1992).

[28] T. Franosch and Th. Voigtmann, J. Stat. Phys. **109**, 237 (2002).

[29] Th. Voigtmann, doctoral thesis, TU München, 2002.

[30] J. Bosse and J. S. Thakur, Phys. Rev. Lett. **59**, 998 (1987).

[31] J. S. Thakur and J. Bosse, Phys. Rev. A **43**, 4388 (1991).

[32] J. Bosse and Y. Kaneko, Phys. Rev. Lett. **74**, 4023 (1995).

[33] F. Höfling, E. Frey, and T. Franosch, (unpublished).

[34] E. Leutheusser, Phys. Rev. A **28**, 1762 (1983).

[35] F. Höfling and T. Franosch, Phys. Rev. Lett. **98**, 140601 (2007).

[36] J. P. Hansen and I. R. McDonald, *Theory of Simple Liquids, 3rd ed.* (Academic Press, London, 2006).

[37] K. Binder and D. W. Heermann, *Monte Carlo Simulation in Statistical Physics*, 4th ed. (Springer, Berlin, Heidelberg, 2010).

[38] F. Ebert, P. Dillmann, G. Maret, and P. Keim, Rev. Sci. Instrum. **80**, 083902 (2009).

[39] E. Noruzifar and M. Oettel, Phys. Rev. E **79**, 051401 (2009).

[40] J. D. Jackson, *Classical Electrodynamics, 3rd ed.* (Wiley, New York, 1999).

[41] F. Ebert, doctoral thesis, Universität Konstanz, 2008.

[42] S. I. Henderson, T. C. Mortensen, S. M. Underwood, and W. van Megen, Physica A **233**, 102 (1996).

[43] A. Ikeda and K. Miyazaki, Phys. Rev. Lett. **104**, 255704 (2010).

[44] S. R. Williams and W. van Megen, Phys. Rev. E **64**, 041502 (2001).

[45] G. Foffi, W. Götze, F. Sciortino, P. Tartaglia, and Th. Voigtmann, Phys. Rev. Lett. 91, 085701 (2003).

[46] G. Foffi, W. Götze, F. Sciortino, P. Tartaglia, and Th. Voigtmann, Phys. Rev. E **69**, 011505 (2004).

[47] R. Juárez-Maldonado and M. Medina-Noyola, Phys. Rev. E **77**, 051503 (2008).

[48] S. Asakura and F. Osawa, J. Chem. Phys. **22**, 1255 (1954).

[49] T. Okubo and T. Odagaki, J. Phys.: Condens. Matter **16**, 6651 (2004).

[50] Th. Voigtmann, unpublished.

[51] F. Weysser, unpublished.

[52] F. Weysser and D. Hajnal, in preparation.

[53] F. Weysser, diploma thesis, Universität Konstanz (2007).

[54] L. Assoud, R. Messina, and H. Löwen, Europhys. Lett. **80**, 48001 (2007).

[55] N. Hoffmann, F. Ebert, C. N. Likos, H. Löwen, and G. Maret, Phys. Rev. Lett. **97**, 078301 (2006).

[56] K. Zahn, doctoral thesis, Université Louis Pasteur Strasbourg, 1997.

[57] N. Hoffmann, doctoral thesis, Heinrich-Heine-Universität Düsseldorf, 2006.

[58] S. H. L. Klapp, unpublished.

[59] K. Dawson, G. Foffi, M. Fuchs, W. Götze, F. Sciortino, M. Sperl, P. Tartaglia, Th. Voigtmann, and E. Zaccarelli, Phys. Rev. E **63**, 011401 (2000).

[60] L. Fabbian, W. Götze, F. Sciortino, P. Tartaglia, and F. Thiery, Phys. Rev. E **59**, R1347 (1999).

[61] J. Bergenholtz and M. Fuchs, Phys. Rev. E **59**, 5706 (1999).

[62] F. Lado, J. Chem. Phys. **49**, 3092 (1968).

[63] J. L. Lebowitz and J. S. Rowlinson, J. Chem. Phys. **41**, 133 (1964).

[64] M. Fuchs, W. Götze, I. Hofacker, and A. Latz, J. Phys.: Condens. Matter **3**, 5047 (1991).

[65] D. Hajnal, diploma thesis, Universität Konstanz (2007).
http://nbn-resolving.de/urn:nbn:de:bsz:352-opus-38002
www.ub.uni-konstanz.de/kops/volltexte/2007/3800/